

MODELLING OF ALKALI-AGGREGATE REACTION EFFECTS IN REINFORCED CONCRETE STRUCTURES

by

Anca-Cristina Jurcut

A thesis submitted in conformity with the requirements
for the degree of Master of Applied Science

Civil Engineering
University of Toronto

© Copyright by Anca-Cristina Jurcut (2015)

Modelling of Alkali-Aggregate Reaction Effects in Reinforced Concrete Structures

Anca-Cristina Jurcut

Master of Applied Sciences

Graduate Department of Civil Engineering
University of Toronto

2015

Abstract

Significant research has been performed worldwide on alkali-aggregate reaction (AAR) since its first deleterious effects on concrete structures were identified 75 years ago. According to the CSA A864-00, conventional methods become invalid for the structural assessment of AAR-affected members due to the induced anisotropy with regards to the mechanical properties of concrete. As such, there is a need for proper analysis tools to investigate the behaviour of an AAR-affected structure, and assist in identifying possible rehabilitation actions.

The VecTor suite of nonlinear finite element programs, developed at the University of Toronto for the analysis of reinforced concrete structures, can be developed into such a tool. The work performed in this thesis is directed towards modifying the algorithms of VecTor2 and VecTor3 for the analysis of AAR-affected structures, as part of a comprehensive study initiated and funded by the Canadian Nuclear Safety Commission.

Acknowledgments

First, I would like to thank my supervisor, Professor Frank J. Vecchio, for all the support and guidance he has provided throughout the duration of my studies. I left the meetings with him inspired by his erudition, boundless patience and thoughtful questions, and motivated to reach his expectations. I cannot picture a better place for my graduate studies, and I am grateful that he provided me with the opportunity to work under his supervision.

I would also like to thank Professor Shamim Sheikh for reviewing this thesis and to Professor Daman Panesar for the valuable advice towards my work.

I am grateful for the financial support provided by the Canadian Nuclear Safety Commission, from Professor F. J. Vecchio, and from the Department of Civil Engineering of the University of Toronto.

I would like to express my deepest appreciation to my friends and colleagues, for their support and friendship throughout the course of my graduate studies, making it an engaging experience: Vahid Sadeghian, Andac Lulec, Dr. Fady ElMohandes, Mark Hunter, Jun Wei Luo, Benard Isojeh, Stamatina Chasiotti, Farhad Habibi, and Bishnu Gautam.

Finally, I would like to thank my fiancé Sebastian, and my family for their unconditional love, encouragement, and endless patience.

Table of Contents

Acknowledgments.....	iii
Table of Contents.....	iv
List of Tables.....	vii
List of Figures.....	ix
Chapter 1 Introduction.....	1
1.1 Overview.....	1
1.2 Research Objectives.....	2
1.3 Thesis Content.....	3
Chapter 2 Literature Review.....	5
2 Literature Review.....	5
2.1 The Chemical Mechanism of Alkali-Aggregate Reactions.....	5
2.1.1 Alkali-Silica Reaction.....	5
2.1.2 Alkali-Carbonate Reaction.....	7
2.2 Delayed Ettringite Formation.....	7
2.3 Factors Influencing ASR.....	8
2.3.1 Temperature.....	8
2.3.2 Water.....	9
2.3.3 Alkali Content.....	10
2.3.4 Type of Reactive Aggregate.....	11
2.3.5 Aggregate Size.....	12
2.3.6 Air Entrainment and Porosity.....	13
2.3.7 Stresses.....	13
2.4 Changes in Mechanical Properties.....	15

2.4.1	Effect on Compressive Strength	15
2.4.2	Effect on Tensile Strength	16
2.4.3	Effect on Modulus of Elasticity	17
2.5	Constitutive Models for ASR	18
2.5.1	Micro-Models	18
2.5.2	Meso-Models	26
2.5.3	Macro-Models.....	29
Chapter 3	VecTor Methodology	49
3	VecTor Methodology	49
3.1	Introduction.....	49
3.2	Stiffness Formulation.....	50
3.3	Modelling the Effects of ASR in VecTor2 and VecTor3	54
3.3.1	Implemented Models for ASR-Induced Expansion.....	54
3.3.2	Implemented Models for Mechanical Properties.....	56
3.4	Sample Calculation	58
Chapter 4	Verification Studies.....	60
4	Verification Studies.....	60
4.1	Behavioural Models and Analysis Parameters	60
4.2	Material-Level Investigation.....	62
4.3	Structural-Level Investigations.....	67
4.3.1	Kobayashi et al., 1988.....	68
4.3.2	Fan and Hanson, 1998.....	74
4.3.3	Deschenes et al., 2009.....	79
4.3.4	Monette, 1997	83
Chapter 5	University of Toronto Specimens	88
5	University of Toronto Specimens	88

5.1 Experimental Program	88
5.2 Two-Dimensional Analysis	92
5.3 Three-Dimensional Analysis	99
Chapter 6 Assessment Recommendations	102
6 Assessment Recommendations	102
6.1 Review of Guidelines on ASR-Affected Structures	102
6.1.1 ISE, 1992.....	103
6.1.2 CUR – Recommendation 102, 2008	108
6.1.3 CSA Special Publication A864-00, 2000.....	112
6.2 Modelling Recommendations	114
Chapter 7 Conclusions	116
7 Conclusions	116
7.1 Summary	116
7.2 Conclusions.....	116
7.3 Recommendations.....	118
References.....	119

List of Tables

Table 2.1 – Deleteriously Reactive Rocks, Minerals and Synthetic Substances (adapted from ACI Committee 201, 1992)	12
Table 2.2 – Comparison of deformations of free expansion specimens versus uniaxially loaded specimens (adapted from Larive, 1997).....	14
Table 2.3 – Percentage loss in compressive strength of ASR-affected concrete (adapted from Swamy and Al-Asali, 1988).....	16
Table 2.4 – Percentage loss in tensile strength of ASR-affected concrete (adapted from Swamy and Al-Asali, 1988).....	17
Table 2.5 – Percentage loss in elastic modulus of ASR-affected concrete (adapted from Swamy and Al-Asali, 1988).....	18
Table 2.6 – Strength and stiffness of components used in lattice simulation (Çopuroğlu and Schlangen, 2007).....	26
Table 3.1 – Lower bound residual mechanical properties as percentage of value for unaffected concrete at 28 days (adapted from ISE, 1992).....	57
Table 4.1 – Constitutive models used for the validation studies	61
Table 4.2 – Material properties.....	61
Table 4.3 – Mixture proportions (kg/m ³).....	62
Table 4.4 – Concrete properties: 150 mm x 300 mm cylinders.....	62
Table 4.5 – Concrete properties: 100 mm x 200 mm cylinders.....	65
Table 4.6 – Actual vs. ISE estimated concrete mechanical properties	67
Table 4.7 – Details of test specimens.....	70
Table 4.8 – Experimental versus theoretical maximum ultimate loads	73
Table 4.9 – Experimental versus theoretical strains	73
Table 4.10 – Reinforcement properties.....	76
Table 4.11 – Experimental versus theoretical maximum ultimate loads	77
Table 4.12 – Concrete strength and specimens' age at testing	79

Table 4.13 – ASR/DEF expansion: experimental vs. calculated strains.....	82
Table 4.14 – Shear strength of the deep beam shear spans.....	82
Table 4.15 – Shear strength of the sectional shear spans.....	82
Table 4.16 – Concrete properties	84
Table 5.1 – Concrete properties (Habibi et al., 2015).....	91
Table 5.2 – Reinforcement properties (Habibi et al., 2015)	91
Table 5.3 – Reinforcement ratios.....	93
Table 6.1 – ISE prediction vs. Experimental Results	103
Table 6.2 – Structural risk (CUR – Recommendation 102, 2008).....	111

List of Figures

Figure 2.1 – Mechanism of dissolution of silica by hydroxyl attack. The dotted line represents the interface between silica and water (adapted from Iler 1976 and Urhan 1987a)	6
Figure 2.2 – ASR development.....	6
Figure 2.3 – Idealized repetitive cubical cell with one reactive particle of original diameter D (the remaining unreacted particle of radius z is marked gray, δ_c =thickness of layer with capillary pores and cracks into which pressurized ASR gel formed intrudes by diffusion) (adapted from Bažant and Steffens, 2000)	20
Figure 2.4 – Idealized cubic array of expanding spherical glass particles surrounded by flaws and dominant growing cracks filled by ASR gel (left); Cell with glass particle and crack (right top); Layer of reacted glass and layer of ASR gel forced into capillary pores of concrete (right bottom) (adapted from Bazant et al., 2000).....	21
Figure 2.5 – (a) Idealized evolution of crack front from initial stage of shallow cracks to terminal stage of small circular uncracked ligaments. (b) Superposition revealing equivalence of crack pressurization and stress externally applied on one cell (adapted from Bazant et al., 2000)	22
Figure 2.6 – Ion diffusion into aggregate (adapted from Puatatsananon and Saouma, 2013).....	24
Figure 2.7 – Gel diffusion into cement paste (adapted from Puatatsananon and Saouma, 2013)	25
Figure 2.8 – ASR damage sequence according to Delft Lattice Model (adapted from Çopuroğlu and Schlangen, 2007).....	26
Figure 2.9 – Factors influencing ASR concrete expansion (adapted from Leger et al., 1996).....	30
Figure 2.10 – CTMR-ASR simulation model (adapted from Leger et al., 1996).....	32
Figure 2.11 – Mesoscopic mechanism of ASR swelling (adapted from Ulm et al., 2000).....	37
Figure 2.12 – Chemoelastic pressure-spring device for ASR swelling (adapted from Ulm et al., 2000)	38
Figure 2.13 – One-dimensional model of expansive concrete behavior (adapted from Farage et al., 2004)	42
Figure 2.14 – One-dimensional stress-strain relation (adapted from Farage et al., 2004).....	43
Figure 2.15 – One-dimensional idealized concrete expansion model: P_g is the gel pressure and VEPD is the visco-elasto-plastic and damaged concrete behaviour law symbol (adapted from Grimal et al., 2008)	48

Figure 3.1 – VecTor2 coordinate reference systems (adapted from Vecchio, 1990)	53
Figure 3.2 – ASR strains in terms of the compressive stress for Charlwood et al., (1992) model	55
Figure 3.3 – ASR strains in terms of the stress level for Curtis model.....	55
Figure 3.4 – Change in mechanical properties (adapted from ISE, 1992).....	57
Figure 4.1 – VecTor2 material-level model for a quarter of a cylinder.....	63
Figure 4.2 – Stress-strain behaviour in compression	64
Figure 4.3 – VecTor2 model for middle-notched prism.....	65
Figure 4.4 – Load-deflection behaviour for Giaccio prisms specimens	66
Figure 4.5 – Specimen reinforcement and cross section (adapted from Kobayashi et al., 1988).	68
Figure 4.6 – Finite element model for beam specimen I-1	70
Figure 4.7 – Predicted and experimental crack patterns for beam II-2.....	71
Figure 4.8 – Load-deflection relationships: analytical versus experimental results	72
Figure 4.9 – Specimen reinforcement – cross section (adapted from Fan and Hanson, 1998) ...	74
Figure 4.10 – Length expansion of beams #3N and #3R (adapted from Fan and Hanson, 1998)	75
Figure 4.11 – Finite element model for the Fan and Hanson beam specimens	76
Figure 4.12 – Deflected shape and cracking pattern for #3R beam at 70% of the ultimate capacity	77
Figure 4.13 – Results of the flexural loading tests for Fan and Hanson specimens	78
Figure 4.14 – Specimen reinforcement - cross section (adapted from Deschenes et al., 2009) ...	80
Figure 4.15 – Finite element model for sectional shear test	81
Figure 4.16 – Finite element representation of beam RB-2.....	84
Figure 4.17 – Stress-strain curves for 28 days and 161 days non-reactive concrete	85
Figure 4.18 – Stress-strain curves for 28 days and 147 days reactive concrete.....	86
Figure 4.19 – Load-deflection relationships for non-reactive beams NB-2 and NB-1,7.....	87

Figure 4.20 – Load-deflection relationships for reactive beams RB-1,6 and RB-2,5	87
Figure 5.1 – Geometric details and reinforcement layout of shear wall specimens	89
Figure 5.2 – Test set-up (Habibi et al., 2015)	90
Figure 5.3 – Reversed cyclic loading history.....	90
Figure 5.4 – Load-deflection relationship for the control wall specimen Regular A (Habibi et al., 2015)	91
Figure 5.5 – Load-deflection relationship for the ASR-affected wall specimen ASR A1 (Habibi et al., 2015)	92
Figure 5.6 – FE model of the shear wall specimens	93
Figure 5.7 – Calculated crack pattern and deflected shape (20x) of Regular A shear wall at ultimate load.....	95
Figure 5.8 – Calculated crack pattern and deflected shape (20x) of ASR A1 shear wall at ultimate load.....	95
Figure 5.9 – Regular A shear wall at failure (Habibi et al., 2015).....	96
Figure 5.10 – ASR A1 shear wall at failure (Habibi et al., 2015)	96
Figure 5.11 – Monotonic vs. cyclic analytical behaviour of Regular A specimen.....	97
Figure 5.12 – Monotonic vs. cyclic analytical behaviour of ASR A1 specimen (Charlwood model for ASR expansion).....	97
Figure 5.13 – Comparison of experimental and analytical results for lateral load versus displacement relationship of Regular A shear wall specimen	98
Figure 5.14 – Comparison of experimental and analytical results for lateral load versus displacement relationship of ASR A1 shear wall specimen	99
Figure 5.15 – Three-dimensional finite element model.....	100
Figure 5.16 – VecTor2 versus VecTor3 responses for Regular A wall.....	101
Figure 5.17 – VecTor2 versus VecTor3 responses for ASR A1 wall.....	101
Figure 6.1 – Restrained expansion (ISE, 1992)	104
Figure 6.2 – Concrete compressive stress (ISE, 1992)	104

Figure 6.3 – Effect of compressive stress on expansion (ISE, 1992)	105
Figure 6.4 – Appraisal leading to diagnosis and action following ASR (ISE, 1992).....	107
Figure 6.5 – Internal ASR cracking in a vertical section of the bridge deck (Bakker, 2008).....	108
Figure 6.6 – Flow chart for inspection and studies (adapted from CUR – Recommendation 102, 2008)	110
Figure 6.7 – Principle of measuring the relative cumulative crack width (CUR – Recommendation 102, 2008)	111
Figure 6.8 – Procedure for the diagnosis of AAR in structures (adapted from CSA A864-00, 2000)	113

Chapter 1

Introduction

1.1 Overview

Through time concrete has proven to be a durable material, yet it is vulnerable to a number of factors that cause physical, chemical, electro-chemical, and biological deterioration. Chemical deterioration in the form of alkali-aggregate reaction (AAR) is a slow-evolving but progressive process leading to expansion and cracking of concrete, and to costly maintenance interventions. AAR is a chemical reaction between alkali hydroxides (sodium and potassium) from Portland cement or from an external source and certain reactive aggregates. Two main types of AAR are currently recognized based on the type of reactive minerals involved in the reaction: the alkali-silica reaction (ASR) and the alkali-carbonate reaction (ACR).

The alkali-silica reaction is a chemical reaction between the alkali present in the cement paste and certain siliceous rocks and minerals such as opaline chert, strained quartz and acidic volcanic glass, present in some aggregates. The product of this reaction is the alkali-silica gel, which under certain circumstances expands and leads to cracking of the affected concrete. Problems due to ASR were first identified in the State of California in the 1920s and 1930s when several structures, including school buildings, bridges, road pavements and a sea wall, developed cracks a few years after their construction although proper standards had been applied during their construction. The studies conducted by Stanton (1940, 1942) showed that the expansion of concrete was caused by the chemical reaction between alkali from cement and siliceous aggregates. It also identified the role of alkali content in the reaction, and the capacity of pozzolanic material to prevent the expansion.

Reported for the first time in Ontario in the 1950s (Swenson, 1957), the alkali-carbonate reaction is a chemical reaction between the alkali from the cement paste and certain carbonate rocks, particularly calcitic dolomite and dolimitic limestones, present in some aggregates. The reaction is usually accompanied by dedolomitization and expansion of the affected aggregate particles, leading to abnormal expansion and cracking of concrete in service.

In 1982 another mechanism of chemical deterioration of concrete was reported: delayed ettringite formation (DEF), a form of sulfate attack common in concrete exposed to high temperatures during the curing process. The presence of products of both ASR and DEF has been identified during

structure diagnosis. As such, several experimental studies have been carried out to investigate the interaction of the two reactions (Shayan and Ivanusec, 1996, Bouzabata et al., 2012). The conclusion of these studies was that even though the chemical mechanisms of AAR and DEF differ, both reactions have similar deleterious effects on concrete.

The alkali-silica reaction is far more widespread and is the main focus of this work. More recently, ASR has been identified as a concrete degradation mechanism in nuclear power plants in Canada (Popovic et al., 2002, Tchnerer and Aziz, 2009, Tchnerer et al., 2009). The ring beam of the Gentility-1 CANDU Nuclear Power Plant had to undergo several repair sessions due to extensive deterioration to which ASR was identified as a contributing factor. A series of challenges arise when evaluating the behaviour of nuclear structures affected by ASR, as follows:

1. The effect of restraint on the structural effects of ASR caused by the biaxially prestressing of the containment structures is not yet fully understood.
2. As a result of the complex stress state which nuclear structures exhibit, the anisotropy of the mechanical properties of concrete caused by the anisotropic ASR expansion is expected to be increased, compared to other types of structures.
3. The in-situ material properties are difficult to obtain; destructive testing may not be an option, and non-destructive testing methods face challenges due to high steel congestion, accessibility, presence of liners, and high thickness of the sections.

1.2 Research Objectives

A significant amount of research is dedicated around the world to understanding the ASR mechanism. One such experimental program, initiated and funded by the Canadian Nuclear Safety Commission (CNSC), has been undertaken at the University of Toronto with the aim of correlating ASR damage and the mechanical and structural consequences. The study incorporates three main parts: material testing (Gautam et al., 2015), structural testing (Habibi et al., 2015), and structural analysis and modelling; the latter is the primary focus of this work.

Structures identified as suffering from ASR require, in most cases, structural assessment. According to the CSA A864-00 (2000), the conventional analytical methods for structural assessment are invalid in the case of ASR-affected structures due to the anisotropic changes in material properties induced. Thus, there is a need for improved analysis tools and ASR numerical

models to capture the observed behaviour, predict long-term effects, analyze failure mechanisms, and facilitate rehabilitation works. The VecTor suite of programs is a good candidate for such a software tool.

The VecTor programs, developed at the University of Toronto over the last 25 years, are nonlinear finite element programs dedicated to the analysis of reinforced concrete structures. The programs have analysis capabilities for beam sections (VecTor1), two-dimensional membrane structures (VecTor2), three-dimensional solid structures (VecTor3), plates and shells (VecTor4), plane frames (VecTor5), and axisymmetric solids (VecTor6). The VecTor programs can be combined to model mixed-type structures with the use of the master program Cyrus. They have been shown to be particularly capable of accurately modelling the response of shear-critical structures. The research program presented in this thesis serves to implement ASR constitutive models within the algorithms of VecTor2 and VecTor3, to verify the programs' capabilities with respect to modelling the effects of ASR on reinforced concrete structures, to identify deficiencies pertaining to the existing formulations, and to develop recommendations on the modelling techniques to be employed for ASR-affected structures.

As this study is focused particularly on nuclear structures, both reinforced concrete and prestressed concrete specimens were analyzed. The experimental data on ASR-affected structures considered in this study for verification purposes included various degrees of ASR-induced damage, reinforcement configurations, and long-term loading conditions. The ASR constitutive model developed as part of the material-level investigation (Gautam et al., 2015) was implemented in VecTor2 and VecTor3, and validated against the structural testing program (Habibi et al., 2015), in concurrent parts of this study.

1.3 Thesis Content

This thesis presents the analytical work undertaken to modify and verify the algorithms of VecTor2 and VecTor3 to accommodate the ASR effects. The overview for ASR and the research objectives were presented in Chapter 1.

Chapter 2 consists of a summary of the available research on ASR. The presented background information pertaining to the topic of this thesis encompasses the chemical mechanisms, the factors

influencing the reaction, the changes in mechanical properties, and the constitutive models developed for ASR.

Chapter 3 provides details on the formulation employed to model ASR effects in VecTor2 and VecTor3. Information on the VecTor methodology is presented, with emphasis on the calculation of ASR strains, and the deterioration in mechanical properties.

Chapter 4 presents the verification studies performed by modelling ASR-affected specimens reported in the literature. Analyses were performed at both the material and structural levels, comparing numerical behaviours with the experimentally observed ones.

Chapter 5 briefly describes the experimental program on the structural effects of ASR on the overall behaviour of squat shear walls, currently underway at the University of Toronto (Habibi et al., 2015). The modelling techniques used to estimate the response of the specimens using VecTor2 and VecTor3 are discussed in detail.

Chapter 6 summarises brief guidelines on the modelling aspects of ASR-affected reinforced concrete structures.

Chapter 7 presents the conclusions drawn from the analytical studies, and provides recommendations for future research.

Chapter 2 Literature Review

2 Literature Review

This chapter provides an overview of the development of advanced models and analytical procedures for ASR-affected concrete relevant to this thesis. The key objectives are: to describe the chemical mechanism of ASR, discuss the parameters that influence the reaction as well as the effects ASR has on the mechanical properties of concrete, and review representative mathematical models. The information in this chapter is not intended to be exhaustive, but rather it is presented to give background for the analytical procedures implemented in the VecTor programs.

2.1 The Chemical Mechanism of Alkali-Aggregate Reactions

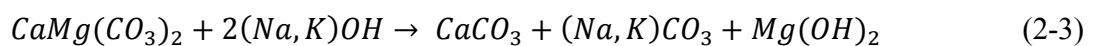
2.1.1 Alkali-Silica Reaction

The mechanism of ASR was originally described by Dent-Glasser and Katakoo (1981) and various other researchers addressed the problem thereafter (Chatterji and Christensen, 1990; Chatterji and Thaulow, 2000; Diamond, 1989; Urhan, 1987a, 1987b). According to Dent-Glasser and Katakoo (1981), in highly alkaline cement paste some of the silicate, aluminate or sulphate ions are balanced by Na^+ or K^+ instead of Ca_2^+ , resulting in abnormally high pH fluid in the paste. Two reactions were identified to contribute to this effect: hydrolysis of anions of weak acids and formation of insoluble calcium salts instead of calcium hydroxide. Both reactions produce hydroxyl ions (OH^-) which, in an environment of pH 7 or higher, penetrate together with sodium or potassium ions by diffusion into poorly crystallized silica aggregates, producing rupture of the siloxane groups (Si-O-Si). As such, silica dissolves in the presence of hydroxyl ions, at the beginning with the neutralization on the silanol groups (Si-OH) which are present at the surface (Eq. (2-1)), and then by the rupture of the siloxane groups (Eq. (2-2)). Figure 2.1 shows an illustration of the dissolution mechanism of silica minerals in the presence of hydroxyl ions.



2.1.2 Alkali-Carbonate Reaction

The alkali-carbonate reaction is less widespread compared to alkali-silica reaction, and therefore did not attract as much scientific interest. The alkali hydroxides present in the cement paste attack the dolomite constituent of carbonate rocks, resulting in the formation of calcite, alkali carbonates and brucite (Eq. (2-3)). The mechanism of expansion due to ACR is somewhat ambiguous. The dedolomitization reaction causes a reduction of volume, with several formulations having been proposed to explain the expansion process of the ACR affected concrete.



Earlier formulations (Gillot, 1964; Gillot and Swenson, 1969) consider the expansion to be primarily caused by the swelling of clay minerals present in the cement matrix. With the opening of access channels caused by the dedolomitization process, the unhydrated clay minerals become exposed to moisture and alkali. More recent studies revealed that ASR is at least a contributing factor to ACR expansion. Alkali-silica gel has been identified in concrete containing alkali-carbonate reactive aggregates. Experimental studies (Katayama, 2010; Grattan-Bellew et al., 2010) concluded that ACR is a combination of the expansive alkali-silica reaction and the dedolomitization reaction, dolomitic aggregates not being able to cause expansion unless ASR is involved.

2.2 Delayed Ettringite Formation

Delayed ettringite formation (DEF) is a form of sulfate attack common in concrete exposed to high temperatures during the curing process. The presence of products of both ASR and DEF have been identified during structure diagnoses. As such, several experimental studies were carried out to investigate the interaction between the two reactions (Shayan and Ivanusec, 1996; Bouzabata et al., 2012). Ettringite is a cement hydration product, formed as a result of the reaction of calcium aluminate with calcium sulfate. The formation of ettringite triggers a volume increase in fresh concrete but, due to concrete's plastic state, this expansion does not have a negative effect on concrete durability.

When fresh concrete is exposed to temperatures above 70°C, as a result of steam curing or due to high heat of hydration, the preliminary ettringite formation is inhibited. In time, the component

phases react and form ettringite. In the presence of moisture, the ettringite swells and causes severe cracking and expansion of the cement paste (Taylor et al., 2001).

Experimental investigations (Shayan and Ivanusec, 1996; Bouzabata et al., 2012) have shown that both elevated curing temperatures and sufficient moisture cause expansion of the ettringite, and the presence of reactive aggregates in the concrete mix influence the magnitude of induced expansion. Similar to ASR and ACR, DEF exhibits significant variation of the associated effects relative to environmental conditions, concrete mix, and exposure. Even though the chemical mechanisms differ, the reactions have proven to have similar deleterious effect on concrete.

2.3 Factors Influencing ASR

The key parameters influencing ASR are presented in this section. Temperature, water, alkali content, type of reactive aggregates, aggregate size, air entrainment and porosity, and finally stress level are reviewed and discussed in detail.

2.3.1 Temperature

Several experimental programs have been carried out to quantify the effect of temperature on ASR expansion and reaction rate: Chatterji and Christensen (1990), Bulteel et al. (2002), Larive (1997), Locher and Sprung (1973). Larive's and Bulteel et al.'s results matched the Arrhenius concept for the temperature dependence of reaction rate very well, thus simplifying the task of taking into account temperature effects when modelling ASR.

The influence of temperature on the reaction rate needs to be correlated with the induced expansion for a useful quantification from a structural point of view. The effect of temperature on expansion was determined through experiments performed at different temperatures on specimens with constant alkali content. The tests carried out by Locher and Sprung (1973) found a pessimum value of 38°C for which the expansion is the largest. Beyond this value, increasing the temperature resulted in a decrease of expansion. However, the tests performed with an unlimited amount of alkali on mortar prisms by Chatterji and Christensen (1990) revealed a decrease of the total expansion with the increase of temperature.

Urhan (1987a) explained that the rise in temperature diminishes the solubility of Ca(OH)_2 and increases the solubility of silica, conditions that increase the reaction up to 40°C. For higher

temperatures, it is assumed that the crystallization rate of CSH is more important than the dissolution of silica, this explaining the decrease of expansion rate with the increase of temperature beyond 40°C. Larive (1997) completes this theory by pointing out that in the case of increased alkali concentration with respect to calcium concentration, the alkali ions penetrate within the silica during its dissolution, increasing the volume. In this case, an increase of the temperature would lead to a reduction of the calcium concentration and therefore to an increase of the expansion rate.

2.3.2 Water

Water plays an important role in the deterioration of concrete affected by ASR since the alkali-silica gel swells only by water imbibition. Larive et al. (2000) studied the influence of water on ASR development by performing laboratory tests on cylinders kept at 38°C in four different storage conditions: immersed in water, in saturated humidity, in high but not saturated humidity (RH between 95% and 99%), and sealed in aluminum foil (no or low water loss). The longitudinal expansion and also the water intake were monitored.

The tests revealed that the expansion increases with the water intake. The cylinders kept in 95% to 99% RH showed a maximum expansion of 2.0×10^{-3} whereas the sealed ones exhibited an expansion of 1.0×10^{-3} . This led to the conclusion that even though external water supply increases the swelling of ASR-affected concrete, potential structural degradation may occur even without water ingress. The specimens containing reactive aggregates imbibed the same amount of water as the specimens containing non-reactive aggregates; therefore, the water movement in ASR-affected concrete is the same as for sound concrete.

Multon et al. (2005) and Multon and Toutlemonde (2010) conducted studies on both cylinder and beam specimens in order to characterize ASR-induced expansion due to variation of moisture conditions. Specimens kept at 100% RH or sealed under watertight aluminum foil for two years were submerged in water and specimens kept in water for two years were exposed to 30% RH. The study revealed that later intake of water causes further expansion of the specimens provided that the maximum potential expansion has not been reached.

2.3.3 Alkali Content

Even though Portland cement is the most important source of alkali in concrete, other materials such as aggregates, supplementary cementing materials, special admixtures, seawater and de-icing salts may contribute to the amount of alkali (Diamond, 1989). The quantity of alkali is expressed in terms of mass percentage of alkali, denoted by Na_2O -equivalent and equal to $\text{NaO}_2 + 0.658 \text{K}_2\text{O}$.

The ASTM C33 standard imposes a maximum limit of 0.60% alkali calculated as Na_2O -equivalent in the cement for concrete containing potentially reactive aggregates, the limit being based on Stanton's work. European standards set threshold values for the total alkali content in the concrete at 3 kg/m^3 . The Canadian standard CSA A23.1 sets limits between 1.7 and 3 kg/m^3 for the Na_2O -equivalent according to the type of structure built and to the exposure conditions, accounting for the alkali supplied by the cement, chemical admixtures and mix water.

However, the specifications do not take into account the contribution to the alkali content of the de-icing salts, seawater or aggregates. Studies carried out by Kawamura et al. (1988) and Sibbick and Page (1998) have shown that the environmental conditions of a concrete structure ought to be evaluated prior to choosing the concrete type. This is mainly due to the potential ingress of alkali ions originating from de-icing salts or seawater through moisture migration. Sibbick and Page (1998) showed how specimens initially containing Na_2O -equivalent below the limit of 3 kg/m^3 , as required by the U.K. standard, can exhibit ASR deleterious effects if in contact with NaCl solution. They found that even aggregates with low reactivity resulted in significant ASR in concrete with $3\text{-}4 \text{ kg/m}^3$ Na_2O -equivalent when immersed in concentrated NaCl solution.

In the study carried out by Chatterji et al. (1987) to quantify the effect of different alkali salts, potassium increased the rate of reaction more than sodium. It was also found that NaOH tends to dissolve the reactive aggregate rather than forming a gel, while the opposite phenomenon takes place when the alkali originates from NaCl . The latter conclusion was contradicted by the study carried out by Duchesne and Bérubé (2003), who found a larger expansion for the specimens immersed in NaOH solution than for those kept in NaCl . They also reported that the initial alkali content was not important for the specimens stored in NaOH ; the specimens with low alkali content and the ones with high alkali content all reached a 3.5×10^{-3} expansion after being kept for five

years in NaOH. The initial alkali content for the specimens stored in NaCl, though, was significant for the final expansion.

Bérubé et al. (2002) showed that significant amounts of alkali can be released with time by aggregates, especially by feldspar-rich ones. After 1.5 years the quantity of alkali released by the aggregates in 0.7 M alkaline solution, which is close to the pore solution in concrete, was significantly higher than the amount released in water or lime-saturated solutions. For an aggregate content of 1850 kg/m² the alkali released varied from less than 0.1 kg/m³ to 12.7 kg/m³ Na₂O-equivalent, with an average of 2.2 kg/m³. Constantiner and Diamond (2003) measured the concentration of alkali in both sound and reactive mortar specimens. Their conclusion was that feldspar within the cement matrix releases alkali ions which may participate in the ASR if reactive aggregates are also present. Another conclusion was that the release of alkali ions from aggregates may be masked by their participation in the reaction, the two processes being confused.

2.3.4 Type of Reactive Aggregate

Table 2.1 presents the list of deleteriously reactive rocks, minerals and synthetic substances according to ACI Committee 201 (1992). The type of reactive aggregates influences the reaction as some are rapidly reactive, while others react more slowly. Many rocks have silica as a component, but not all siliceous aggregates produce ASR. Mineral quartz is stable, whereas mineral opal is reactive. This difference is attributed to the microstructure; the mineral opal has a highly disordered structure which ends up vulnerable to alkali attack in high pH environment.

The silica minerals considered reactive are: opal, tridymite, cristobalite, volcanic glass, cryptocrystalline quartz and strained quartz; they may be found in the following rock types: shale, sandstone, silicified carbonate rocks, chert, flint, quartzite, quartz-arenite, gneiss, argillite, granite, greywacke, siltstone, arenite, arkose, and hornfels. The reactivity of the aggregates was found to be influenced by the presence of reactive minerals within (Thomas et al., 2013). The presence of reactive minerals is usually detected through petrography tests.

Table 2.1 – Deleteriously Reactive Rocks, Minerals and Synthetic Substances (adapted from ACI Committee 201, 1992)

Reactive substance (mineral)	Chemical composition	Physical character
Opal	$\text{SiO}_2 \cdot n\text{H}_2\text{O}$	Amorphous
Chalcedony	SiO_2	Microcrystalline to cryptocrystalline; commonly fibrous
Certain forms of quartz	SiO_2	Microcrystalline to cryptocrystalline, crystalline but intensely fractures, strained and/or inclusion-filled
Cristobalite	SiO_2	Crystalline
Tridymite	SiO_2	Crystalline
Rhyolitic, dacitic, latitic, or andesite glass or cryptocrystalline devitrification products	Siliceous with lesser proportions of Al_2O_3 , Fe_2O_3 , alkaline earths and alkalis	Glass or ctyptocrystalline material as the matrix of volcanic rocks or fragments in tuffs
Synthetic siliceous glass	Siliceous with lesser proportions of Al_2O_3 , and/or other substances	Glass

2.3.5 Aggregate Size

The size of the reactive aggregate particles proves to be of great influence regarding the rate of reaction and the expansion of concrete. Diamond and Thaulow (1974) showed that aggregate sizes ranging between 20 μm and 30 μm induce larger expansion than coarser aggregates. In addition to this, the rate of reaction is also increased. For mortar specimens with aggregates of size 20 μm - 30 μm , the expansion process terminated in a few months; specimens having the same type of reactive aggregates but coarser, 125 μm , experienced a more prolonged and gradual expansion. Hobbs and Gutteridge (1979) also studied the influence of particle size with opaline rocks as aggregates, having fractions between 150 μm to 4.8 mm. Their conclusion was that expansion becomes larger with the decrease of aggregate particle size. This effect was particularly pronounced for opaline content in the range 4% to 6% of the total amount of aggregates.

Kuroda et al. (2004) found that expansion increases with the decrease of aggregate particle size. They tested specimens kept in NaOH solution inside an autoclave apparatus. A correlation between the total surface of the reactive aggregate and the expansion was observed, regardless of particle size. Jin et al. (2000) and Shayan and Xu (2004) have shown that the expansion of concrete containing reactive recycled glass as an aggregate can be significantly reduced provided that the glass is crushed to a certain size, depending on its type.

2.3.6 Air Entrainment and Porosity

The ASR-induced expansion is highly reduced provided that a network of well distributed pores exists in the concrete matrix. Even though the reaction rate is not influenced, the swelling of the gel is accommodated by the pores and therefore the expansion of concrete is reduced (Hobbs, 1988). This phenomenon is similar to the beneficial effect of air entrainment in the case of concrete exposed to freeze-thaw cycles; well distributed pores provide space for the expansion of water in the freezing process, avoiding damage. Similar results were obtained in the experimental study carried out by Jensen et al. (1984), which showed a reduction of 40% of the expansion when 4% air was introduced in the mortar specimen.

Increased porosity of the cement has the same effect on reducing the induced expansion as air entrainment. Collins and Bareham (1987) showed that by using porous aggregates the expansion and damage caused by ASR is reduced. Their conclusion was that the alkali-silica gel is partially accommodated within the porous aggregate but more importantly, a reduced amount of gel is produced due to the dilution of the alkali by the water absorbed by aggregates.

2.3.7 Stresses

Several experimental programs were performed to determine the influence of stress level on the expansion of concrete affected by ASR. A comprehensive study was carried out by Larive (1997) regarding the influence of uniaxial loading on the expansion of ASR-affected cylinders with a diameter of 130 mm and 240 mm height. The nominal compressive strength of the sound concrete was 39.8 MPa while the compressive strength for the reactive concrete was 45.8 MPa. Both transversal and longitudinal expansions were measured for specimens loaded at 0 MPa, 5 MPa, 10 MPa and 20 MPa.

The specimens loaded uniaxially at 20 MPa presented no longitudinal deformation due to ASR. Longitudinal expansion was significantly reduced for the specimens loaded at 5 MPa and 10 MPa: from 2.0×10^{-3} for the unloaded specimens, to 0.23×10^{-3} and 0.14×10^{-3} respectively. Additionally, the cracks were wider in the case of the loaded specimens (0.20 mm – 0.30 mm) in comparison to the unloaded ones (0.05 mm – 0.10 mm), oriented in the direction of the principal loading. Regarding the transversal expansion, the specimens loaded at 10 MPa presented the largest expansion compared to the free expansion specimens, followed by the cylinders loaded at 5 MPa. The specimens loaded at 20 MPa, however, presented the lowest expansion. This was attributed to the fact that significant micro-cracks formed, accommodating the reaction product causing expansion.

For a better comparison of the expansion of specimens subjected to loading to those under free expansion, the volumetric expansion is presented in Table 2.2. The volumetric expansion was calculated considering that the deformed specimen maintains the cylindrical shape. As may be observed, the volumetric expansion of the specimens loaded at 5 MPa and 10 MPa is comparable to the free expansion; the deformations suppressed in the direction of the loading are transferred to the perpendicular directions. The volumetric expansion of the specimens loaded at 20 MPa is significantly reduced due to the mechanical micro-cracks that develop. The behavior of the specimens upon unloading was also studied by Larive (1997). Both longitudinal and transversal deformations were similar to the specimens subjected to free expansion from the beginning.

Table 2.2 – Comparison of deformations of free expansion specimens versus uniaxially loaded specimens (adapted from Larive, 1997)

	0 MPa	5 MPa	10 MPa	20 MPa
Average longitudinal expansion ($\times 10^{-3}$)	1.99	0.23	0.14	-0.03
Average transversal expansion ($\times 10^{-3}$)	1.02	1.53	2.08	1.25
Average volumetric expansion ($\times 10^{-3}$)	4.03	3.29	4.30	2.47

Another significant study was carried out by Multon and Toutlemonde (2006). Several different states of stresses were applied to cylinders having identical geometric dimensions as the ones tested by Larive (1997): 130 mm diameter, 240 mm height. The axial loading was applied by a flat hydraulic jack while the radial loading was applied by steel rings of different thicknesses. For the specimens loaded only longitudinally, two levels of loading were used: 10 MPa and 20 MPa. The free expansions of reactive and non-reactive concrete were also studied.

The ASR-induced expansion was reduced from 1.0×10^{-3} to 0.3×10^{-3} when 10 MPa or 20 MPa stress was applied, while the radial strains increased, which is explained by an 'expansion transfer'; the ASR gel expands in the transverse, less compressed direction. Three types of tests were performed for the confined specimens: with no axial loading, 10 MPa loading and 20 MPa applied loading. The results showed that, for the specimens without axial loading, the axial ASR expansion was between 1.0×10^{-3} and 1.5×10^{-3} for specimens confined with 3 mm and 5 mm rings. The specimens that were loaded presented larger creep strains than ASR expansion, and therefore, the deformations were negative: -0.3×10^{-3} for 10 MPa and -0.75×10^{-3} for 20 MPa, compared to 0.75×10^{-3} and 1.70×10^{-3} for the same loading on unrestrained specimens.

The conclusions from their study were the following: the ASR volumetric imposed strain can be considered as constant, regardless of the stress state; and, in loaded/restrained concrete, ASR-induced expansions are transferred in the less compressed direction.

2.4 Changes in Mechanical Properties

This section discusses changes in the mechanical properties caused by ASR. The reaction-induced expansion causes internal stresses which usually lead to cracks, damage of the concrete and deterioration of its initial properties. The effect of ASR on compressive strength, flexural strength and stiffness are presented in the following subsections.

2.4.1 Effect on Compressive Strength

Multon et al.'s (2005) experimental study showed no decrease in the compressive strength caused by ASR for cylindrical standard specimens. Similar conclusions were reached by Larive (1997) and Monette (1999). The negative effect of ASR on the compressive strength of concrete was found, in all these studies, to be counteracted by the hydration process. However, investigations conducted by Giaccio et al. (2008) and Swamy and Al-Asali (1988) concluded that ASR decreases the compressive strength once the induction period of ASR is finished. Giaccio et al. (2008) tested various types of reactive concrete showing that in the case of rapidly evolving ASR, the concrete presents no strength gain with time. A loss in compressive strength of 12% was reported for 1.0×10^{-3} linear expansion in the case of highly reactive aggregates, whereas the slow evolving aggregates did not affect the compressive strength.

The differences in results are attributed to differences in concrete mixtures, particularly in regards to reactive aggregates. Swamy and Al-Asali (1988) tested the effect of ASR on compressive strength of specimens containing opal or fused silica. Both concretes showed initially an increase in strength followed by a gradual decrease: opal at 10 to 20 days and fused silica at 2 months. The loss in compressive strength related to expansion is presented in Table 2.3.

Table 2.3 – Percentage loss in compressive strength of ASR-affected concrete (adapted from Swamy and Al-Asali, 1988)

Linear expansion ($\times 10^{-3}$)	4.5% opal		15% fused silica	
	Age (days)	Loss (%)	Age (days)	Loss (%)
0.5	6	9	40	12
1.0	8	11	60	11
2.0	17	20	87	15
4.0	36	27	140	30
6.0	60	30	200	40
10.0	117	38	-	-
16.0	270	62	-	-

2.4.2 Effect on Tensile Strength

ASR significantly reduces the tensile strength of concrete due to induced cracking. Studies carried by Swamy and Al-Asali (1988) have shown that the tensile strength is the most negatively affected mechanical property of concrete. Table 2.4 shows the loss in tensile strength with expansion as obtained from the experimental study carried by Swamy and Al-Asali (1988). The modulus of rupture and the tensile splitting tests were performed on specimens containing fused silica. Compared to the compressive strength, the tensile strength is more sensitive even at early ages. Visible cracking were observed at 0.5×10^{-3} expansion but it can be observed that loss in flexural strength occurred before this point.

Giaccio et al. (2008) obtained similar results regarding the tensile strength. In addition, their study showed that in the case of slow-reactive aggregates, the decrease in tensile strength is not as dramatic as in the case of highly reactive aggregates.

Table 2.4 – Percentage loss in tensile strength of ASR-affected concrete (adapted from Swamy and Al-Asali, 1988)

Linear expansion ($\times 10^{-3}$)	Age (days)	Loss of tensile strength (%)	
		Modulus of rupture	Indirect tensile ¹
0.2	27	11	11
0.4	36	20	19
0.5	40	30	27
0.6	45	29	23
0.8	54	40	26
1.0	60	48	29
1.5	75	56	38
3.0	110	67	55
6.0	200	78	64

¹from split cylinder test

2.4.3 Effect on Modulus of Elasticity

The degradation of the elastic modulus of ASR-affected concrete is significant, ranging between 20% and 70%. The stiffness loss is correlated with the expansion of concrete and therefore with the severity of the reaction (Giaccio et al., 2008; Multon et al., 2005; Swamy and Al-Asali, 1988). The results of the experimental study led by Swamy and Al-Asali (1988) are shown in Table 2.5, the conclusion being that the loss in elastic modulus has the same trend as the loss in tensile strength.

As also pointed out by Multon et al. (2005), the hydration process counteracts to some extent the damaging effect of ASR. This is reflected in the change of elastic modulus. In the case of the specimens containing opal, the linear expansion increased from 3.16×10^{-3} at 28 days to 8.83×10^{-3} at 100 days while the loss in elastic modulus was from 51% to 56%. During this period the water absorption increased from 0.147 kg to 0.410 kg. Like other properties, the loss in modulus of elasticity depends on the type of reactive aggregates and on the rate of reaction.

Table 2.5 – Percentage loss in elastic modulus of ASR-affected concrete (adapted from Swamy and Al-Asali, 1988)

Age (days)	4.5% opal		15% fused silica	
	Expansion ($\times 10^{-3}$)	Loss (%)	Expansion ($\times 10^{-3}$)	Loss (%)
2	0.00	4.6	0.00	2.7
7	0.71	20.3	0.00	3.8
10	0.97	42.3	0.05	2.3
28	3.16	51.1	0.23	4.0
100	8.83	55.8	2.59	45.7
204	14.42	74.7	6.15	68.0
300	16.18	81.9	6.25	59.8
365	16.44	77.1	6.23	58.4

2.5 Constitutive Models for ASR

The expansion of concrete generated by ASR causes a new set of stresses which may lead to mechanical and structural changes in the behaviour of concrete. The study of ASR is complicated by its heterogeneous character and by the fact that the solid participating in the reaction encloses in its pores the liquid in the reaction, the reactive solid being a small and irregularly distributed part of the total solid.

A comprehensive model should address the following basic aspects: the kinetics of the reaction and the diffusion process, the mechanical damage caused by the expansion due to ASR, and the evaluation of ASR-induced strains. As ASR is influenced by many factors, it is difficult to formulate a model which encompasses all the variables. Therefore, several theoretical, semi-empirical and numerical constitutive models have been developed to reproduce the ASR effect at a material or structural scale. Depending on the level at which the ASR is described, three types of models can be identified: micro-models, meso-models and macro-models.

2.5.1 Micro-Models

In micro-models, the emphasis lies in the transport equations for the reactants and the diffusion processes in order to quantify the gel formation and its swelling, the aggregate and the cement paste being modeled separately. Even though this type of modelling has little relevance on the structural analysis of elements affected by ASR, it is important for properly understanding the whole phenomenon causing ASR.

Hobbs (1981) proposed a model for predicting the expansion in mortar which assumed the reaction rate is directly proportional to the quantity of reactive aggregates, accounting also for the alkali concentration in the pore water. This model predicted the expansion of the mortar bars containing opaline silica, and the time to cracking in relatively good agreement with the observed experimental data.

Groves and Zhang (1990) developed a dilatation model for mortar containing silica glass particles assuming (a) the matrix surrounding the reactive aggregate may be treated as a solid continuum, (b) all the silica in the reacted glass becomes located in the gel, and (c) the main ASR product is located at the surface of the silica glass particle. Regarding the mechanical aspect, the authors used the model of a spherical aggregate particle. The expansion of the mortar was predicted by estimating the volume increase by elasticity theory of a misfitting sphere in the matrix.

Several authors combined this dilatation model with diffusion theories in order to predict the ASR-induced expansion. Svensson (1991) assumed diffusion governed by the Fourier parabolic heat equation for a sphere embedded in a continuum with elastic properties, modelling cracks due to ASR as caused by diffusion generated eigenstresses. In the following subsections some of the most relevant micro-models are presented.

2.5.1.1 Mathematical Model for Kinetics of ASR: Bazant and Steffens, 2000

Bazant and Steffens (2000) developed a model addressing the kinetics of alkali-silica reaction with the associated diffusion processes that analyzes the moisture diffusion on pessimum size taking into account the nonlinear coupled diffusion of water within concrete. The model simplifies the microstructure of concrete with a periodically repetitive cubic cell containing one reactive particle, as shown in Figure 2.3. Two separate micro-diffusion processes of water are considered: the diffusion towards the surface of the aggregate, which has not reacted yet, through ASR gel; and the diffusion of water towards the ASR gel, causing its expansion. The gel expansion is resisted by the surrounding concrete once the pores are filled, a phenomena which inhibits water imbibition.

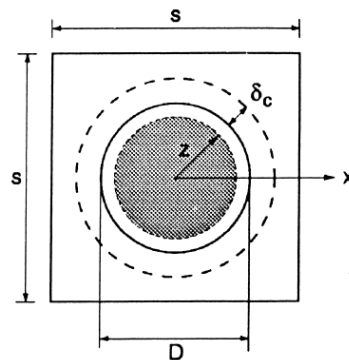


Figure 2.3 – Idealized repetitive cubical cell with one reactive particle of original diameter D (the remaining unreacted particle of radius z is marked gray, δ_c =thickness of layer with capillary pores and cracks into which pressurized ASR gel formed intrudes by diffusion) (adapted from Bažant and Steffens, 2000)

The diffusion of water through the increasing gel towards the unreacted surface of the aggregate is assumed to be governed by Fick's law; therefore the radial flux of water depends on the concentration of water within the ASR gel layer and on the permeability of ASR gel to water. The radial profile of the water concentration within the ASR gel is determined as the solution to the steady-state diffusion equation, followed by the calculation of the velocity of the reaction front. Finally, the mass of gel produced per cubic meter of concrete is determined as a function of the volume of reacted aggregates.

The swelling of the formed gel is assumed to be caused by the imbibition of additional water, which is treated as a local micro-diffusion process, whose geometry is no longer spherical. This is due to the fact that the expansion of ASR gel takes place partially in the capillary pores of the cement paste located near the surface of the particle and partially in the interstitial layer with higher porosity near the aggregate. The water imbibition rate is determined as a function of the thermodynamic affinity, mass of basic gel, diffusivity of water and thickness of the ASR gel.

As the alkali-silica reaction depends on the water supply, the macro-diffusion of water through concrete is also modeled. This diffusion is governed by a linear Darcy's law, depending on the permeability of concrete and the relative vapor pressure. The solution of the system of differential equations constituting this model was achieved numerically, showing the existence of a pessimum size and agreeing with previous research studies (Jin, 1998).

2.5.1.2 Fracture Mechanics of ASR - Bazant et al., 2000

A fracture mechanics model was proposed by Bazant et al. (2000) aiming to explain the pessimum size and the pessimum expansion by fracture mechanics alone. This model is suited for concrete with waste glass particles, tested by Jin (1998). The kinetics of the reaction and the diffusion processes were simplified in order to keep the fracture analysis simple.

The microstructure of concrete is modelled as a regular array of cubical cells, each one containing one spherical glass particle embedded in the cement mortar. The expanding ASR gel, assumed to be present only at the surface of the glass particle, causes radial pressure on the surrounding cement mortar, leading to cracks (Figure 2.4).

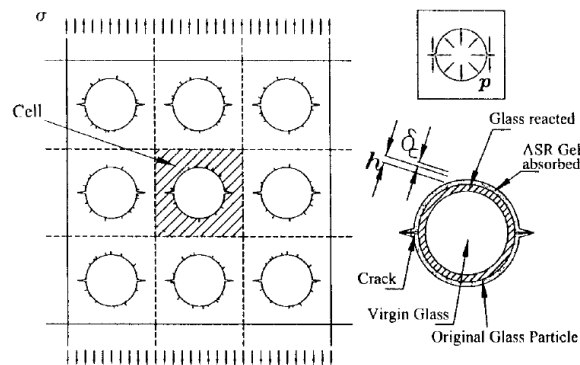


Figure 2.4 – Idealized cubic array of expanding spherical glass particles surrounded by flaws and dominant growing cracks filled by ASR gel (left); Cell with glass particle and crack (right top); Layer of reacted glass and layer of ASR gel forced into capillary pores of concrete (right bottom) (adapted from Bazant et al., 2000)

The crack planes are assumed to be parallel in all cells. Therefore, the analysis can be reduced to a single cubical cell, a ring crack being assumed to cause the expansion (Figure 2.5.a). The stress field caused by the pressure generated by the gel swelling on the crack is assumed to be a superposition of the stress field caused by the hydrostatic stress applied by the gel and the stress field caused by externally applied tensile stresses (Figure 2.5.b). Two stages of crack evolution are identified: edge crack in an elastic half-space in the initial stage, and small circular uncracked ligaments in the final stage.

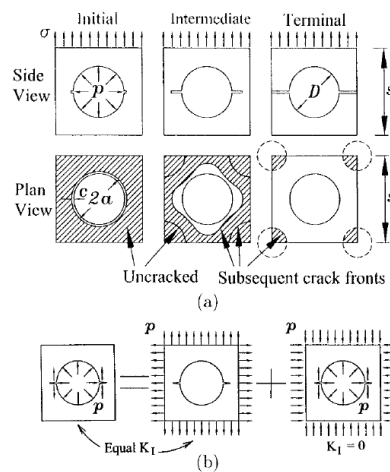


Figure 2.5 – (a) Idealized evolution of crack front from initial stage of shallow cracks to terminal stage of small circular uncracked ligaments. (b) Superposition revealing equivalence of crack pressurization and stress externally applied on one cell (adapted from Bazant et al., 2000)

The crack growth was characterized by a damage variable which depends on the area of the crack and on the size of the cell. The deformation of the cell can be integrated analytically on the basis of the stress intensity factor solution. The calculation of the pressure is assumed to be based on the condition of compatibility of the volume expansion of ASR, the change of volume of the crack and the volume of the gel fitted in the capillary pores. The numerical solution of the model was in good agreement with the experimental data to predict the volume expansion as a function of particle size, but inadequate for estimating the compressive strength.

2.5.1.3 Mathematical Model - Suwito et al., 2002

The model developed by Suwito et al. (2002) is a mathematical model developed to evaluate the pessimum expansion and the pessimum size. Jin (1998) demonstrated that only up to a specific particle size does the volume expansion increase with the decrease of particle size. The presented model comprehends the chemo-mechanical coupling of the ASR expansion, the size distribution of aggregates and the micro-structural characteristics of the cement paste.

The limiting assumption is elastic behaviour for all the constituent materials; therefore it is not suited for severe reactions and cracking due to ASR, and the model is applicable only to fully saturated concrete. The theoretical model comprises two parts: the first part is the application of a composite theory for the expansion and pressure generated by ASR, and the second part is the

application of different diffusion theories in order to simulate the dominant diffusion process during ASR.

The mechanical part of the composite model for ASR expansion is based on the multiphase generalized self-consistent method. The basic element is a two-phase composite sphere: the interior sphere represents the aggregate, and the exterior one represents the cement paste. The ASR gel is included as part of the aggregate. This is due to the fact that each phase is assumed to have a fixed volume fraction in each element and considering the gel as a distinct phase would result in different volume fractions of gel for different aggregate sizes.

In this model the chemical part includes two opposing diffusion processes which occur simultaneously: diffusion of the hydroxyl and alkali ions into the aggregates, and the permeation of the ASR gel into the surrounding cement paste. The diffusion of the chemical ions has two stages: macro-diffusion of the ions into the specimen, and micro-diffusion of the ions within the aggregate. The micro-diffusion of chemical ions into aggregate is governed by Fick's law, accounting for the free ion concentration of the pore solution inside the aggregate, binding capacity and ion permeability of the aggregate. In this way the volume of the reacted aggregate is determined, followed by the calculation of the gel volume. Expansion is assumed to be initiated when the volume of alkali-silica gel overcomes the volume of the pores of the interfacial transition zone. Darcy's law for viscous flow is used to characterize the generated interface pressure, taking into account the concentration, viscosity of the gel, permeability of the cement paste and the pressure distribution in the gel.

The pressure distribution in the gel can be determined by solving the boundary condition for the sphere with the interfacial pressure applied. As the interfacial pressure is a function of time that needs to be evaluated simultaneously from the equilibrium of the system, the diffusion of the ions and the permeation of the gel, its solution depends on a state relation between the pressure distribution and the concentration of the gel. A state function for the cement paste, which is determined from the state of saturation, is introduced. The gel volume in the cement paste is then evaluated by integrating the gel concentration over the surrounding cement paste. The volume change generates an interfacial pressure which must be equal to the interfacial pressure from the equilibrium of the composite system. The solution of the proposed model can be pursued numerically.

2.5.1.4 Chemo-mechanical micro-model for ASR - Puatatsananon and Saouma, 2013

The chemo-mechanical micro-model for ASR proposed by Puatatsananon and Saouma (2013) is a modified version of the mathematical model developed by Suwito et al. (2002). This model overcomes the original limitations as it represents a nonlinear coupled formulation including the effects of internal moisture and ion concentration on the transport properties of concrete.

The authors identify three different diffusion processes, similar to the ones in the original model: the macro-diffusion of alkali, which is the diffusion of the ions into the specimen; the micro-diffusion of alkali, representing the penetration of chemical ions inside the aggregate (Figure 2.6); and the micro-diffusion of gel through the porous cement paste.

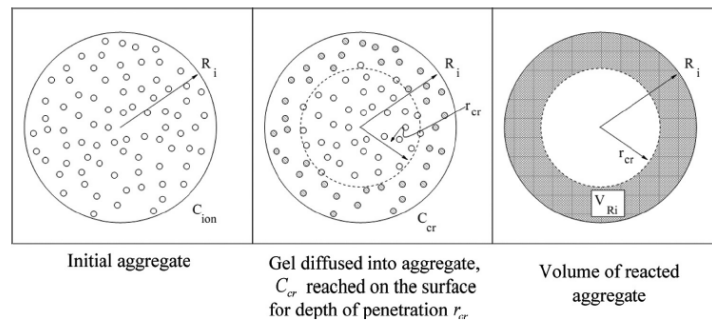


Figure 2.6 – Ion diffusion into aggregate (adapted from Puatatsananon and Saouma, 2013)

When determining the volume of the reacted aggregate by using Fick's law to describe the micro-diffusion of the ions inside the aggregate, a simplified linear model is assumed for the ion diffusivity. Suwito et al. (2002) assumed the ion diffusivity as being constant when it actually decreases with the formation of gel, depending on the porosity of the cement paste, the gel concentration and the saturated state of the gel. The volume of ASR gel is determined from the volume of the reacted aggregate, taking into account the relative humidity.

The gel diffusion through the porous cement paste (Figure 2.7) is described by Darcy's law, assuming the gel permeability and viscosity of the gel to be constant. The gel volume that will cause the transient internal pressure and the coefficient of ASR expansion are evaluated assuming that the swelling of the aggregate is generated only by the gel outside the interface zone. The interface pressure is determined by solving the equilibrium of the composite system and must be

equal to the pressure distribution due to ASR gel from Darcy's law, the solution being pursued iteratively.

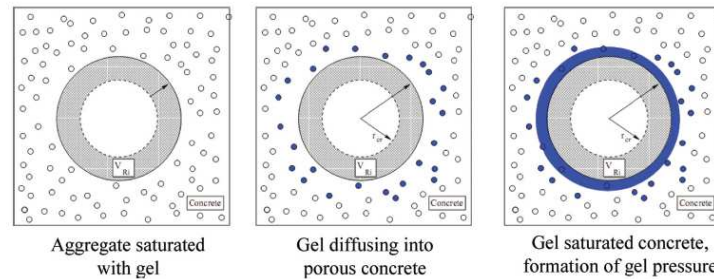


Figure 2.7 – Gel diffusion into cement paste (adapted from Puatatsananon and Saouma, 2013)

2.5.1.5 Delft Lattice Model

The Delft Lattice Model, proposed by Schlangen and Garboczi (1997), is a model in which the material is discretized into a lattice of beam elements with 3 degrees of freedom at each node, transferring normal and shear forces and bending moments (Schlangen and Van Mier, 1992; Çopuroğlu and Schlangen, 2007). Fracture is simulated by performing a linear elastic analysis under loading conditions and removing the element that exceeds a certain imposed threshold for elastic energy or tensile strength. The heterogeneity of concrete is taken into account through the use of digital images of the real material. The interfacial transition zone is modelled by adjusting the tensile strength and the modulus of elasticity of the beam elements that fall in that region. The fracture criterion proved to strongly influence the results obtained from simulations with lattice models. The use of the fracture law in which the stress is calculated at the nodes of the lattice, rather than in the beam, predicted better results for uniaxial tensile loading, tensile splitting and compression.

Schlangen and Çopuroğlu (2007) proposed a model to simulate the crack patterns and deformations in concrete due to ASR based on the Delft Lattice Model. The missing parameter for modelling ASR is the force resulting from the swelling of the alkali-silica gel and therefore the stresses generated by it. To account for this, the authors suggested a new measuring device to measure the free deformation of the concrete due to ASR and also the stresses in the case when the deformation is restrained.

Çopuroğlu and Schlangen (2007) simulated ASR mechanism by creating a model with a single aggregate particle surrounded by cement paste. The alkali-silica gel was placed in three locations: within the aggregate, at the interfacial transition zone, and in the cement paste, assuming these three locations expand at the same rate. Strength and stiffness values for the beam elements were randomly chosen from the specified ranges in Table 2.6. Figure 2.8 shows the results from the simulation; the predicted crack pattern is similar to the real one.

Table 2.6 – Strength and stiffness of components used in lattice simulation (Çopuroğlu and Schlangen, 2007)

	Aggregate	Dissolved rim of aggregate	Interfacial transition zone	Cement matrix	ASR gel
Strength (MPa)	7.0-13.0	1.0-2.0	1.5-2.5	3.0-5.0	1.0
Stiffness (MPa)	70,000-130,000	10,000-20,000	15,000-25,000	30,000-50,000	10,000

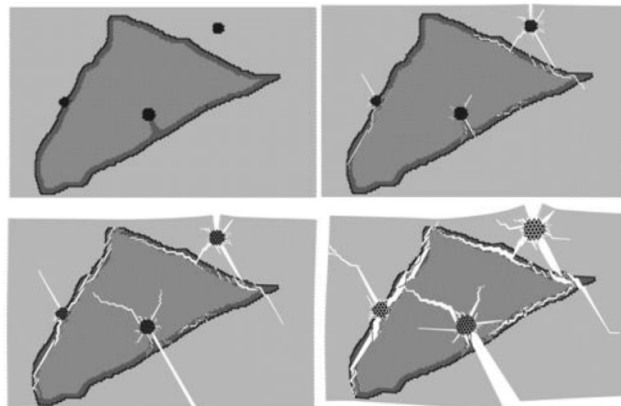


Figure 2.8 – ASR damage sequence according to Delft Lattice Model (adapted from Çopuroğlu and Schlangen, 2007)

2.5.2 Meso-Models

The meso-models are focused on dimensions between 1 cm and 10 cm, a scale which encompasses the aggregates, the interfacial transition zone and the cement paste. At this level, the concrete is modelled as a heterogeneous material with the aim to better understand and capture the local mechanisms of deformation and their effect on the changes on the microstructure. Several meso-scale models are available in the literature and they mainly differ regarding the mechanism considered for the ASR-induced expansion which may be homogenized aggregate expansion, gel rim expansion or gel pockets expansion.

Comby-Peyrot et al. (2009) proposed a model in which ASR expansion is simplified based on an isotropic dilatation of the reactive aggregates. Dunant and Scrivener (2010) developed another model which simulated the expansion as being induced by growing pocket gels within the aggregate. Finally, the model developed by Pan et al. (2012) considers the gel formation in the interfacial transition zone, adopting the model proposed by Bazant and Steffens (2000) previously described as a micro-scale model. Dunant and Scrivener (2010) carried out simulations showing that the macroscopic expansion and damage are strongly linked to the localization of the reaction at the micro structural level.

2.5.2.1 Dunant and Scrivener, 2010

Dunant and Scrivener (2010) proposed a model in which damage is introduced by growing gel pockets in the aggregates. The model is physically-based and emphasizes the predominant effect of gel formation within the aggregates damaging the aggregates themselves. The damage introduced by the gel causes the loss of mechanical properties and the model is used to predict their evolution. The proposed model shows robustness to variation of the apparent gel stiffness.

The authors conducted an experimental study which was intended to be an extension of the experimental investigation carried out by Haha et al. (2007). The expansion of concrete and mortar specimens containing moderately reactive aggregates at different temperatures was monitored. The image analysis methodology proposed by Haha et al. (2007), Scanning Electron Microscopy Image Analysis (SEM-IA), was used to quantify the degree of the reaction. The ratio of the aggregate surface to void surface was used to measure the reaction progress directly. The relation found by Haha et al. (2007) between the expansion and the reacted fraction was confirmed by the experimental study carried by Dunant and Scrivener (2010). A renormalization function was derived accounting for the aggregate fraction which allowed the comparison between samples with different grain size distribution.

A finite element framework of the model was proposed in which spherical aggregates are used and which generates the microstructure of concrete through a random packing algorithm. A dense network of cracks induces the damage in the meso-scale model. Both the paste and aggregates are considered as quasi-brittle, and for this reason, the damage evolution law is the following:

$$d^{i+1} = \max(d^i + e^{\eta d^i}, 1 - \varepsilon) \quad (2-4)$$

where d is a factor such that the modulus of elasticity, E , is related to the initial modulus, E_o , by:

$$E = (1 - d)E_o \quad (2-5)$$

The failure criterion adopted is a modified Mohr-Coulomb criterion which was validated by the fact that it produces failure patterns similar to the experimental observed ones from a morphological point of view. The damage is incremented when the failure criterion is reached. A parameter, s , is defined to allow inter-elements comparison and to determine which elements are to be damaged at each step. The parameter is calculated as:

$$s = 1 - \frac{\sigma_{max}}{\sigma_{crit}} \quad (2-6)$$

The model considers explicitly the gel pockets within the aggregates, which are modeled using a soft-discontinuity type of enrichment. The enrichment function simulates a perfect contact between materials of different mechanical properties and was introduced by Moes et al. (2003):

$$\phi(\mathbf{x}) = 1 - \left| \mathbf{x} - \text{proj}_{\Gamma_{gel}} \mathbf{x} \right| \quad (2-7)$$

where Γ_{gel} is the gel boundary, proj is the projection operator and \mathbf{x} are coordinates in the global system.

The gel properties are assumed to be linear elastic with an imposed strain from the surroundings until large amounts of damage have occurred. The gel is assumed to be quasi-incompressible, with a Poisson's ratio equal to that of water and stiffness equal to a fraction of that of the calcium silicate hydrate (C-S-H). The free expansion of the gel was obtained by fitting the early part of the free expansion-damage curve and it was found that 50% of the volume expansion fits the experiments. The strain of the gel ε_{imp} is imposed as a virtual force on the nodes of the elements inside or cut by the gel pockets. The associated force is of the following form:

$$f_i = \int_{\Omega_{gel} \cap e} \nabla h_i E \varepsilon_{imp} d(\Omega_{gel} \cap e) \quad (2-8)$$

where Ω_{gel} is the gel surface, e is the element surface, h_i is the shape function associated with the considered degree of freedom and E is the Cauchy-Green stress tensor of the gel.

The expansion is computed against the degree of reaction, and as a result the mechanical model does not take into account time-dependent behavior depending on curing conditions such as gel flow or creep. Therefore, the predicted expansions are expected to be higher than the ones in the later stages of the reaction.

The gel is increased by steps in every aggregate until a certain percentage of the aggregate has reacted (3%), at which point the reaction in the aggregate is stopped. Simulations were run with all gel pockets growing in the same way, regardless of their location; by the end of the run, nearly half of the aggregates exhausted their expansion potential. Expansions up to 10×10^{-3} were simulated and, at this level, significant damage occurred. The expansion-reaction curves obtained from simulation matched the experimental ones with fitting the stiffness and free expansion of the gel.

The model explains the loss of stiffness as being caused by aggregates cracking, which is consistent to the microscopic observations. Paste failure occurs when the cracks within the aggregates reach the paste. The loss of stiffness proved to be sensitive to the choice of gel properties.

2.5.3 Macro-Models

The emphasis of macro-models lies with the global behavior of a structure affected by ASR taking into consideration the displacements, the stresses and the deleterious cracking. There are numerous models in the literature; the majority of them were formulated within the framework of a finite element method. Some models decouple the structural modelling from the reaction mechanism, other models couple them, and other models ignore reaction kinetics. The reaction kinetics is typically based on experimental studies while the behavior of concrete is simulated as either linear elastic or nonlinear. Macro-models are used to predict the long-term behaviour of concrete structures which are identified to suffer from ASR and to quantify their durability.

2.5.3.1 Parametric model - Leger et al., 1996

Leger et al. (1996) proposed a numerical model to distribute the observed concrete expansion in proportion to the compressive stress state, temperature, moisture and reactivity of the constituents. Expansion factors (Figure 2.9), which vary from 0.0 to 1.0, represent these effects on the ASR expansion.

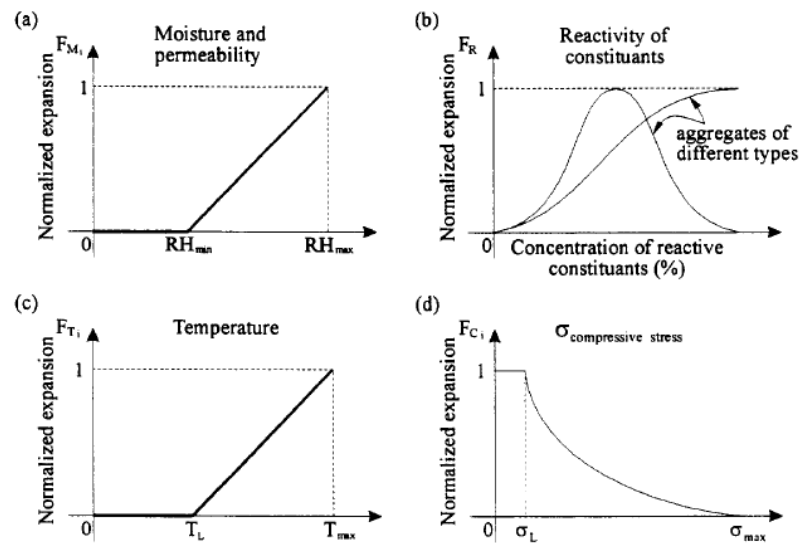


Figure 2.9 – Factors influencing ASR concrete expansion (adapted from Leger et al., 1996)

The normalized expansion factors are determined on the basis of empirical methods. The relative humidity (Figure 2.9.a) has to be approximately 75% to initiate significant expansion and the magnitude of the expansion is assumed to vary linearly between 75% and 100% RH. As the analysis of water transport is very complex, especially when several sources of water are involved, the authors suggest using a value of 1.0 for F_M .

The reactivity of the constituents (Figure 2.9.b) can be assessed by identifying the total alkali content and the total amount of reactive aggregates. As in a massive concrete structure large heterogeneity is expected to be encountered, an attempt to estimate accurately the magnitude and spatial distribution of the reactive material is rather difficult. Therefore, the method assumes there will be no global differential expansion of the concrete structure due to reactivity of the constituents; the alkalis content, type and size of the aggregates are considered homogenous throughout the structure, thus $F_R=1.0$.

The evolution of the temperature field during a year is suggested to be performed through finite element heat transfer analysis. In thinner sections, where the seasonal temperature variations penetrate to the full depth, there will be no significant temperature effects on an annual average basis other than a separation between the submerged zone and the zone exposed to air.

The expansion and damage due to ASR is significantly influenced by the applied stresses, with expansion being reduced in the direction of the compression. In the present model, the concrete swelling ε_g is related to the compressive stress σ_i , with the following expressions being applicable in the three principal directions independently of each other, as proposed by Charlwood et al. (1992):

$$\varepsilon_g = \begin{cases} \varepsilon_u, & 0 \leq \sigma_i \leq \sigma_L \\ \varepsilon_u - K \log_{10} \frac{\sigma_i}{\sigma_L}, & \sigma_L < \sigma_i \leq \sigma_{max} \\ 0, & \sigma_i > \sigma_{max} \end{cases} \quad (2-9)$$

where

ε_g = restrained growth rate

σ_i = principal stress in direction i

ε_u = unrestrained concrete growth rate at zero stress (free expansion)

σ_L = stress below which ε_g is equal to the free expansion rate (approximately 0.3 MPa)

σ_{max} = stress above which concrete ε_g is zero (between 5 and 10 MPa)

K = slope of the line defining the concrete growth rate versus log-stress.

A normalized version of this model is shown in Figure 2.9.d. The constitutive models relating the growth of the strain to stresses have to be determined iteratively.

Figure 2.10 shows the method for determining the spatial distribution of ASR-induced expansion. An anisotropic non-uniform growth rate is simulated, starting with the evaluation of the normalized expansion factors which are then combined to determine the expansion caused by ASR.

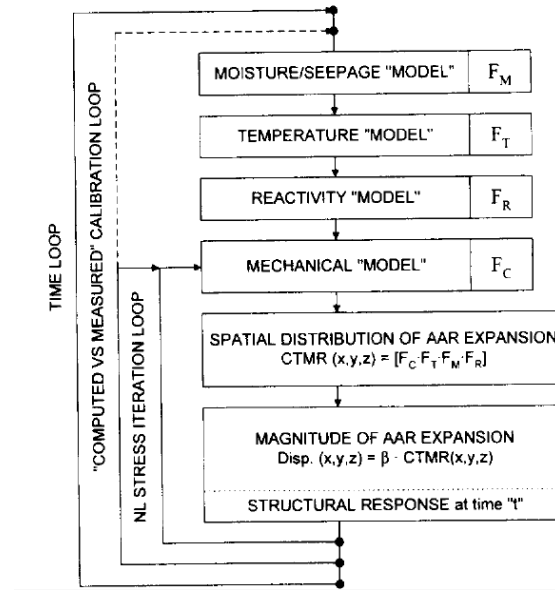


Figure 2.10 – CTMR-ASR simulation model (adapted from Leger et al., 1996)

The induced strain due to ASR, in a particular zone ‘m’ of n finite elements, is written as:

$$\varepsilon_{aar}^m(t) = \beta^m(t) \cdot [F_C(\sigma, t) \cdot F_T(t) \cdot F_M(t) \cdot F_R(t)]^m \quad (2-10)$$

$$\varepsilon_{aar}^m(t) = \beta^m(t) \cdot CTMR^m \quad (2-11)$$

where F_T , F_M , F_R are the normalized expansion factors for temperature, moisture and reactivity of the constituents, $F_C(\sigma, t) = 1 - K \log_{10} \frac{\sigma_i}{\sigma_L}$ is the normalized confinement expansion factor, $\beta^m(t)$ is a calibration factor and $CTMR^m$, is the normalized ASR induced strain.

The equations of equilibrium are formulated as:

$$[K(t)]\{U(t)\} = \{R(t)\} \quad (2-12)$$

where $[K(t)]$ is the structure stiffness matrix, $\{U(t)\}$ and $\{R(t)\}$ are the displacement and respectively load vectors.

The contribution of the ASR expansion to the load vector is:

$$\{R(t)\} = \sum \{ \beta(t) \}^m \{ R(t) \}^m \quad (2-13)$$

where the summation is done over all the zones in which the structure is subdivided. The contribution of zone ‘m’ is considered to be:

$$\{R(t)\}^m = \beta(t)^m \sum \int [B_i]^t [E_i(t)]^t \{ CTMR^m(t) \} dV \quad (2-14)$$

where $[B_i]$ is the strain displacement transformation matrix for element i , V is the element volume, and the summation is done over all finite elements in zone ‘m’.

The effective material property matrix $E_i(t)$ is expressed as a function of several parameters: Poisson’s ratio, tensile strength, elastic modulus, creep coefficient, ASR strain and total strain. The reduction of tensile strength and elastic modulus is accounted for by assuming a linear decrease. The authors suggest the use of material constants for this matter, determined from literature or laboratory tests.

The structure stiffness matrix is obtained from:

$$[K(t)] = \sum \int [B_i]^T [E_i(t)] [B_i] dV \quad (2-15)$$

Upon determining the displacements, the finite element stresses are computed:

$$\{\sigma(t)\} = [E(t)_i] \cdot ([B_i]\{U(t)\} - \{\varepsilon_{aar}(t)\}) \quad (2-16)$$

This procedure is a widely used method in the analysis of ASR affected dams. The model was implemented in a finite element algorithm and it was used to analyze the state of several dams affected by ASR. Herrador et al. (2009) modified this procedure, combining also creep effects to analyze the core-drilled specimens extracted from the Belesar Dam, identified to suffer from ASR in Lugo, Spain.

2.5.3.2 Chemo-mechanical coupling model – Pietruszczak, 1996

Pietruszczak (1996) proposed a nonlinear continuum theory for the description of mechanical effects of AAR in concrete, considering that the progress of the chemical reaction is coupled with the degradation of the material properties, which is described using the framework of elastoplasticity. Huang and Pietruszczak (1996) focused on implementing the model in the

numerical analysis of concrete structures, developing also a three-dimensional finite element analysis of a part of the Beauharnois power plant (Quebec, Canada), affected by ASR.

The material is assumed to be in the elastic range, with the constitutive relation taking the form:

$$\varepsilon^e = C^e \cdot \sigma + \frac{1}{3} \varepsilon_A \cdot \delta \quad (2-17)$$

where ε^e and σ are the principal strains and stresses, C^e is the elastic compliance matrix, δ is Kronecker's delta, and ε_A is the volumetric expansion due to the formation of alkali-silica gel.

The volumetric expansion due to alkali-silica reaction is described by an evolution law:

$$\dot{\varepsilon}_A = g_1(\delta^T, \sigma) \cdot \dot{g}_2(t) \quad (2-18)$$

where g_1 specifies the constraining effect of hydrostatic pressure and g_2 defines the free expansion for a constant alkali content:

$$g_1(\delta^T, \sigma) = e^{\frac{-A_1 \delta^T \sigma}{f_{co}}} \quad (2-19)$$

$$g_2(t) = \frac{\varepsilon t}{A_2 + t} \quad (2-20)$$

where A_1 and A_2 are material constants.

The material is in the elastic range and, as such, the only degrading parameter is assumed to be Young's modulus:

$$E = E_o \left[1 - (1 - A_3) \frac{g_2}{\varepsilon} \right] \quad (2-21)$$

As $g_2 \rightarrow \varepsilon$ for $t \rightarrow \infty$, it is implied that $E \rightarrow A_3 E_o$, where A_3 is a material constant, and E_o is the initial modulus of elasticity. The conditions at failure are defined in terms of a path-independent criterion formulated by Pietruszczak et al. (1988) as follows:

$$F = \bar{\sigma} - k(\theta) \bar{\sigma}_c = 0 \quad (2-22)$$

where

$$\bar{\sigma}_c = \frac{-a_1 + \sqrt{(a_1^2 + 4a_2(a_3 + I/f_c))}}{2a_2} f_c \quad (2-23)$$

In the above equations $I = -I_1$, $\bar{\sigma} = J_2^{1/2}$, $\theta = \frac{1}{3} \sin^{-1}(3\sqrt{3}J_3/2\bar{\sigma}^3)$, where I_1, J_2, J_3 are the basic invariants of the stress tensor and the stress deviator respectively. The parameters a_1, a_2, a_3 are dimensionless material constants and f_c is the uniaxial compressive strength of concrete.

The yield surface is assumed to be of the form:

$$f = \bar{\sigma} - \beta(\xi)k(\theta)\bar{\sigma}_c = 0 \quad (2-24)$$

$$\xi = (2\dot{e}_{ij}^p \dot{e}_{ij}^p)^{1/2} / \bar{\Phi} \quad (2-25)$$

where $\beta(\xi)$ is defined as the hardening function, \dot{e}_{ij} is the deviatoric strain and $\bar{\Phi}$ is a parameter depending on I and θ .

The degradation function for the uniaxial compressive strength is chosen as:

$$f_c = f_{co} \left[1 - (1 - A_4) \frac{g_2}{\varepsilon} \right] \quad (2-26)$$

The degradation of the uniaxial compressive strength is assumed to be accompanied by a proportional reduction in the uniaxial tensile strength which is ensured by the functional form (2-24).

For $f_c = f_c(t)$, Eqs. (2-23), (2-24), and (2-25) yield:

$$\frac{\partial f}{\partial t} = \frac{\partial f}{\partial \bar{\sigma}_c} \frac{\partial \bar{\sigma}_c}{\partial f_c} \frac{\partial f_c}{\partial g_2} \frac{dg_2}{dt} = -\beta(\xi)k(\theta) \frac{f_{co}A_2(1 - A_4)}{(A_2 + t)^2} \left(\frac{\bar{\sigma}_c}{f_c} - \frac{I}{2a_2\bar{\sigma}_c + a_1f_c} \right) \quad (2-27)$$

Under a stationary stress field, the degradation of the plastic properties is described through the evolution of the failure surface which undergoes a continuous contraction due to ASR. This formulation does not take into account the effects of temperature in the evolution of the governing laws for ASR expansion. Huang and Pietruszczak (1999) extended the model so that it includes the magnitude of the confining stresses, the alkali content in the cement, and the temperature history as well. Both the volumetric expansion and the degradation of mechanical properties are assumed to be affected by the temperature of the concrete mass.

The constitutive relation is rewritten as:

$$\varepsilon = C^e \cdot \sigma + \frac{1}{3} \varepsilon_A \cdot m + \varepsilon_T \quad (2-28)$$

The new latter ε_T term is defined as:

$$\varepsilon_T = \frac{1}{3} \beta_T (T - \bar{T}) m \quad (2-29)$$

In the above equation β_T is a coefficient for thermal expansion, T and \bar{T} are the absolute and the reference temperatures, and m is an operator similar to Kronecker's delta.

The notion of 'thermal activated time t' ' is introduced as being a local property influenced by the temperature history. The evolution law is written in the form:

$$\dot{\varepsilon}_A = g_1(m^T, \sigma) \cdot \dot{g}_3(t') \quad (2-30)$$

$$dt' = g_2(T) dt \quad (2-31)$$

Function g_3 represents the free expansion at a given alkali content while g_1 and g_2 represent the constraining effect of the hydrostatic pressure and the temperature. The functions g_1 and g_3 , based on the experimental data from Hobbs (1988), have the form:

$$g_3(t') = \frac{\varepsilon t'}{A_3 + t'} \quad (2-32)$$

$$g_1(m^T, \sigma) = \exp(A_1 m^T \sigma / f_{co}) \quad (2-33)$$

The function g_2 is cast in a hyperbolic form in order to account for the effect of temperature on the rate of reaction; as such:

$$g_2(T) = \frac{1}{2} \left(1 + \tanh \left(\frac{T - T_0}{A_2} \right) \right) \quad (2-34)$$

The kinetics law, which defines the rate of expansion, has the form:

$$\dot{g}_3 = \frac{\varepsilon (1 - g_3/\varepsilon)^2}{A_3} g_2(T) \quad (2-35)$$

The degradation functions for the modulus of elasticity and for the uniaxial compressive strength are assumed to have the following form:

$$E = E_o[1 - (1 - B_1)\frac{g_3}{\varepsilon}] \quad (2-36)$$

$$f_c = f_{co}[1 - (1 - B_2)\frac{g_3}{\varepsilon}] \quad (2-37)$$

where B_1 and B_2 are material constants.

It can be observed that the material properties depend on both the thermal activation time t' and on the chronological time t . The actual numerical integration, however, is carried out with respect to the chronological time.

2.5.3.3 Chemo-mechanical model - Ulm et al. 2000

Ulm et al. (2000) developed a quantitative analysis of the chemo-mechanical effect of the expansion caused by ASR on dimensional stability of concrete structures. A one-dimensional chemoelastic model is proposed to represent the mesoscopic mechanism of ASR swelling. The alkali-silica gel is assumed to exert pressure on the surrounding concrete, once it has filled the pores and the microcracks of the cementitious matrix. The swelling pressure p_g in the gel is considered to be balanced by the tension σ_μ in the concrete skeleton. Figure 2.11 presents the suggested chemoelastic model under stress-free conditions.

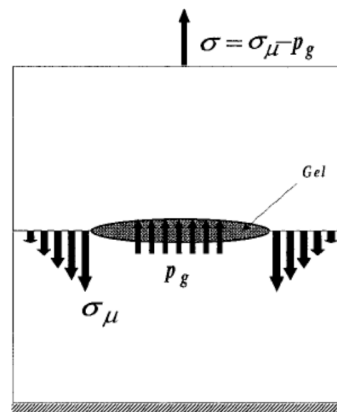


Figure 2.11 – Mesoscopic mechanism of ASR swelling (adapted from Ulm et al., 2000)

For capturing the process at a macro level, the authors suggest a first-order engineering approach assuming an elastic behavior for the concrete. Figure 2.12 presents the parallel chemical pressure spring device, with σ as the stress due to external loading and ε as the overall strain.

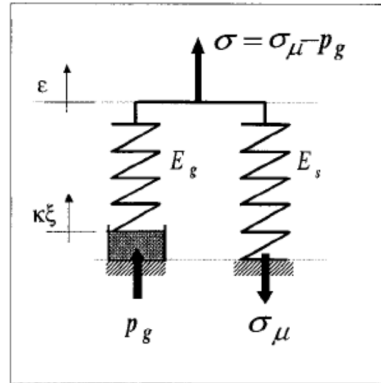


Figure 2.12 – Chemoelastic pressure-spring device for ASR swelling (adapted from Ulm et al., 2000)

One of the springs represents the gel, while the other one represents the concrete matrix; therefore the device takes into account gel expansion and gel compressibility. The stress equilibrium in the chemoelastic device takes the form:

$$\sigma = \sigma_{\mu} - p_g = E_s \varepsilon + E_g (\varepsilon - \kappa \xi) \quad (2-38)$$

where E_s and E_g are the elastic spring moduli of the device, ξ is the reaction extent and κ is intrinsic dilatation coefficient.

In the case of stress-free ASR swelling, the equilibrium equations reads:

$$\sigma = 0: \quad \varepsilon = \beta \xi \quad (2-39)$$

$$\beta = \frac{\kappa E_g}{E_g + E_s} \quad (2-40)$$

The total strain in the case of stress-free ASR swelling is related to the chemical dilatation coefficient β which depends on the intrinsic dilatation coefficient and on the stiffness of the material. As a result, the strain evolution in time is dictated by the non-instantaneous kinetics of the reaction, the only unknown variable being the reaction extent ξ . A linear kinetic law is adopted to relate the reaction affinity $A_m = A_m(\xi)$ to the reaction rate $\dot{\xi} = \frac{d\xi}{dt}$ as follows:

$$\sigma = 0: \quad A_m = k_d \frac{d\xi}{dt} \quad (2-41)$$

where $k_d > 0$ is a coefficient.

The reaction affinity $A_m(\xi)$ defines the reaction order and quantifies the imbalance that triggers the ASR gel formation, decreasing from an initial value $A_m(\xi = 0.0)$ to equilibrium $A_m(\xi = 1.0)$. A first-order reaction is assumed, thus:

$$\sigma = 0: \quad 1 - \xi = t_c \frac{\partial \xi}{\partial t} \quad (2-42)$$

where $t_c = k_d / A_m(\xi = 0)$ is a parameter defining a characteristic time of the reaction, determined from stress-free expansion experimental measurements. The one-dimensional chemoelastic model provides access to the macroscopic kinetics of the reaction from stress-free expansion tests.

The extension to a three-dimensional model is made through an energy balance approach. The expression of dissipation for the considered one-dimensional model has the form: $\varphi dt = \sigma d\varepsilon - d\psi \geq 0$, while the free energy is written as: $\psi = \frac{1}{2}[E_s \varepsilon^2 + E_g(\varepsilon - \kappa\xi)^2] + g(\xi)$. Using the equation of the free energy in the expression on dissipation, it yields:

$$\varphi dt = \left[\sigma - (E_s \varepsilon + E_g(\varepsilon - \kappa\xi)) \right] d\varepsilon + \left[\kappa E_g(\varepsilon - \kappa\xi) - \frac{\partial g}{\partial \xi} \right] d\xi \geq 0 \quad (2-43)$$

From Eqs. (2-40) and (2-43) it follows that:

$$\sigma = \frac{\partial \psi}{\partial \varepsilon} = E_s \varepsilon + E_g(\varepsilon - \kappa\xi) \quad (2-44)$$

The driving force of the reaction is the second term in Eq. (2-43), which may be written in the form:

$$A_m = -\frac{\partial \psi}{\partial \xi} = -\kappa p_g - \frac{\partial g}{\partial \xi} \quad (2-45)$$

The extension to the three-dimensional model is realized by replacing the scalar quantities with their corresponding tensors in the isotropic case.

$$\sigma_{ij} = \frac{\partial \psi}{\partial \varepsilon_{ij}} = \left(K_s - \frac{2}{3}G \right) \varepsilon_{ii} \delta_{ij} + 2G \varepsilon_{ij} + K_g (\varepsilon_{ii} - \kappa \xi) \delta_{ij} = \left(K - \frac{2}{3}G \right) \varepsilon_{ii} \delta_{ij} + 2G \varepsilon_{ij} - 3\beta K \xi \delta_{ij} \quad (2-46)$$

where $K = K_s + K_g = E/3(1 - 2\nu)$ and $G = E/2(1 + \nu)$ are the overall bulk and shear moduli.

The contribution of the swelling pressure $p_g = -K_g(\varepsilon_{ii} - \kappa \xi)$ is neglected and therefore, as in the case of the one-dimensional model, the first-order reaction is considered:

$$\forall \sigma_{ij}: 1 - \xi = t_c(\theta, \xi) \frac{\partial \xi}{\partial t} \quad (2-47)$$

In addition to the standard thermoelastic parameters (E , ν and α), the model has parameters relating to the kinetics of ASR such as the chemical expansion coefficient β , the ASR time constants at reference temperature $\tau_c(T_0)$, $\tau_L(T_0)$ and the thermal activation constants U_c and U_L .

The reaction kinetics suggested by the authors is based on the kinetics proposed by (Larive 1997), being essentially the same as the kinetics proposed by Huang and Pietruszczak (1999). Considering an isothermal stress-free ASR expansion test, carried out at the temperature θ_0 , the volumetric strain ε is recorded as a function of time:

$$\sigma_{ij} = 0: \quad \xi(t) = \frac{\varepsilon(t)}{\varepsilon(\infty)} \quad (2-48)$$

where $\varepsilon(\infty) = 3\beta$ is the volumetric expansion strain.

Eq. (2-48) assumes that the reaction extent can be determined by strain measurements. From Eqs. (2-47) and (2-48) it follows:

$$\sigma_{ij} = 0: \quad \varepsilon(\infty) - \varepsilon(t) = t_c(\theta_0, \xi) \frac{\partial \varepsilon}{\partial t}(t) \quad (2-49)$$

where $\varepsilon(t)$ and $\dot{\varepsilon}(t)$ are measurable functions of time, and the characteristic time t_c can be determined from experimental tests.

The time characteristic is assumed to depend on both the temperature at which the test is carried θ_0 and on the reaction extent, ξ :

$$t_c = \tau_c(\theta_0) \lambda(\xi, \theta_0) \quad (2-50)$$

where

$$\lambda(\xi, \theta) = \frac{1 + e^{-\frac{\tau_L(\theta_0)}{\tau_c(\theta_0)}}}{\xi + e^{-\frac{\tau_L(\theta_0)}{\tau_c(\theta_0)}}} \quad (2-51)$$

Using Eqs. (2-49), (2-50), and (2-51) it follows that:

$$\xi(t) = \frac{1 - e^{-\frac{t}{\tau_c}}}{\xi + e^{-\left(\frac{t}{\tau_c} + \frac{\tau_L}{\tau_c}\right)}} \quad (2-52)$$

Larive's (1997) experiments showed that characteristic time τ_c and the latency time τ_L vary with respect to the temperature according to Arrhenius concept:

$$\tau_c(\theta) = \tau_c(\theta_0) e^{U_c \left(\frac{1}{\theta} - \frac{1}{\theta_0} \right)} \quad (2-53)$$

$$\tau_L(\theta) = \tau_L(\theta_0) e^{U_L \left(\frac{1}{\theta} - \frac{1}{\theta_0} \right)} \quad (2-54)$$

where U_c and U_L are assumed to be activation energy constants of the characteristic and latency time:

$$U_c = 5,400 \pm 500K \quad (2-55)$$

$$U_L = 9,400 \pm 500K \quad (2-56)$$

2.5.3.4 Farage et al., 2004

Farage et al. (2004) proposed a theory based on Ulm et al.'s model (2000), developing a smeared crack finite element approach to analyze ASR effects on concrete structures. Ulm et al.'s one-dimensional model was modified to account for crack opening in tension by adding a cohesive joint element to the spring representing the concrete matrix as represented in Figure 2.13. As in the original model, the gel pressure p_g is balanced by the stresses in the concrete skeleton σ_μ and also by external stresses depending on the loading and boundary conditions, the equilibrium equation being:

$$\sigma = \sigma_{\mu} - p_g \quad (2-57)$$

The gel pressure has the form:

$$p_g = E_g(\varepsilon_{ch} - \varepsilon) \quad (2-58)$$

where ε_{ch} is the ASR-induced strain, ε is the concrete matrix strain and E_g is the gel elastic modulus.

The material total strain is considered to be the superposition of elastic strain and post-cracking strain:

$$\varepsilon = \varepsilon^e + \varepsilon_{cr} \quad (2-59)$$

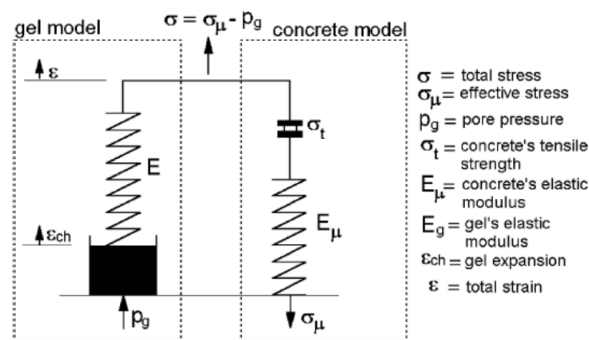


Figure 2.13 – One-dimensional model of expansive concrete behavior (adapted from Farage et al., 2004)

A smeared crack model was adopted and Rankine criterion was selected as a cracking detection surface. Regarding the crack orientation, a fixed orthogonal crack model was considered. The stress-strain relation is presented in Figure 2.14. Depending on the loading condition, the cracks are allowed to close and then reopen, with the model allowing for the release of cracking energy, represented by variations of the modulus of elasticity. Residual strains are neglected.

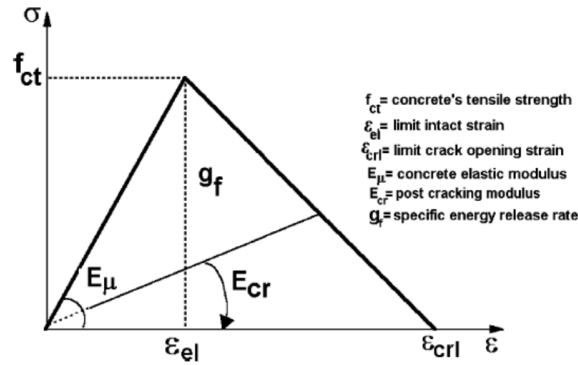


Figure 2.14 – One-dimensional stress-strain relation (adapted from Farage et al., 2004)

The ASR expansion is an input parameter, as proposed by Larive (1997) representing the free expansion evolution of concrete:

$$\dot{\varepsilon}_{ch} = \frac{\varepsilon_{\infty}}{\tau_c} \frac{\left(e^{\frac{T}{\tau_c}} + e^{\frac{-T+\tau_l}{\tau_c}} \right)}{\left(1 + e^{\frac{-T+\tau_l}{\tau_c}} \right)^2} \quad (2-60)$$

where T is the time, ε_{∞} is the asymptotic volumetric strain, τ_l is the latency time and τ_c is the characteristic time.

An isotropic behavior is assumed for concrete under free expansion and therefore the volumetric chemical expansion rate is $\dot{\varepsilon}_{ch}^V = 3\dot{\varepsilon}_{ch}$.

For the three-dimensional model, two reference systems are adopted: a global system (x-y-z) and a local system (1-2-3), coincident with the principal stress directions. System equilibrium is written by replacing the scalars in Equation (2-58) with the corresponding tensors.

The pore pressure is represented by:

$$\mathbf{p}_g = B \begin{bmatrix} 3\varepsilon_{ch} - \varepsilon_v & 0 & 0 \\ 0 & 3\varepsilon_{ch} - \varepsilon_v & 0 \\ 0 & 0 & 3\varepsilon_{ch} - \varepsilon_v \end{bmatrix} \quad (2-61)$$

where B is the gel's bulk modulus:

$$B = \frac{E_g}{3(1 - 2\nu_g)} \quad (2-62)$$

where ν_g is the gel's Poisson's ratio.

The volumetric strain is expressed as:

$$\varepsilon_V = \varepsilon_X + \varepsilon_Y + \varepsilon_Z \quad (2-63)$$

The incremental stress-strain relation is expressed by:

$$\dot{\sigma}_\mu = \mathbf{D} \dot{\varepsilon} \quad (2-64)$$

Prior to cracking, while the principal stresses in direction 1 are lower than the tensile strength, the elastic matrix is represented as:

$$\mathbf{D} = d \begin{bmatrix} 1 & \frac{\nu}{1-\nu} & \frac{\nu}{1-\nu} & 0 & 0 & 0 \\ \frac{\nu}{1-\nu} & 1 & \frac{\nu}{1-\nu} & 0 & 0 & 0 \\ \frac{\nu}{1-\nu} & \frac{\nu}{1-\nu} & 1 & 0 & 0 & 0 \\ 0 & 0 & 0 & \frac{1-2\nu}{2(1-\nu)} & 0 & 0 \\ 0 & 0 & 0 & 0 & \frac{1-2\nu}{2(1-\nu)} & 0 \\ 0 & 0 & 0 & 0 & 0 & \frac{1-2\nu}{2(1-\nu)} \end{bmatrix} \quad (2-65)$$

where ν is concrete Poisson's ratio and $d = \frac{E_\mu(1-\nu)}{(1+\nu)(1-2\nu)}$

The initial elastic matrix is replaced by \mathbf{D}_{cr} post cracking. As the model does not account for shear stresses on the cracked planes, the normal directions to the crack surface are considered uncoupled to the other directions, allowing the formation of a maximum of three cracks per element.

The model was implemented in a software for nonlinear analysis of 3D structures developed in FORTRAN, giving good agreement between the numerical simulations and the experimental

results obtained by Larive (1997). This procedure was developed for massive, lightly reinforced structures, such as dams.

2.5.3.5 Saouma and Perotti, 2006

The Saouma and Perotti (2006) model treats ASR expansion as a volumetric strain that is redistributed among the principal directions according to weight factors empirically determined, largely based on Multon's work (Multon, 2003; Multon et al., 2004). The free ASR volumetric strain, $\varepsilon_{AA\bar{R}}^{vol}$, is calculated as:

$$\varepsilon_{AA\bar{R}}^{vol} = \Gamma_t \cdot \Gamma_c \cdot f(h) \cdot \xi(t, \theta) \cdot \varepsilon_{AA\bar{R}}^{\infty}(\theta_0) \quad (2-66)$$

This model assumes that high compressive or tensile stresses reduce ASR expansion as a result of the formation of micro-cracks or macro-cracks that accommodate the expansive gel. To take this into account, two functions were introduced to reduce the ASR volumetric strain as a function of the stress condition: Γ_t and Γ_c given in Eqs. (2-67) and (2-68). The function $f(h)$ is a reduction function for humidity, usually equal to unity; $\xi(t, \theta)$ in Eq. (2-69) is the expansion evolution, as defined by Larive (1997); and $\varepsilon_{AA\bar{R}}^{\infty}(\theta_0)$ is the laboratory-determined or predicted maximum free expansion at the reference temperature, θ_0 .

$$\Gamma_c = \begin{cases} 1.0 & , \quad \bar{\sigma} \leq 0 \\ 1 - \frac{e^{\beta} \bar{\sigma}}{1 + (e^{\beta} - 1)\bar{\sigma}} & , \quad \bar{\sigma} > 0 \end{cases} \quad (2-67)$$

where $\bar{\sigma} = \frac{\sigma_1 + \sigma_2 + \sigma_3}{3f_c}$ and β is a coefficient equal to 0.5.

The function Γ_t is provided for a smeared crack model:

$$\Gamma_t = \begin{cases} 1.0 & , \quad COD_{max} \leq \gamma_t w_c \\ \Gamma_r + (1 - \Gamma_r) \frac{\gamma_t w_c}{COD_{max}} & , \quad \gamma_t w_c < COD_{max} \end{cases} \quad (2-68)$$

where γ_t is the fraction of the tensile strength beyond which gel is absorbed by the crack, Γ_r is a residual ASR retention factor, COD_{max} is the maximum crack opening displacement at the current Gauss point, and w_c is the maximum crack opening displacement in the tensile softening curve.

The expansion evolution law is:

$$\xi(t, \theta) = \frac{1 - e^{-\frac{t}{\tau_c(\theta)}}}{\xi + e^{-\left(\frac{t}{\tau_c(\theta)} + \frac{\tau_L(\theta)}{\tau_c(\theta)}\right)}} \quad (2-69)$$

Larive's (1997) experiments showed that the characteristic time τ_c and the latency time τ_L vary with respect to the temperature according to the Arrhenius concept:

$$\tau_c(\theta) = \tau_c(\theta_0) e^{U_c \left(\frac{1}{\theta} - \frac{1}{\theta_0}\right)} \quad (2-70)$$

$$\tau_c(\theta) = f(I_\sigma) \tau_L(\theta_0) e^{U_L \left(\frac{1}{\theta} - \frac{1}{\theta_0}\right)} \quad (2-71)$$

where U_c and U_L are assumed to be activation energy constants of the characteristic and latency times, respectively, and $f(I_\sigma)$ is a function that couples the kinetic parameter τ_L to the stress condition:

$$U_c = 5,400 \pm 500K \quad (2-72)$$

$$U_L = 9,400 \pm 500K \quad (2-73)$$

$$f(I_\sigma) = \begin{cases} 1, & I_\sigma > 0 \\ 1 + \alpha \frac{I_\sigma}{3f'_c}, & I_\sigma \leq 0 \end{cases} \quad (2-74)$$

$$I_\sigma = \sigma_1 + \sigma_2 + \sigma_3 \quad (2-75)$$

Therefore, provided that experimental data are available, the user may input the set of parameters needed to describe the kinetics of the reaction: $\varepsilon_{AAR}^\infty(\theta_0)$, $\tau_c(\theta_0)$, $\tau_L(\theta_0)$ and the program will evaluate the expansion based on the evolution law presented above.

The redistribution of the ASR volumetric strain is performed according to weight factors determined based on different scenarios for the applied stress, tensile and compressive strengths as well as σ_{max} , the compression stress above which concrete strain due to ASR is zero.

2.5.3.6 Sellier et al., 2009

The Sellier et al. (2009) model treats ASR expansion as a consequence of the gel pressure, which is calculated according to Eq. (2-76) and depends on temperature, moisture, and maximum volume

of gel that can result from the reactive aggregates. The ASR-induced strains are determined based on an orthotropic damage law (2-77) which links the free expansion with the constrained strains in the principal directions.

$$P_g = K_g \cdot (AV_g - (A_0V_g + b_g tr\varepsilon)) \quad (2-76)$$

where:

K_g : ASR gel bulk modulus

A : chemical advancement

V_g : maximum gel volume fraction that can be created by the ASR

A_0V_g : the gel volume necessary to fill the porosity connected to the reactive aggregates

b_g : coefficient that allows a decrease of gel pressure according to the volumetric expansion $tr\varepsilon$.

$$d_i = 1 - \exp\left(\frac{-1}{m_t} \cdot \left(\frac{\max(\min(f_{ci} + b_g P_g, b_g P_g), 0)}{\sigma_{ut}}\right)^{m_t}\right) \quad (2-77)$$

where:

f_{ci} : the stress in direction i ,

$m_t = 1.32$: damage model parameter

$\sigma_{ut} = 6.4MPa$: damage model parameter.

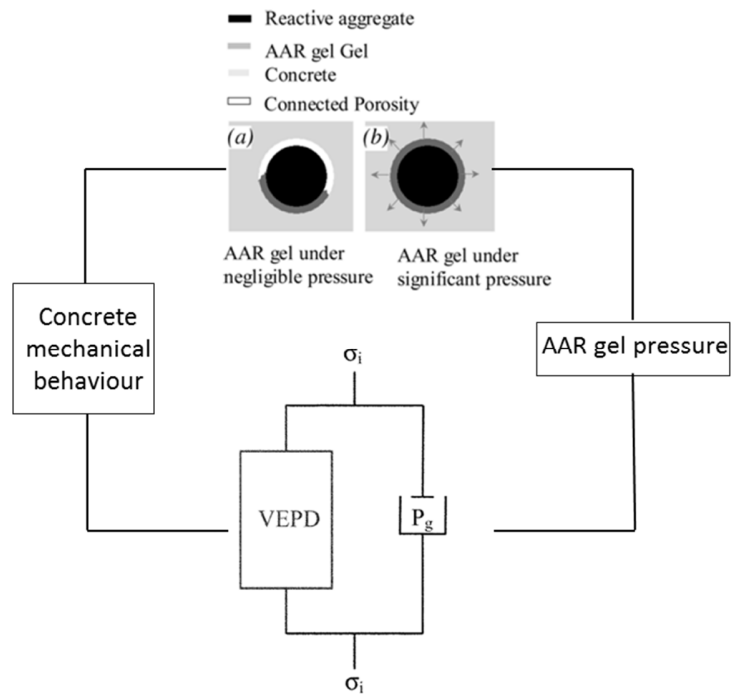


Figure 2.15 – One-dimensional idealized concrete expansion model: P_g is the gel pressure and VEPD is the visco-elasto-plastic and damaged concrete behaviour law symbol (adapted from Grimal et al., 2008)

Chapter 3 VecTor Methodology

3 VecTor Methodology

3.1 Introduction

VecTor2 is a two-dimensional finite element program, developed at University of Toronto, for the analysis of reinforced concrete membrane structures under static and dynamic loading. The Modified Compression Field Theory (MCFT) and the Disturbed Stress Field Model (DSFM), analytical models for cracked reinforced concrete elements subjected to in-plane normal and shear stresses, form the basis for VecTor2. The program has been enhanced to take into consideration the effects of lateral expansion, triaxial stresses, cyclic loading, construction and loading chronology, and bond-slip among other mechanisms.

The MCFT (Vecchio and Collins, 1986) treats concrete as an orthotropic material with rotating uniformly distributed cracks over the element. Compatibility, equilibrium, and constitutive response relationships, formulated in terms of average stresses and average strains, are incorporated in the analysis. An essential feature of the MCFT is the consideration of local stresses and strains at the crack, together with the width and orientation of the cracks. Thus, the failure mechanism may be determined.

The DSFM (Vecchio, 2000) extends the MCFT, enabling improved accuracy in predicting the behaviour for specific types of structures and loading conditions. For elements that exhibit significant shear slip, such as lightly reinforced elements, where the rotation of the principal stress field was found to lag the greater rotation of the principal strain field, the MCFT may overestimate the shear stiffness and strength. Conversely, the MCFT can underestimate the shear stiffness and strength for elements with limited rotation of the principal stress and strain fields. The DSFM produces improved simulations by incorporating: compatibility relationships which include crack shear slip deformations, decoupling the orientation of the principal stress field from that of the principal strain field, and augmented constitutive relationships for concrete and reinforcement.

3.2 Stiffness Formulation

VecTor2 utilizes an incremental total load, iterative secant stiffness formulation as the solution procedure. The total strains $[\varepsilon]$ at a point in a reinforced concrete continuum represent the summation of: the net concrete stress-induced strains $[\varepsilon_c]$; the elastic concrete strain offsets $[\varepsilon_c^o]$ due to mechanisms such as thermal expansion, prestrains, shrinkage, and lateral expansion; the plastic concrete strain offsets $[\varepsilon_c^p]$ due to cyclic loading or damage effects; and the strains due to shear slip along the crack $[\varepsilon^s]$. Consequently, the compatibility relationship for concrete is:

$$[\varepsilon] = [\varepsilon_c] + [\varepsilon_c^o] + [\varepsilon_c^p] + [\varepsilon^s] \quad (3-1)$$

$$[\varepsilon] = \begin{bmatrix} \varepsilon_x \\ \varepsilon_y \\ \gamma_{xy} \end{bmatrix}; [\varepsilon_c] = \begin{bmatrix} \varepsilon_{cx} \\ \varepsilon_{cy} \\ \gamma_{cxy} \end{bmatrix}; [\varepsilon_c^o] = \begin{bmatrix} \varepsilon_{cx}^o \\ \varepsilon_{cy}^o \\ \gamma_{cxy}^o \end{bmatrix}; [\varepsilon_c^p] = \begin{bmatrix} \varepsilon_{cx}^p \\ \varepsilon_{cy}^p \\ \gamma_{cxy}^p \end{bmatrix}; [\varepsilon^s] = \begin{bmatrix} \varepsilon_x^s \\ \varepsilon_y^s \\ \gamma_{xy}^s \end{bmatrix} \quad (3-2)$$

The VecTor2 algorithms were modified to accommodate the anisotropic expansion due to ASR, which is handled in the same manner as the thermal or shrinkage strains. The ASR-induced strains are evaluated following an iterative procedure in the first load stage and carried through the analysis as elastic strain offsets, in the prestrain vector $[\varepsilon_c^o]$. They are determined with respect to the principal axis, according to one of the ASR constitutive models implemented: $\varepsilon_{c1.ASR}^o$, $\varepsilon_{c2.ASR}^o$, and $\varepsilon_{c3.ASR}^o$. If angle θ defines the orientation of the principal axis, the following relationships are used for transforming the strains to the x, y reference system:

$$\varepsilon_{cx.ASR}^o = \varepsilon_{c1.ASR}^o \frac{(1 + \cos 2\theta)}{2} + \varepsilon_{c2.ASR}^o \frac{(1 - \cos 2\theta)}{2} \quad (3-3)$$

$$\varepsilon_{cy.ASR}^o = \varepsilon_{c1.ASR}^o \frac{(1 - \cos 2\theta)}{2} + \varepsilon_{c2.ASR}^o \frac{(1 + \cos 2\theta)}{2} \quad (3-4)$$

$$\gamma_{cxy.ASR}^o = \varepsilon_{c1.ASR}^o \sin 2\theta - \varepsilon_{c2.ASR}^o \sin 2\theta \quad (3-5)$$

Thus, the prestrain vector for ASR is:

$$[\varepsilon_{c.ASR}^o] = \begin{bmatrix} \varepsilon_{cx.ASR}^o \\ \varepsilon_{cy.ASR}^o \\ \gamma_{cxy.ASR}^o \end{bmatrix} \quad (3-6)$$

The total prestrain vector, $[\varepsilon_c^o]$ is constructed through the summation of the thermal, shrinkage, post-cracking dilatation, and ASR-induced strains.

The strain in the i^{th} smeared reinforcement component $[\varepsilon_s]_i$ is comprised of the total strain, elastic offset strain $[\varepsilon_s^o]_i$ due to thermal or prestrain effects, and plastic offset strain $[\varepsilon_s^p]_i$ due to cyclic loading or material nonlinearity, as follows:

$$[\varepsilon_s]_i = [\varepsilon] + [\varepsilon_s^o]_i + [\varepsilon_s^p]_i \quad (3-7)$$

The total strains are related to the element stresses $[\sigma]$ by the composite material stiffness matrix $[D]$, as such:

$$[\sigma] = [D][\varepsilon] - [\sigma^o] \quad (3-8)$$

The material stiffness matrix is determined by combining the contributions from the concrete and reinforcement components, in the context of the secant-stiffness formulation. Stiffness matrices for concrete $[D_c]'$ and for reinforcement components $[D_s]_i'$ are defined with respect to the principal axis, then transformed to the global reference system using appropriate transformation matrices, and summed to form the material stiffness matrix:

$$[D] = [D_c] + \sum_{i=1}^n [D_s]_i \quad (3-9)$$

The pseudo-stress vector $[\sigma^o]$ is used to subtract the stress contribution of strain offsets and shear slip strains, such that the element stresses are related only to the net strains of concrete and reinforcement:

$$[\sigma^o] = [D_c]\{[\varepsilon_c^o] + [\varepsilon_c^p] + [\varepsilon^s]\} + \sum_{i=1}^n [D_s]_i \{[\varepsilon_s^o]_i + [\varepsilon_s^p]_i\} \quad (3-10)$$

The concrete material stiffness matrix $[D_c]'$ is defined relative to the principal axis (1, 2) for two-dimensional elements, according to the MCFT and DSFM formulations:

$$[D_c]' = \begin{bmatrix} \bar{E}_{c1} & 0 & 0 \\ 0 & \bar{E}_{c2} & 0 \\ 0 & 0 & \bar{G}_c \end{bmatrix} \quad (3-11)$$

The secant moduli \bar{E}_{c1} , \bar{E}_{c2} , and \bar{G}_c are evaluated from the current values of the principal stresses, f_{c1} and f_{c2} , and corresponding principal net strains, ε_{c1} and ε_{c2} , as follows:

$$\bar{E}_{c1} = \frac{f_{c1}}{\varepsilon_{c1}}; \bar{E}_{c2} = \frac{f_{c2}}{\varepsilon_{c2}}; \bar{G}_c = \frac{\bar{E}_{c1} \cdot \bar{E}_{c2}}{\bar{E}_{c1} + \bar{E}_{c2}} \quad (3-12)$$

Similarly, the material stiffness matrices for the reinforcement components $[D_s]_i'$ are expressed relative to their longitudinal axes, assuming reinforcement resists only uniaxial stresses:

$$[D_s]_i' = \begin{bmatrix} \rho_i \bar{E}_{si} & 0 & 0 \\ 0 & 0 & 0 \\ 0 & 0 & 0 \end{bmatrix} \quad (3-13)$$

where ρ_i is the reinforcement ratio of the i^{th} reinforcement component. The secant modulus \bar{E}_{si} is defined in terms of the current values of the average strains ε_{si} and stresses f_{si} :

$$\bar{E}_{si} = \frac{f_{si}}{\varepsilon_{si}} \quad (3-14)$$

The material stiffness matrices are transformed to the x, y system of axes by means of the transformation matrix:

$$[D_c] = [T_c]^T [D_c]' [T_c] \quad (3-15)$$

$$[D_s]_i = [T_s]_i^T [D_s]_i' [T_s]_i \quad (3-16)$$

$$[T] = \begin{bmatrix} \cos^2 \psi & \sin^2 \psi & \cos \psi \cdot \sin \psi \\ \sin^2 \psi & \cos^2 \psi & -\cos \psi \cdot \sin \psi \\ -2 \cos \psi \cdot \sin \psi & 2 \cos \psi \cdot \sin \psi & (\cos^2 \psi - \sin^2 \psi) \end{bmatrix} \quad (3-17)$$

where $[T_c]$ is calculated using $\psi = \theta_\sigma$, the inclination of the principal tensile stress axis, with respect to the positive x-axis, and $[T_s]_i$ is evaluated with $\psi = \alpha_i$ the orientation of each reinforcement component, with respect to the positive x-axis. The coordinate reference system is shown in Figure 3.1.

The element stiffness matrix $[k]$, relating the nodal forces to the nodal displacements of the element, is determined based on the composite material stiffness matrix:

$$[k] = \int_{vol} [B]^T [D] [B] dV \quad (3-18)$$

where $[B]$ is the strain-displacement matrix with the form depending on the element type, which in VecTor2 may be triangular, rectangular or quadrilateral.

VecTor2 has been augmented to model the triaxial stress state, which is used to determine the strength enhancement due to confinement. The out-of-plane stresses in the z-direction result from

the confinement effect of lateral expansion provided by the out-of-plane reinforcement (Wong et al. 2013). The out-of-plane concrete strain is computed as:

$$\varepsilon_{cz} = \frac{E_c}{E_c + \rho_z E_{sz}} \left(-\nu_{12} \frac{f_{c2}}{\bar{E}_{c2}} - \nu_{21} \frac{f_{c1}}{\bar{E}_{c1}} + \varepsilon_{cz,ASR}^o \right) \quad (3-19)$$

where ρ_z is the reinforcement ratio in z-direction; E_{sz} is Young's modulus of elasticity for the reinforcement; E_c is the initial tangent stiffness of concrete; \bar{E}_{c1} and \bar{E}_{c2} are the secant moduli of concrete in the principal directions; f_{c1} and f_{c2} are the concrete stresses in the principal directions; ν_{12} and ν_{21} are Poisson's ratios of concrete in the principal directions; and $\varepsilon_{cz,ASR}^o$ is the ASR strain in the out-of-plane direction.

If the out-of-plane reinforcement has yielded the out-of-plane stress is calculated as follows:

$$\varepsilon_{cz} = -\frac{\rho_z f_{z,yield}}{E_c} - \nu_{12} \frac{f_{c2}}{\bar{E}_{c2}} - \nu_{21} \frac{f_{c1}}{\bar{E}_{c1}} + \varepsilon_{cz,ASR}^o \quad (3-20)$$

where $f_{z,yield}$ is the yield strength of the out-of-plane reinforcement.

The stress in the out-of-plane reinforcement is determined as:

$$f_{sz} = E_{sz} \varepsilon_{cz} \leq f_{z,yield} \quad (3-21)$$

From equilibrium, the compressive stress in concrete is:

$$f_{cz} = -\rho_z f_{sz} \quad (3-22)$$

Additional details on VecTor2 methodology may be found in "VecTor2 and FormWorks User's Manual" (Wong et al., 2013). A similar approach can be taken to expand the analysis methodology to three-dimensional elements.

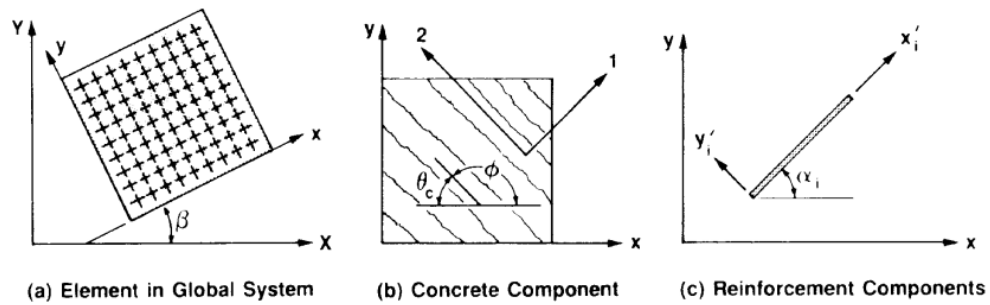


Figure 3.1 – VecTor2 coordinate reference systems (adapted from Vecchio, 1990)

VecTor3 is the three-dimensional version of VecTor2, suited for the analysis of three-dimensional reinforced concrete structures. It was originally developed by Selby (1990) and later extensively

enhanced by ElMohandes (2013). The VecTor3 algorithms were similarly modified to accommodate the anisotropic expansion due to ASR.

3.3 Modelling the Effects of ASR in VecTor2 and VecTor3

In order to quantify the effects of ASR on reinforced concrete structures, two distinct mechanisms are currently considered in the VecTor programs: ASR-induced expansion, and resulting changes in mechanical properties.

3.3.1 Implemented Models for ASR-Induced Expansion

The expansion is treated as an offset strain, evaluated in the first load stage of the analysis according to a procedure previously developed for elastic and plastic offset strains (Vecchio, 1992). Currently, there are six different models embodied in VecTor2 and VecTor3 for the evaluation of ASR-induced expansion:

1. Uniform strains in all directions,
2. Charlwood et al. (1992) model,
3. Curtis (personal communication 2014) model,
4. Saouma and Perotti (2006) model,
5. Sellier (2009) model,
6. Gautam (2015) model.

The first model treats ASR strains as non-recoverable offset strains, uniform in all directions, similar to the procedure for evaluating shrinkage strains. This approach does not take into account the effect of compressive stresses to reduce expansion and it yields the highest expansion of all the models.

The second model implemented was developed by Charlwood et al. (1992) and later refined by Leger et al. (1996), described in detail in the previous chapter. In this case, ASR expansion is evaluated as a strain limited by the effect of confinement, independently evaluated in each principal direction as shown in Figure 3.2.

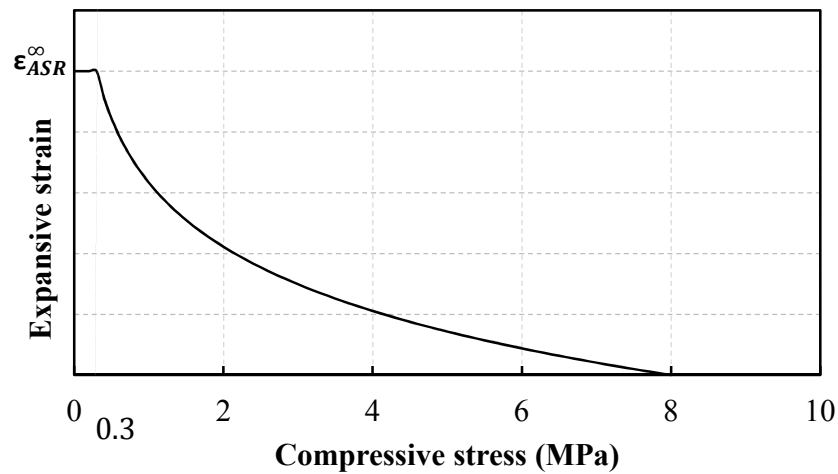


Figure 3.2 – ASR strains in terms of the compressive stress for Charlwood et al. (1992) model

The Curtis (personal communication, 2014) model, a refined version of the Charlwood et al. (1992) model, considers an increase in the concrete growth rate due to tensile stresses, as shown in Figure 3.3. The increase of expansion in tension was defined as a result of field observations of the Mactaquac powerhouse. The analyses performed by Curtis predicted cracking of the water passage piers as a consequence of slot cutting between units; field investigations however, revealed no presence of cracks. As a result, it was concluded that the ASR-induced expansion was increased by tensile stresses near the bottom of intake piers. The revised model was successfully used in the calibration of the Mactaquac powerhouse model, improving the results. The model was developed within a linear-elastic formulation, thus explaining the high tension stresses.

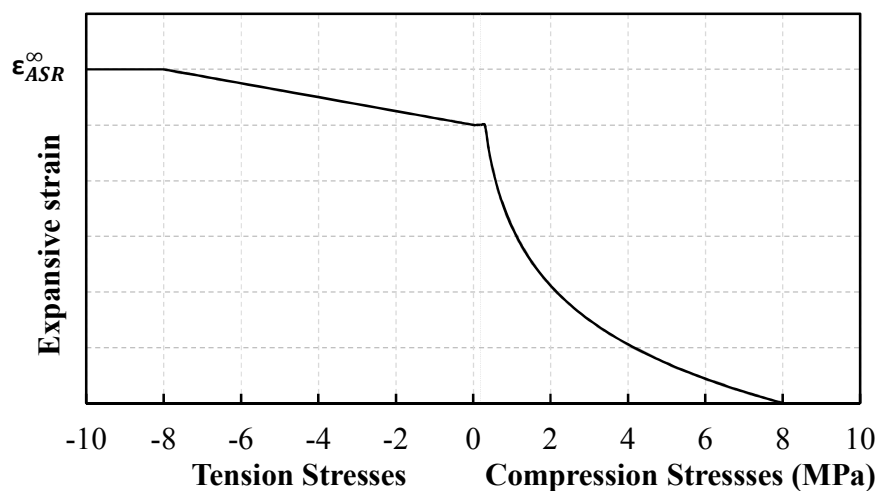


Figure 3.3 – ASR strains in terms of the stress level for Curtis model

The Saouma and Perotti (2006) model treats ASR expansion as a volumetric strain that is redistributed among the principal directions according to weight factors empirically determined, largely based on Multon's work (Multon, 2003; Multon et al., 2004). This model incorporates a kinetics component; as such, predictions of the level of expansion as a function of time may be made, provided that parameters describing the reaction are available from laboratory tests. The model was described in detail in the previous chapter.

The Sellier et al. (2009) model also incorporates a kinetics component. As described in the previous chapter, the ASR expansion is evaluated as a consequence of the gel pressure. The Sellier model, significantly different from all other models implemented in the VecTor programs, predicted results in good agreement with the experimentally observed behaviours and similar to those obtained by the Saouma and Perotti model.

VecTor2 and VecTor3 also embody the ASR constitutive model developed by Bishnu Gautam, under the supervision of Dr. Daman Panesar, as part of the research study funded by the CNSC at the University of Toronto. Concrete cube specimens were subjected to uniaxial, biaxial, and triaxial stresses. Expansion measurements were taken in all three directions as ASR developed in accelerated curing conditions (Gautam et al., 2015). Relationships between the stress state and ASR-induced expansion were derived and implemented in the VecTor programs. A detailed description of the model will be made in the upcoming doctoral thesis of Gautam.

3.3.2 Implemented Models for Mechanical Properties

Experimental data show that ASR causes deterioration of the compressive and tensile strengths, as well as a reduction in the modulus of elasticity. The changes in mechanical properties are closely linked to the type of reactive aggregates present, to the environmental conditions, and to the stress state. Therefore, a formulation that would cover all the possible scenarios is unlikely. As such, the changes in mechanical properties due to ASR effects are calculated following the prescriptions of ISE (1992), as a function of the current free expansion, using lower bound values from tests performed on cubes, prisms and cylinders, and on cores extracted from structures. Lower bounds to the compressive and tensile strengths and modulus of elasticity, as percentages of the targeted properties of unaffected concrete at 28 days, were implemented in the VecTor programs as indicated in Table 3.1 and Figure 3.4.

A significant difference may be observed between the residual compressive strength measured on cube specimens as compared to the cylinder compression strength. This may be due to the fact that the lower bounds for the cylinder values include data obtained from core specimens extracted from structures, which may have experienced an increased damage, or due to the difference in boundary conditions.

Table 3.1 – Lower bound residual mechanical properties as percentage of value for unaffected concrete at 28 days (adapted from ISE, 1992)

Property	Percentage strength as compared with sound concrete for various amounts of free expansion				
	0.5×10^{-3}	1.0×10^{-3}	2.5×10^{-3}	5.0×10^{-3}	10.0×10^{-3}
Cube compression, %	100	85	80	75	70
Cylinder compression, %	95	80	60	60	*
Tension, %	85	75	55	40	*
Elastic modulus, %	100	70	50	35	30

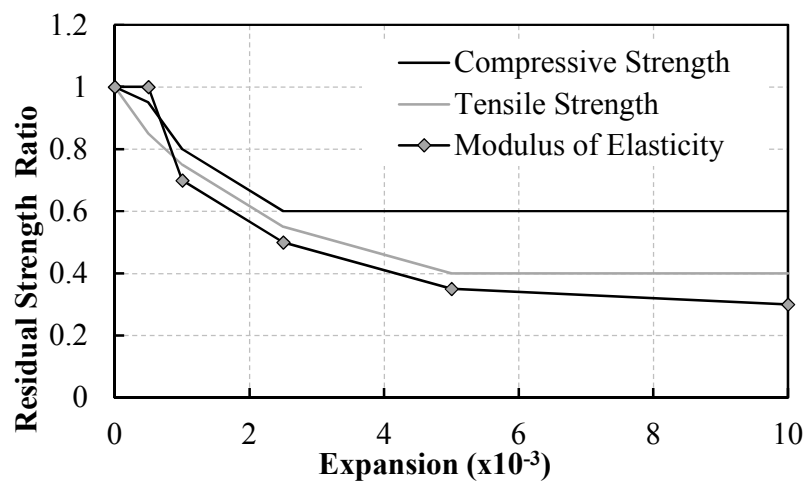


Figure 3.4 – Change in mechanical properties (adapted from ISE, 1992)

3.4 Sample Calculation

In the following section, a sample calculation will be provided on the procedure in which the ASR prestrain vector is determined. For this purpose, a panel with the following material properties was assumed:

$$f'_c = 30.0 \text{ MPa}, \quad f_{cr} = 2.0 \text{ MPa}, \quad \varepsilon_o = -2.0 \times 10^{-3},$$

$$E_c = 25000 \text{ MPa}, \quad \nu = 0.2, \quad E_s = 200000 \text{ MPa},$$

$$\rho_{sx} = 2.0\%, \quad \rho_{sy} = 0.5\%, \quad f_{sy} = 400 \text{ MPa}.$$

where:

- f'_c = compressive strength of concrete cylinder,
- f_{cr} = concrete cracking stress,
- ε_o = strain in concrete at peak stress f'_c ,
- E_c = modulus of elasticity of concrete,
- ν = Poisson's ratio of concrete,
- E_s = modulus of elasticity of reinforcement,
- ρ_{si} = steel reinforcement ratio in i -direction,
- f_{sy} = yielding strength of the reinforcement.

The concrete was considered to be ASR-affected. The degree of ASR strain chosen was 1.5×10^{-3} under stress-free conditions. The Charlwood (1992) model was used as the expansion model, and no reduction of concrete properties was taken into account. An analysis was performed for the stress condition: $\sigma_x = -2.10 \text{ MPa}$, $\sigma_y = 0.00 \text{ MPa}$, $\tau_{xy} = 1.00 \text{ MPa}$ (Eq. (3-23))

$$[\sigma] = \begin{bmatrix} -2.10 \\ 0.00 \\ 1.00 \end{bmatrix} (\text{MPa}) \quad (3-23)$$

The corresponding principal concrete stresses are: $f_{c1} = 0.69 \text{ MPa}$, $f_{c2} = -3.84 \text{ MPa}$, with the orientation angle equal to $\theta = 70.3^\circ$. The out-of-plane stress is $f_{c3} = 0.00 \text{ MPa}$. As such, for the given principal stress condition, the ASR strains determined according to Charlwood (1992) model in the principal directions were: $\varepsilon_{1,ASR} = 1.14 \times 10^{-3}$, $\varepsilon_{2,ASR} = 0.35 \times 10^{-3}$, $\varepsilon_{3,ASR} = 1.50 \times 10^{-3}$.

Using Eqs. (3-4), (3-5) and (3-6) the ASR strains are transformed to the x, y reference system: $\varepsilon_{cx.ASR}^o = 0.36 \times 10^{-3}$, $\varepsilon_{cy.ASR}^o = 1.298 \times 10^{-3}$, and $\gamma_{cxy.ASR}^o = 0.65 \times 10^{-3}$. Thus, the ASR prestrain vector has the form:

$$[\varepsilon_{c.ASR}^o] = \begin{bmatrix} 0.45 \\ 1.04 \\ 0.52 \end{bmatrix} \times 10^{-3} \quad (3-24)$$

The out-of-plane ASR strain is equal to $\varepsilon_{cz.ASR}^o = 1.5 \times 10^{-3}$.

Chapter 4 Verification Studies

4 Verification Studies

The ASR constitutive models implemented in VecTor2 and VecTor3, and the analytical procedure itself, were verified by modelling ASR-affected specimens. The verification studies were carried out at two levels: material behaviour and structural behaviour. In what follows, details of the experimental programs collected from the literature and used in the current study for verification purposes are presented. The numerical techniques used to represent the specimens are described, together with a detailed comparison performed for each element between the analytical and experimental behaviour. This chapter is focused on the VecTor2 verification studies, while the three-dimensional analyses performed with VecTor3 are presented in Chapter 5.

4.1 Behavioural Models and Analysis Parameters

All the analyses performed in this work were modelled with the version of VecTor2 dated May, 2015, and were constructed with VecTor2's pre-processor software, FormWorks 3.8. The post-processor Augustus (Bentz, 2010) was used to process the results.

The structural-level FE studies were carried out with the default models designated in VecTor2, unless there was a valid reason for selecting an alternative behavioural model. The motive of this strategy was to demonstrate that with no subjective use of the advanced constitutive models, reasonable results may be achieved. The default material and behavioural models are presented in Table 4.1.

The following material types were used for the analyses: reinforced concrete with and without smeared reinforcement, ductile steel reinforcement, structural steel, and bearing material. The default properties for the concrete material are shown in Table 4.2. For all the analyses, the cylinder compressive strength, f_c , and initial tangent modulus E_c were specified as input parameters; the remaining properties were left as VecTor2 default values.

The ductile steel reinforcement material has the thermal expansion coefficient, C_s , available with a default value ($10 \times 10^{-6}/^\circ\text{C}$). The following remaining properties must be input by the user: reinforcement ratio (for smeared reinforcement only), reinforcement diameter, yield strength,

ultimate strength, elastic modulus, strain hardening strain, ultimate strain, prestrain, and unsupported length. For some of the specimens analyzed in this study, not all the necessary properties were made available by the researchers who carried out the experimental studies; as such, reasonable assumptions had to be made, mentioned in the following sections. Additional details on VecTor2 may be found in “VecTor2 and FormWorks User’s Manual” (Wong et al. 2013).

Table 4.1 – Constitutive models used for the validation studies

Concrete Models			
Compression Pre-Peak	Hognestad(Parabola)	Dilation	Variable-Kupfer
Compression Post-Peak	Modified Park-Kent	Cracking Criterion	Mohr-Coulomb (Stress)
Compression Softening	Vecchio 1992-A	Crack Stress Calculation	Basic (DSFM/MCFT)
Tension Stiffening	Modified Bentz 2003	Crack Width Check	Agg/2.5 Max Crack Width
Tension Softening	Bilinear	Crack Slip Calculation	Walraven
FRC Tension	SDEM-Monotonic	Creep and Relaxation	Not Considered
Confined Strength	Kupfer / Richart	Hysteretic Response	Nonlinear w/ Plastic offsets
Reinforcement Models			
Hysteretic Response	Bauschinger Effect (Seckin)	Buckling	Akkaya 2012
Dowel Effect	Tassios (Crack Slip)	Concrete Bond	Eligehausen

Table 4.2 – Material properties

Concrete Properties			
Thickness (mm)	required input	C_c ($^{\circ}C$)	10×10^{-6}
f'_c (MPa)	required input	Max. agg. size (mm)	20
f'_t (MPa)	$0.33\sqrt{f'_c}$	Density (kg/m³)	2400
E_c (MPa)	$3320\sqrt{f'_c} + 6900$	K_c (mm²/s)	1.2
ϵ_o (mm/m)	$1.8 + 0.0075 \cdot f'_c$	S_x (mm)	1000
ν_o	0.15	S_y (mm)	1000

Note: The program limits to 1000 mm the spacing of cracks parallel to the y-axis, S_x and parallel to the x-axis, S_y . If the calculated crack spacing is larger than 1000 mm, 1000 mm is used for the crack width evaluation. The crack spacing is calculated based on the CEB-FIP (1978) model.

4.2 Material-Level Investigation

The experimental program carried out by Giaccio et al. (2008) was chosen for the material-level validation study. Giaccio et al. (2008) studied the mechanical behaviour of concrete affected by ASR in comparison with the response of sound concrete. Three different types of reactive concretes were designed with the same mix proportions but with different reactive aggregates as shown in Table 4.3. Cylinders and prisms were cast and stored in saturated conditions at 38°C to enhance ASR development. The evolution of linear expansion, compressive and tensile strengths, and modulus of elasticity were monitored during the experimental program, as were the load-displacement and load-crack opening displacement (CMOD) behaviour in flexure.

Table 4.3 – Mixture proportions (kg/m³)

Concrete	C1	R2	R3	R4
W/C ratio		0.42		
Water		176		
Cement		420		
Na ₂ O equivalent		5.25		
Reactive siliceous orthoquartzite	-	-	120	-
Slow reactive granitic crushed stone	-	-	-	1090
Non-reactive granitic crushed stone	1090	1090	980	-
Natural reactive sand	-	710	-	-
Non-reactive natural sand	710	-	710	710

Expansion measurements were performed on 75 mm x 75 mm x 300 mm prisms. Uniaxial compression tests were performed on 150 mm x 300 mm cylinders. Additional 100 mm x 200 mm cylinders were used to determine the compressive strength and modulus of elasticity at 28 days and their evolution with time. The stress-strain behaviour in tension was studied through three-point bending tests of middle-notched prisms with the dimensions 75 mm x 105 mm x 430 mm. The tests were performed at different ages of the specimens, for different levels of expansion. A major conclusion of this study was that specimens exhibiting the same level of expansion may reach substantially different compressive strengths, as shown in Table 4.4.

Table 4.4 – Concrete properties: 150 mm x 300 mm cylinders

Specimen	Age (days)	f _c (MPa)	E _c (MPa)	Expansion (x10 ⁻³)
C1	250	46.2	39700	-
R2	200	37.3	19900	1.45
R3	120	29.7	18400	1.45
R4	745	49.7	28800	1.35

Since ASR developed in plain concrete, under stress-free conditions, the ASR constitutive model chosen had no influence on the results. As such, for both the compression and tension analyses, no reference is made regarding the ASR model used. A quarter of a cylinder was modelled in VecTor2 as it is shown in Figure 4.1. The cross-sectional area of a 150 mm x 300 mm cylinder was transformed into an equivalent square one of equal area. Thus, the element in VecTor2 had a width of 66 mm, a height of 150 mm and a thickness of 66 mm. Nodal displacement-controlled loads with an increment of 0.01 mm were applied such that the uniaxial behaviour of the specimen would be captured, similar to the test set-up. The cylinder compressive strength and the modulus of elasticity were utilized as the concrete input parameters; the other properties were left as default VecTor2 values. For the reactive cylinders, the initial value of the displacement-controlled loads had to be adjusted according to the level of expansion of each mix.

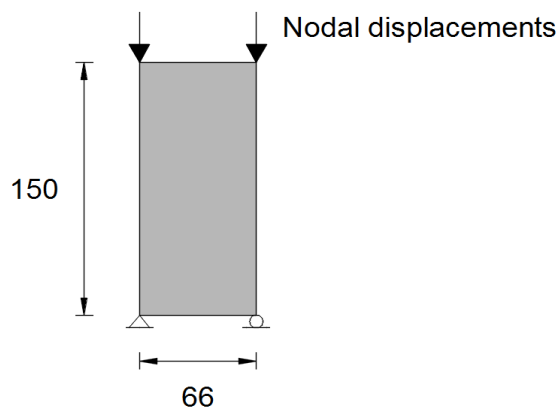


Figure 4.1 – VecTor2 material-level model for a quarter of a cylinder

Figure 4.2 shows the comparison between the stress-strain relationships obtained experimentally and the ones obtained numerically using different models for concrete compression stress-strain response: default VecTor2 concrete model (i.e. Hognestad parabola), Attard and Setunge model, Samani and Attard model, and Popovics HSC model. As shown, the responses of specimens C1, R2, and R3 computed with either the default, Attard and Setunge or Samani and Attard model traced the observed one well. The Popovics HSC model for high strength concrete proved to be more appropriate for the R4 specimen since it had a higher strength, 49.7 MPa.

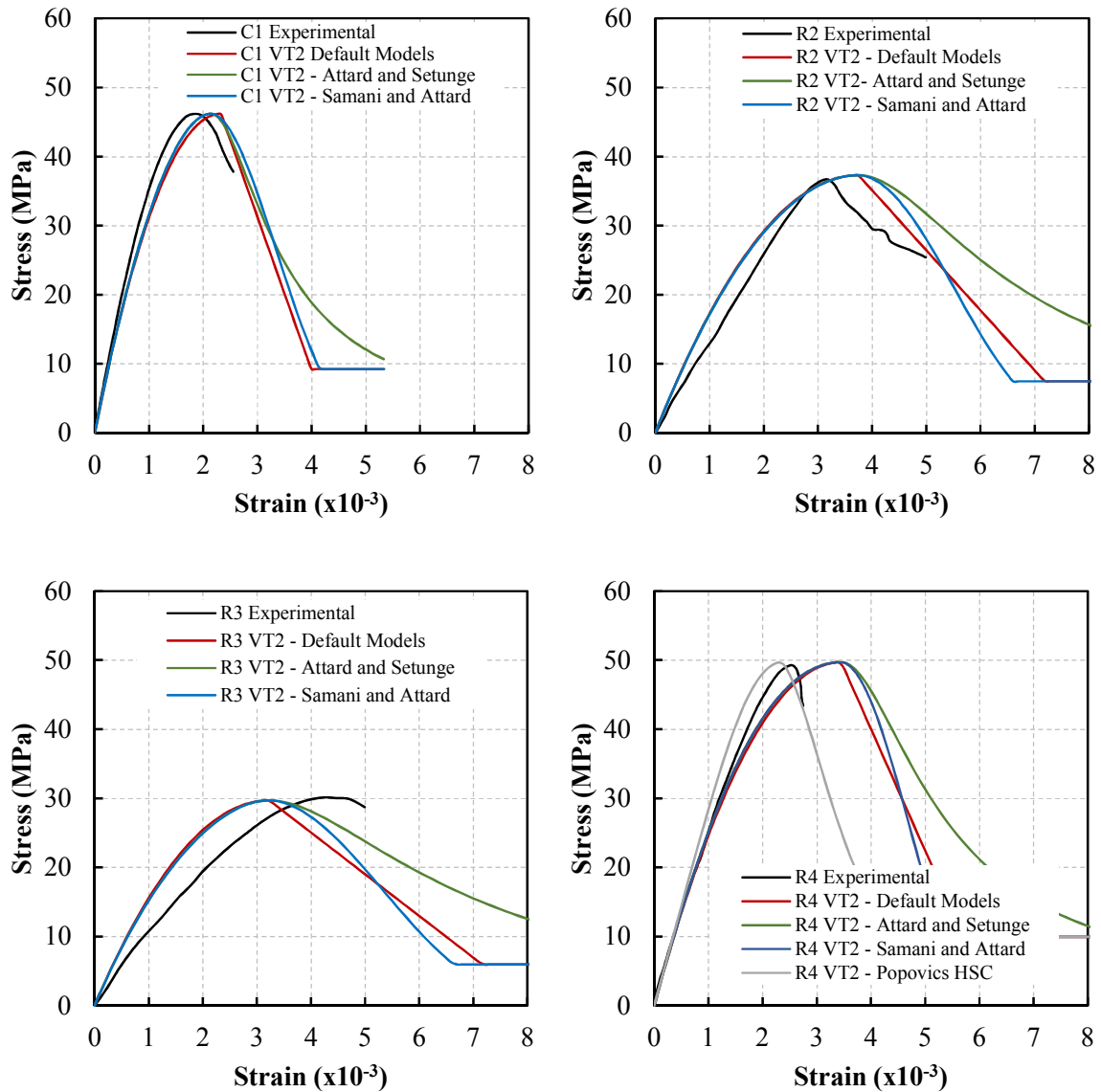


Figure 4.2 – Stress-strain behaviour in compression

Middle-notched prisms, 75 mm x 105 mm x 430 mm, were used to determine the stress-strain behaviour in tension. The prisms were modelled using VecTor2 with a square 5 mm x 5 mm mesh, as shown in Figure 4.3. A total of 1817 rectangular elements were used for representing the prisms, all having the same thickness of 105 mm, as utilized by Giaccio et al. (2008). Displacement-controlled load with 0.01 mm increments was applied at the centre of the simply-supported beam. The material input parameters specified were the concrete compressive strength and modulus of elasticity, as determined from the cylinder tests. The other concrete properties were kept as default

VecTor2 values. For the reactive specimens, the expansion determined on the 75 mm x 75 mm x 300 mm prisms was used to determine the strains caused by ASR. Concrete properties and the ASR expansion are presented in Table 4.5.

Comparisons between the analytical results and the experimentally observed behaviours are shown in Figure 4.4. Two set of analyses were performed for each prism: one assuming that the tensile strength of concrete was $f'_t = 0.33\sqrt{f'_c}$, labelled as VecTor2 A; the other one assuming that the tensile strength was $f_t = 0.6\sqrt{f'_c}$, labelled as VecTor2 B. The former is the typical default value for VecTor2, representing lower bound conditions, while the latter is thought to be a more appropriate average value for this type of test. A good correlation between the theoretical calculated behaviour and the actual determined behaviour can be observed for VecTor2 B.

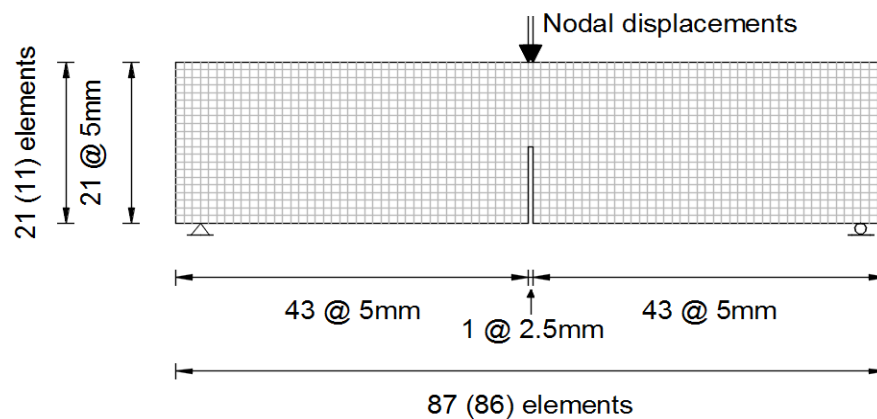


Figure 4.3 – VecTor2 model for middle-notched prism.

Table 4.5 – Concrete properties: 100 mm x 200 mm cylinders

Specimen	Age (days)	f'_c (MPa)	$f'_t = 0.33\sqrt{f'_c}$ (MPa)	$f_t = 0.6\sqrt{f'_c}$ (MPa)	E_c (MPa)	Expansion ($\times 10^{-3}$)
C1-75d	75	39.5	2.07	3.77	38200	-
C1-250d	250	47.4	2.24	4.08	37900	-
C1-745d	745	49.4	2.32	4.22	37400	-
R2-200d	200	37.8	2.03	3.69	17100	1.45
R2-250d	250	29.1	1.78	3.24	13100	1.80
R3-75d	75	30.8	1.83	3.33	25100	1.15
R3-120d	120	32.8	1.89	3.44	21700	1.45
R4-485d	485	51.2	2.36	4.29	31300	1.25
R4-745d	745	48.2	2.29	4.16	30100	1.35

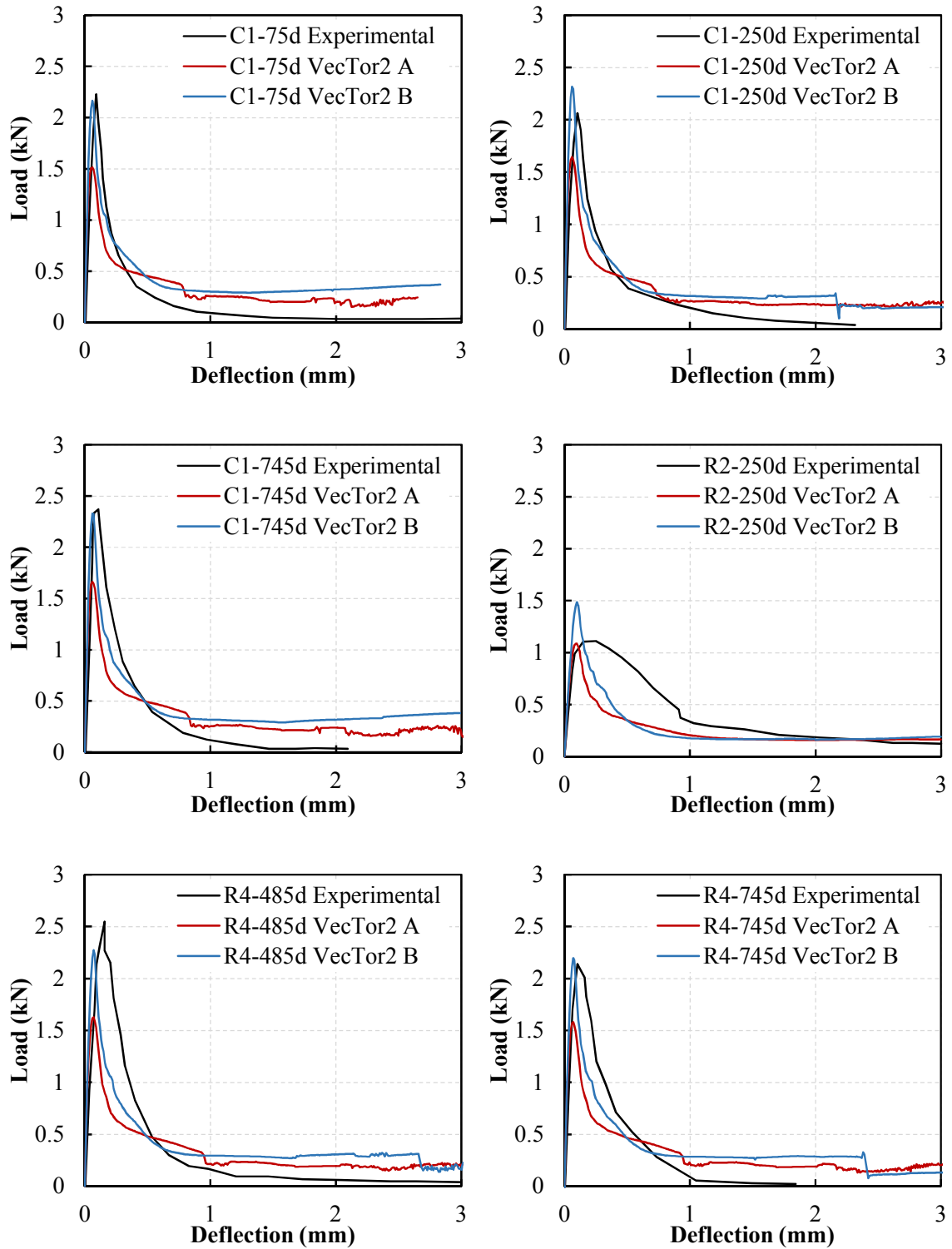


Figure 4.4 – Load-deflection behaviour for Giaccio prisms specimens

Table 4.6 presents the comparison between actual compressive strength and modulus of elasticity of the ASR-affected concrete, as reported by Giaccio et al. (2008), and the ones estimated using the ISE reduction factors, as function of the free expansion and the concrete properties of unaffected concrete at 28 days. It is shown that ISE procedure underestimates the compressive strength, with the ratio of actual to calculated strengths having a mean of 1.79 and a coefficient of variation (COV) of 22%. The modulus of elasticity is estimated somewhat more accurately with a mean of 0.99 and a COV of 28%.

Table 4.6 – Actual vs. ISE estimated concrete mechanical properties

Specimen	Age (days)	Expansion ($\times 10^{-3}$)	Actual		ISE		Actual/ISE	
			f'_c (MPa)	E_c (MPa)	f'_c (MPa)	E_c (MPa)	f'_c	E_c
C1-28d	75	-	28.6	35700	-	-	-	-
R2-200d	200	1.45	37.8	17100	21.2	22848	1.78	0.75
R2-250d	250	1.80	29.1	13100	19.8	21182	1.47	0.62
R3-75d	75	1.15	30.8	25100	22.3	24276	1.37	1.03
R3-120d	120	1.45	32.8	21700	21.2	22848	1.55	0.95
R4-485d	485	1.25	51.2	31300	21.9	23800	2.34	1.32
R4-745d	745	1.35	48.2	30100	21.5	23324	2.24	1.29
Mean							1.79	0.99
COV ¹							22%	28%

¹COV = Coefficient of variation

The material-level FE simulations prove that the program is capable of reproducing the behaviour of ASR-affected concrete subjected to pure compression or tension, as accurate as for sound concrete specimens.

4.3 Structural-Level Investigations

A considerable number of experimental studies have been carried out on ASR-affected structural elements including reinforced concrete beams, prestressed beams, reinforced concrete columns and reinforced concrete slabs. In the following section, the experimental investigations selected for the validation studies performed with VecTor2 are presented, as well as the numerical techniques used for the numerical analyses.

4.3.1 Kobayashi et al., 1988

Ten prestressed concrete beams were constructed and tested to failure at the Department of Civil Engineering at Kyoto University, Japan (Kobayashi et al., 1988). Three different types of concrete mixtures were used: non-reactive concrete (Mix-I), reactive concrete with 6 kg/m³ Na₂O equivalent (Mix-II), and reactive concrete with 8 kg/m³ Na₂O equivalent (Mix-III). For the reactive mixtures, bronzite andesite containing cristobalite and silica glass was used as coarse aggregate. All beams had a rectangular cross section of 100 mm x 200 mm and were 1600 mm long. The beams were post-tensioned after being cured for 28 days at 20° C and 80% RH with 11 mm or 15 mm diameter bars to give a bottom stress of 4.90 MPa or 9.80 MPa and zero top stress. The transverse reinforcement ratio of 0.58% was provided by 6 mm stirrups, supported by four longitudinal 6 mm mild steel reinforcement bars (Figure 4.5).

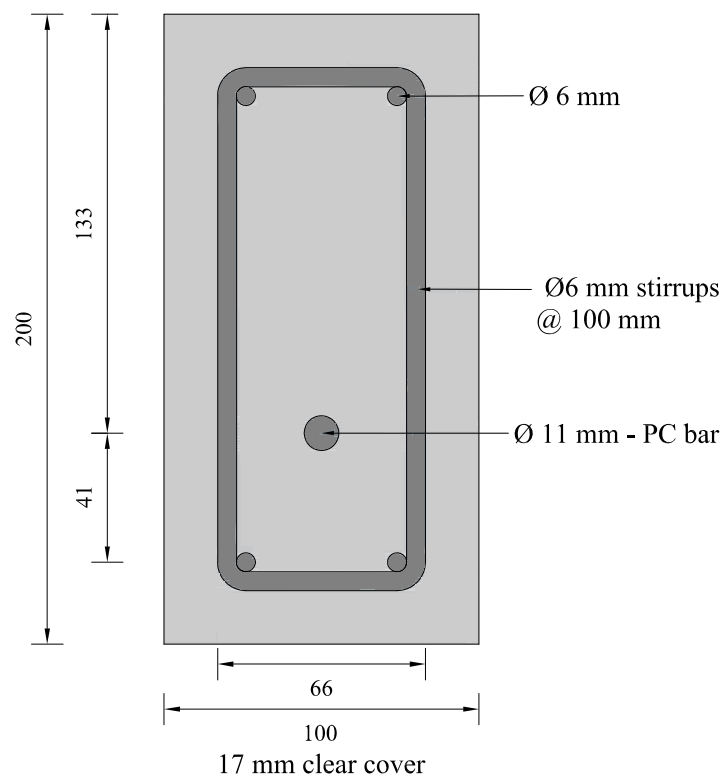


Figure 4.5 – Specimen reinforcement and cross section (adapted from Kobayashi et al., 1988)

After post-tensioning, the beams were stored at 40° C and 100% RH. The changes in steel strains were monitored during the accelerated curing period for the prestressing bar, top and bottom longitudinal reinforcement, as well as for transverse reinforcement. The beams were tested under

symmetrical two-point loading, simply supported with a span length of 1360 mm. The shear span-to-depth ratio (a/d) was alternately set at 4.0 or 2.5. All beams failed in flexure, regardless of the shear span-to-depth ratio, with no significant difference between reactive and non-reactive beams.

The following conclusions were derived from the tests:

1. The compressive strength, tensile strength and modulus of elasticity of Mix-III were reduced by 60%, 50% and 45%, respectively, as compared to Mix-I (normal concrete) whereas Mix-II showed little decrease in its mechanical properties relative to sound concrete at the day of the test.
2. All beams failed in flexure, regardless of the shear span-to-depth ratio, with no significant difference between the reactive and non-reactive beams.
3. The strength of the ASR-affected beams was within 10% of the non-reactive beams, even with stirrups strains greater than 1.0×10^{-3} .
4. The difference in deflections of the beams were reported to be within 10% of each other.

The beams were modelled with VecTor2 following the details of the experimental program. A total of 3232 rectangular elements with the thickness of 100 mm were used for the finite element model. The longitudinal reinforcement was represented with 472 truss bar elements connected directly to the concrete elements. The behaviour of both passive and prestressed reinforcement was assumed to be linear-elastic with strain hardening. The prestrain of the prestressed reinforcement was calculated such that the compressive stress level specified by Kobayashi et al. (1988) at the lower fibre of the cross section would be obtained, 4.9 MPa for the 11 mm reinforcement and 9.8 MPa for the 15 mm reinforcement. The transverse reinforcement was included in the concrete elements as smeared reinforcement.

Displacement-controlled loads (i.e. nodal displacements) were applied symmetrically, consistent with the test set-up. A bearing material with unidirectional stiffness was defined at the contact between the concrete beam and the steel bearing plates. The finite element model for a beam having the shear span-to-depth ratio of 4.0, representative for this experimental study, is presented in Figure 4.6. Details of the test specimens on concrete properties and age at test are presented in Table 4.7.

Shown in Figure 4.7 is the predicted crack pattern for beam specimen II-2, as obtained from the FE analysis, compared with the experimentally observed one. The analysis indicated flexural cracks developing at the mid-span of the beams, and crushing of the concrete at the top of the beam as the failure mechanism, consistent with the test. Similar results were obtained for all the beams.

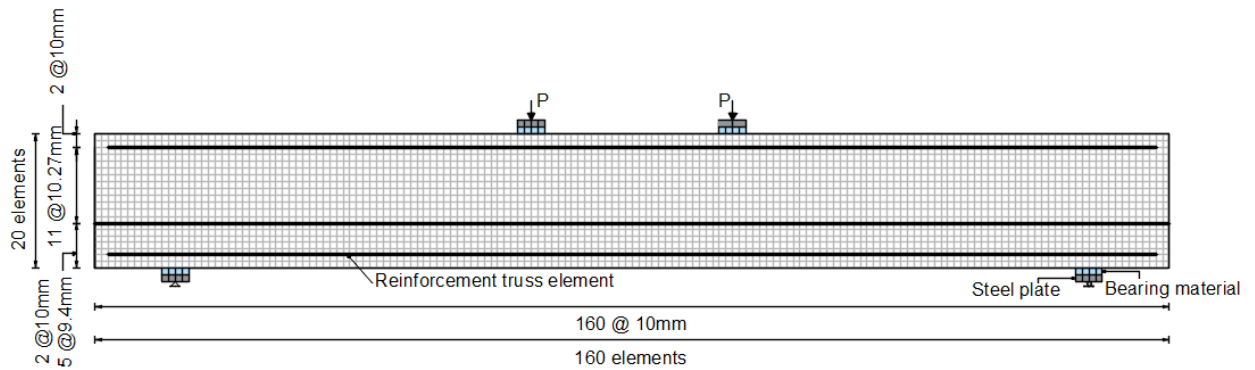


Figure 4.6 – Finite element model for beam specimen I-1

Table 4.7 – Details of test specimens

Specimen	Mix	Age (days)	PC bar ϕ (mm)	Properties at 28 days		Properties at loading test	
				f'_c (MPa)	E_c (MPa)	f'_c (MPa)	E_c (MPa)
I-1	I	284	11	35	26772	50	41202
II-1	II	284	11	34	25987	50	38150
III-1	III	181	11	41	24124	30	17260
I-2	I	284	15	35	26772	50	41202
II-2	II	284	15	34	25987	50	38150
III-2	III	181	15	41	24124	30	17260
I-3	I	405	15	35	26772	55	37363
II-3	II	405	15	34	25987	55	39324
III-3	III	181	15	41	24124	30	17260
III-4	III	181	11	41	24124	30	17260

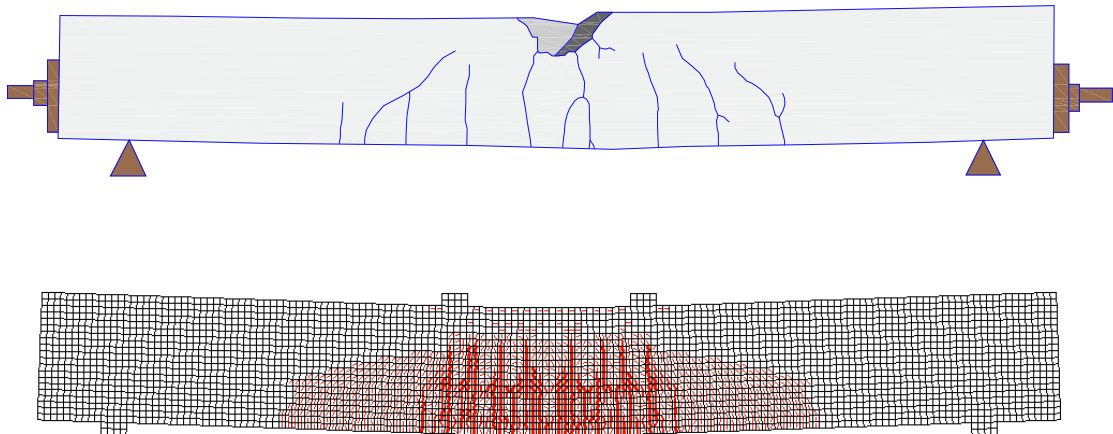


Figure 4.7 – Predicted and experimental crack patterns for beam II-2

The load-deflection relationships for the beams are presented in Figure 4.8 as reported by Kobayashi et al. (1988). Shown in Table 4.8 are the maximum ultimate loads obtained experimentally versus the maximum ultimate loads obtained with VecTor2 for all the beams tested. Two set of analysis were performed with VecTor2 for each beam: one using the actual concrete properties as determined from cylinders before the test, labelled VecTor2 Actual; and another, labelled VecTor2 Factored, using the concrete properties at 28 days modified by the ISE reduction factors due to AAR, in the case of the reactive specimens. It may be observed that the analyses performed with the actual concrete properties yielded results closer to the experimental values in terms of capacity, albeit with a mean of 1.14 and a COV of 7.2%. Nevertheless, the stiffness was better captured when the ISE reduction factors were utilized, with a mean of 1.24% and a COV of 7.9% for the ultimate load. As the failure mechanism of the beams was crushing of concrete, this result is largely consistent with the material-level study performed for the Giaccio et al. (2008) specimens, where it was found that the ISE reduction factors underestimated the compressive strength but predicted the modulus of elasticity better.

Kobayashi et al. (1988) do not provide the free expansion due to ASR for each specimen; instead the strain level in the top and bottom reinforcement, prestressed reinforcement, and stirrups are reported. Thus, the free expansion needed for the ASR expansion models was determined by comparison between the analytical strains with the experimentally measured ones, as shown in Table 4.9.

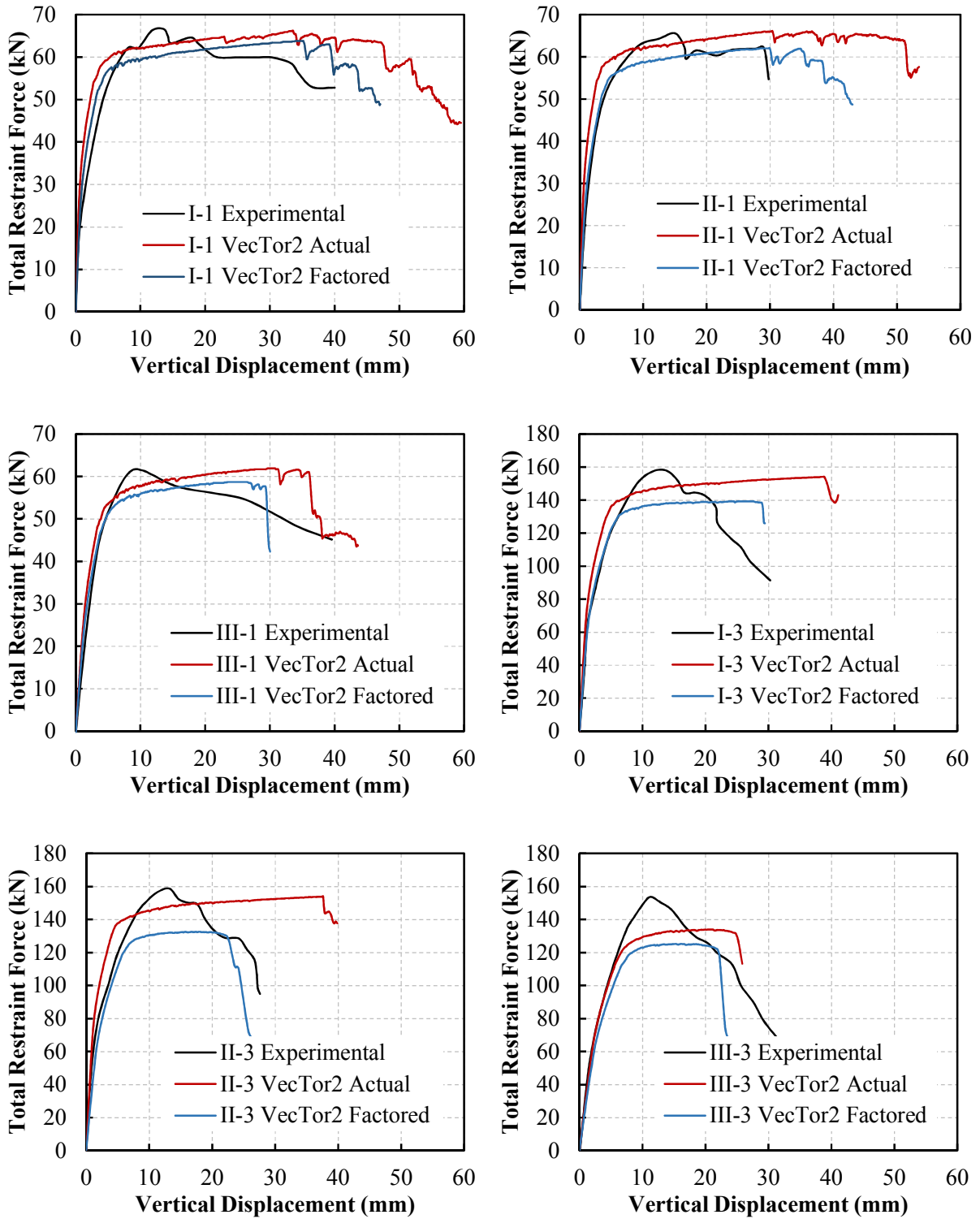


Figure 4.8 – Load-deflection relationships: analytical versus experimental results

Table 4.8 – Experimental versus theoretical maximum ultimate loads

Specimen	$P_{u,test}$ (kN)	$P_{u,calc.}$ (kN)		Test/Calc.	
		Actual ¹	Factored ²	Actual ¹	Factored ²
I-1	73.6	66.2	63.8	1.11	1.15
II-1	72.3	66.1	62.1	1.09	1.16
III-1	68.2	61.9	58.7	1.10	1.16
I-2	100.5	93.9	86.7	1.07	1.16
II-2	104.0	94.0	84.2	1.11	1.23
III-2	88.2	83.5	78.0	1.06	1.13
I-3	176.5	154.1	139.2	1.15	1.27
II-3	181.4	154.0	132.6	1.18	1.37
III-3	170.6	133.9	125.2	1.27	1.36
III-4	129.0	99.3	94.4	1.30	1.37
Mean				1.14	1.24
COV ³				7.2%	7.9%

¹Actual: properties of AAR specimens, as determined from test cylinders

²Factored: properties of normal concrete at 28 days with ISE factors applied

³COV = Coefficient of variation

Table 4.9 – Experimental versus theoretical strains

Specimen	Measured strains				Theoretical strains – actual ¹				Theoretical strains – factored ²				AAR strain
	PC bar	upper	lower	stirrup	PC bar	upper	lower	stirrup	PC bar	upper	lower	stirrup	
I-1	0.04	0.07	-0.18	0.25	-0.01	-0.02	-0.12	0.01	-0.13	-0.02	-0.18	0.01	0.00
II-1	0.10	0.57	-0.02	0.39	0.09	0.35	-0.02	0.55	0.03	0.34	-0.10	0.55	0.70
III-1	0.38	1.10	0.17	1.63	0.39	1.05	0.13	1.45	0.37	1.04	0.09	1.46	3.00
I-2	-0.04	0.25	-0.14	0.37	-0.20	-0.03	-0.27	0.02	-0.28	-0.04	-0.37	0.03	0.00
II-2	0.12	0.38	-0.11	0.47	-0.10	0.22	-0.24	0.57	-0.23	0.21	-0.42	0.57	0.70
III-2	0.14	0.87	-0.10	1.47	-0.10	0.75	-0.45	1.48	-0.19	0.75	-0.57	1.46	3.00
I-3	-0.88	0.36	-0.12	0.58	-0.20	-0.03	-0.27	0.03	-0.28	-0.05	-0.37	0.03	0.00
II-3	-0.07	0.35	-0.10	0.51	-0.07	0.28	-0.25	0.70	-0.23	0.27	-0.44	0.68	0.90
III-3	0.19	0.84	-0.19	1.43	-0.10	0.74	-0.44	1.49	-0.16	0.75	-0.53	1.47	3.00
III-4	0.38	0.92	0.13	1.49	0.40	1.04	0.14	1.45	0.37	1.03	0.10	1.45	3.00

4.3.2 Fan and Hanson, 1998

Six reinforced concrete beams were tested at the Department of Civil Engineering at North Carolina State University, USA, to investigate the effects of ASR expansion on the behavior of reinforced concrete. Three beams were cast with reactive concrete and the other three beams with non-reactive concrete. Gold Hill coarse aggregate from North Carolina was used for the reactive mixture, classified by the North Carolina Department of Transportation as being a highly reactive aggregate. Ordinary Portland cement with an alkali content of 0.65% Na₂O equivalent was used. The compressive strength at 28 days was 34.7 MPa for the reactive mix, and 35.9 MPa for the nonreactive concrete. The beams were 1500 mm long with a cross section of 150 mm x 250 mm (Figure 4.9). Two longitudinal reinforcement ratios were chosen: 0.4% and 1.0% using 2 #3 bars (#3N and #3R) or 2 #5 bars (#5N1, #5R1, #5N2, and #5R2). All bars were Grade 60. The stirrups were D-5 wire placed at 75 mm. Cylinders (100 mm x 200 mm) were also cast to investigate the development of mechanical properties.

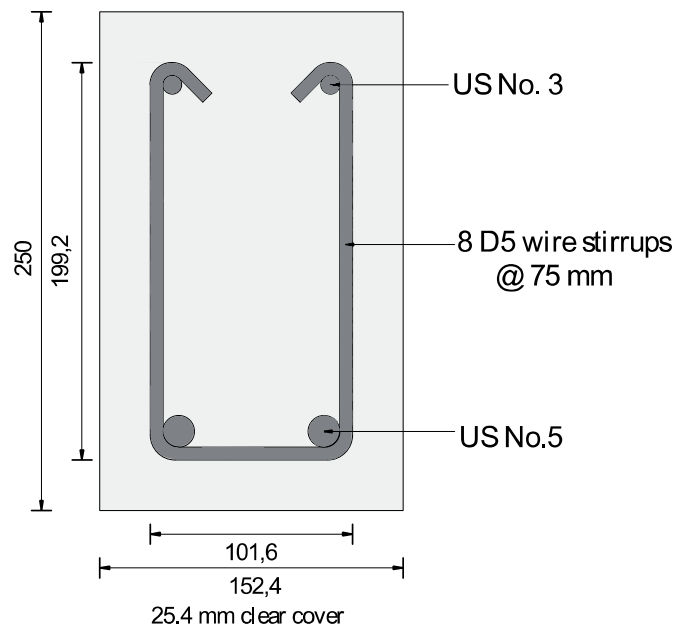


Figure 4.9 – Specimen reinforcement – cross section (adapted from Fan and Hanson, 1998)

After being cured for 14 days in a standard moisture room, all specimens were placed in a 0.5 N concentration alkali solution. The solution was made by adding 10 grams of NaOH, 14 grams of potassium hydroxide KOH, and 0.1 grams of CaO per liter of tap water, as proposed by the British Cement Association (1992). The solution was heated to 38°C for a period of 5 to 7 days, after

which it was allowed to cool at 24°C for 2 days. This procedure continued until the end of the tests. Two of the beams, one reactive and one non-reactive, were loaded during the ASR conditioning period such that cracks of around 0.2 mm developed on the tension face in order to investigate the effect of ASR on beams under service loads.

After one year of accelerated conditioning, the beams were tested to failure. During the curing period the expansion was monitored for all beams at three different locations: longitudinal expansion at top of the beams, longitudinal expansion at the level of the reinforcing bars, and transverse expansion. Figure 4.10 shows the length expansion measurements for beams #3N and #3R. Similar trends of expansion were reported for the other four beams.

The conclusions from this study were consistent with the behavior of ASR-affected beams observed in other experimental programs:

1. Cracking was observed six months after the immersion in the alkali solution.
2. The main cracks were primarily oriented parallel to the longitudinal reinforcement.
3. Substantial changes in the concrete mechanical properties were found after cracking.
4. The flexural capacity of the ASR-affected beams was nearly the same as the capacity of the non-reactive beams.

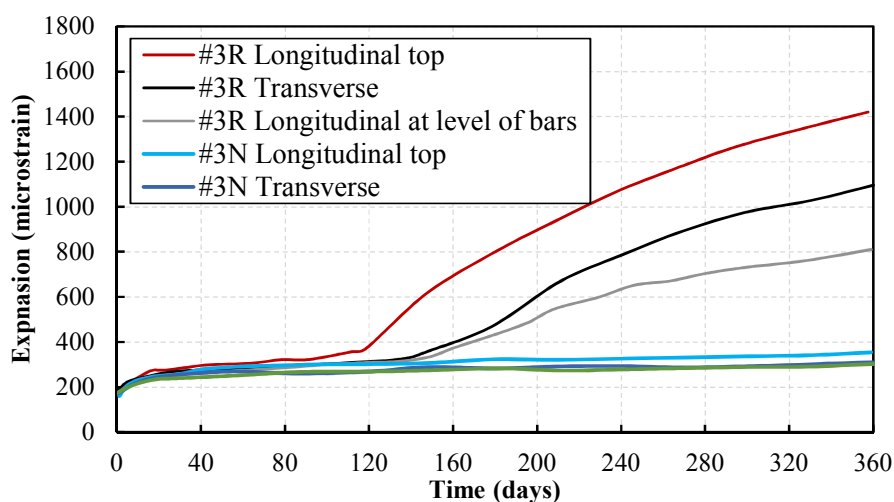


Figure 4.10 – Length expansion of beams #3N and #3R (adapted from Fan and Hanson, 1998)

The beams were modelled with VecTor2. The support and loading condition, together with the reinforcement layout and the mesh, are presented in Figure 4.11. The longitudinal reinforcement was represented as discrete reinforcement, while the stirrups were modelled as smeared. A total of 3766 rectangular elements and 292 truss bar elements were used to model the beam. Monotonically increasing nodal loads with 1 mm increments were applied at the locations indicated in Figure 4.11, similar to the test set-up. A bearing material with unidirectional stiffness was modelled at the interface between the bearing steel plates to better match the support conditions from the test.

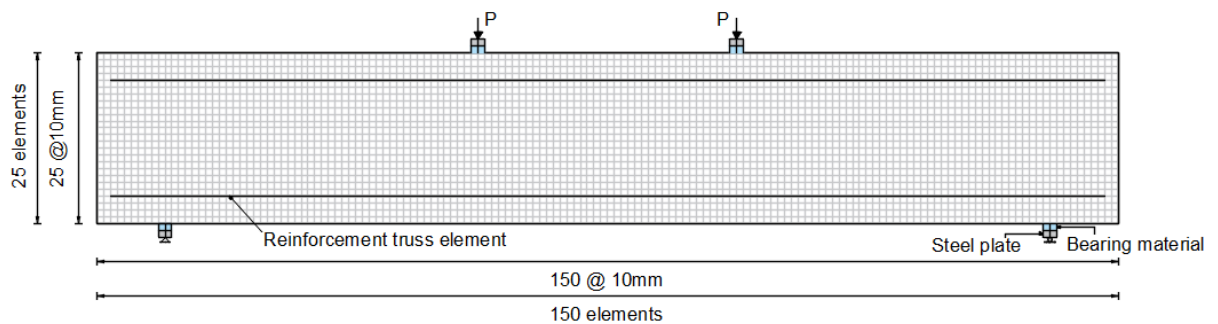


Figure 4.11 – Finite element model for the Fan and Hanson beam specimens

The concrete properties specified in the analyses were the compressive strengths, 35 MPa for the non-reactive specimens and 25 MPa for the reactive ones, and the modulus of elasticity estimated as $3320\sqrt{f'_c} + 6900$ MPa. The other properties were left as default VecTor2 values. For the reinforcement properties, only the yielding strength of the longitudinal bars, 435 MPa, was specified by Fan and Hanson (1998), thus, an elastic-plastic response with strain hardening was assumed as described in Table 4.10. Two analyses were performed for each test, the variables being the reinforcement properties. As the beams are flexural-critical, their behaviour after the yielding of the reinforcement was sensitive to the assumed strain-hardening response of the reinforcement.

Table 4.10 – Reinforcement properties

Label	f_y (MPa)	f_u (MPa)	ϵ_{sh} ($\times 10^{-3}$)	ϵ_u ($\times 10^{-3}$)	E_s (MPa)
$f_u=1.5*f_y$	435	653	3	125	200,000
$f_u=1.7*f_y$	435	783	3	125	200,000

The cracking pattern (Figure 4.12), as well as the stiffness, displacement at ultimate load, and the ultimate capacity were captured reasonably well by VecTor2. The comparison between the analytical and experimental results are presented in Table 4.11 and Figure 4.13. The ultimate loads were estimated relatively well by VecTor2 with a mean of 0.93 and a COV of 3.11% for the analyses performed with $f_u=1.7*f_y$. The second set of analyses, which assumed $f_u=1.5*f_y$, gave somewhat poorer results with a mean of 0.87 and a COV of 3.98%. There was a tendency to overestimate the initial stiffness of the ASR-affected beams, which may be a consequence of the prestressing effect of the reinforcement, the compressive stresses induced in concrete due to ASR expansion, or the estimation of Young's modulus for concrete.

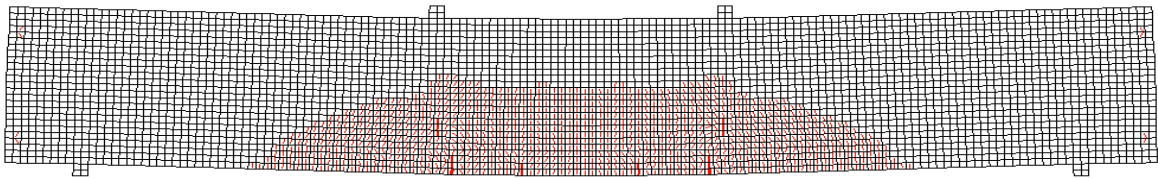


Figure 4.12 – Deflected shape and cracking pattern for #3R beam at 70% of the ultimate capacity

Table 4.11 – Experimental versus theoretical maximum ultimate loads

Specimen	$P_{u,test}$ (kN)	$P_{u,calc.}$ (kN)		Exp/Calc.	
		$f_u=1.5*f_y$	$f_u=1.7*f_y$	$f_u=1.5*f_y$	$f_u=1.7*f_y$
#3N	89.6	77.4	85.4	1.16	1.05
#3R	86.5	71.4	79.4	1.21	1.09
#5N1	184.3	169.4	177.4	1.09	1.04
#5R1	178.0	157.4	161.4	1.13	1.10
#5N2	190.0	169.4	177.4	1.12	1.07
#5R2	188.2	159.4	165.4	1.18	1.14
Mean				1.15	1.08
COV ¹				3.51%	3.08%

¹COV = Coefficient of variation

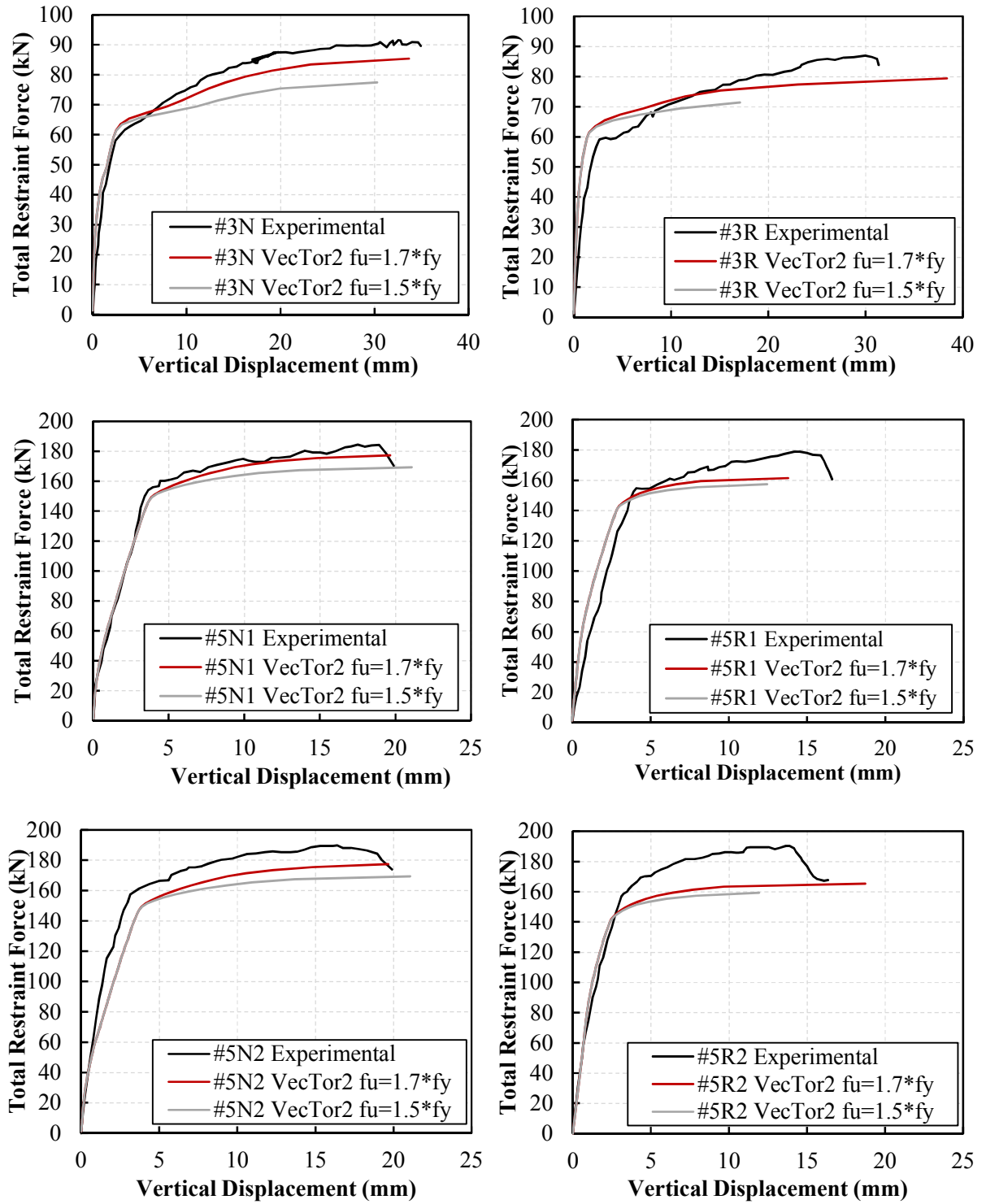


Figure 4.13 – Results of the flexural loading tests for Fan and Hanson specimens

4.3.3 Deschenes et al., 2009

An experimental program of large-scale bent cap specimens was carried out at the University of Texas at Austin to quantify the time-dependent relation between concrete deterioration and nominal shear capacity, and to develop recommendations for the assessment of in-service bent caps affected by alkali-silica reaction and delayed ettringite formation.

Six specimens, and a pilot specimen, were constructed: four of them were cast with reactive concrete and cured at high temperatures while the remaining two specimens, non-reactive, were used as a basis for comparison of long-term structural performance. Jobe-Newmann sand from the El Paso quarry in Texas was used for the reactive mixture. The target concrete strength at 28 days was 35 MPa. Table 4.12 presents the compressive strength and the age of the specimens at the time of testing.

Two independent shear tests, a deep beam shear test and a sectional shear test, were performed on each specimen; one at each end. The shear span-to-depth ratio was 1.85 for the deep beam tests and 3.0 for the sectional shear tests. All six specimens were structurally identical, with a width of 21 in (533 mm) and height of 42 in (1067 mm). The longitudinal reinforcement ratio of 3.1% was chosen such that a shear failure would be obtained, while the minimum amount of transverse reinforcement was provided to ensure that the specimen would represent the least conservative field scenario: 0.31% for the deep beam tests and 0.15% for the sectional shear tests. Crack control reinforcement was provided along the height of the beam, as shown in the reinforcement layout in Figure 4.14. Companion cylinders and prisms were cast to evaluate the compressive strength and the free expansion potential.

Table 4.12 – Concrete strength and specimens' age at testing

Specimen		f'_c	Age (days)
Non-reactive	Pilot	35	32
	nR1	51	259
Reactive	R1	31	341
	R2	29	371

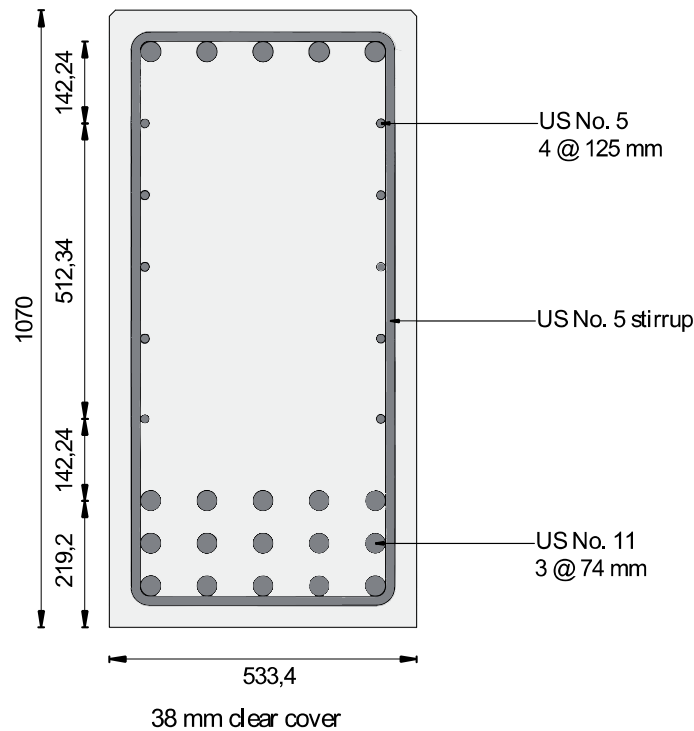


Figure 4.14 – Specimen reinforcement - cross section (adapted from Deschenes et al., 2009)

The tests revealed that the shear strengths of the sectional and deep beam shear spans were not compromised by ASR/DEF; the capacity of the reactive specimens always exceeded the capacity of the non-reactive companion beams. The confinement provided by the stirrups limited the damage of the structural core of the reactive specimens and led to a later formation of diagonal cracking prior to shear failure, as compared to the non-reactive specimen. It was concluded that any potential change in the mechanical properties of concrete was counteracted by the confining stresses due to the transverse reinforcement.

Finite element models were created, consistent with the specimens' geometric and reinforcement details. Two analyses were performed for each shear test, the variables being the concrete properties. In the first case, the compressive strength, as determined from cylinders at the time of the beams tests, together with the initial tangent modulus of elasticity, calculated as $E_c = 4500\sqrt{f'_c}$ were specified. For the second analysis, the targeted compressive strength at 28 days was utilized together with the initial tangent modulus of elasticity, calculated as $E_c = 4500\sqrt{f'_c}$. To take into account the changes in mechanical properties due to ASR, the reduction functions suggested by ISE (1992) were used. All other concrete material properties were kept as default VecTor2 values.

For the reinforcement, an elastic-plastic stress-strain behaviour with strain hardening was assumed, with the specified yield strength of 475 MPa and ultimate strength of 710 MPa as reported by Deschenes et al. (2009). The transverse reinforcement was smeared in both shear spans, as was the skin reinforcement. The longitudinal reinforcement was represented as discrete with truss bar elements. All regions were modelled with a 50 mm x 50 mm mesh. Support conditions were specified according to the experimental test set-up. The steel bearing plates were modelled with the dimensions given in the report. A bearing material with unidirectional stiffness was used between the steel bearing plates and the concrete beam. An increasing load was applied with an increment of 10 kN, as represented in Figure 4.15.

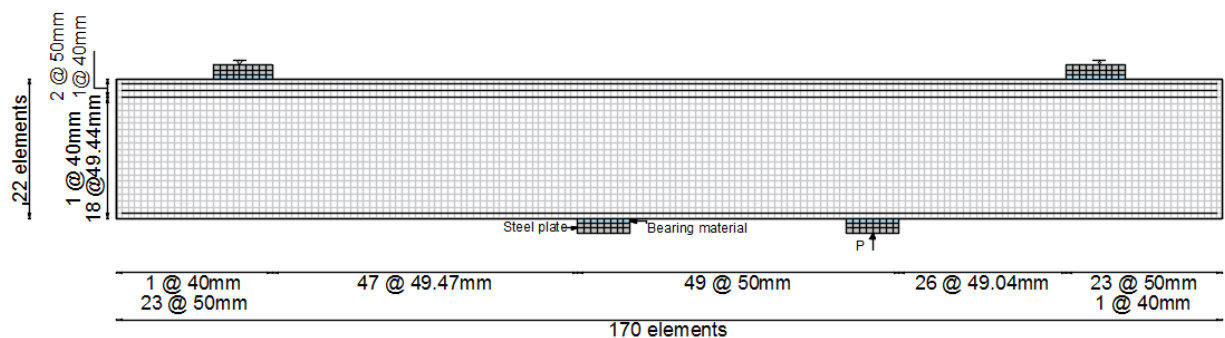


Figure 4.15 – Finite element model for sectional shear test

Four of the specimens were tested with respect to damage severity: undamaged, mild and moderate. The development of ASR/DEF deterioration was dominated by the in-plane expansion in the transverse direction, similar to the behavior reported by Multon et al. (2005). Two factors were considered to contribute to this anisotropy: the amount of reinforcement in the longitudinal direction, significantly larger than the amount of reinforcement in transverse direction, and the vertical casting direction. The minimum amount of transverse reinforcement required by AASHTO could not restrain the induced expansion; thus, the stirrups were subjected to strains larger than the yielding strain. The expansion of ASR/DEF-affected specimens was monitored in terms of transverse and longitudinal concrete core strains (ϵ_{ct} and ϵ_{cl}) and steel strains in the transverse and longitudinal reinforcement (ϵ_{st} and ϵ_{sl}).

Table 4.13 presents a summary of the induced expansions within the bent cap specimens as measured before the shear test and the results obtained analytically with VecTor2, using the Charlwood model for the ASR expansion. The other ASR expansion models yielded similar

results. In general, good agreement was obtained. The ultimate loads obtained from the theoretical analysis are compared with the experimental values in Table 4.14 and Table 4.15. The free expansions at the time of testing, determined from corresponding cylinders, were input for both reactive beams. It is seen that, for this test series, the use of the ISE ASR-correlated reductions factors for the compressive strength, tensile strength and modulus of elasticity led to better correlations to the experimental values rather than the use of properties determined from tests on cores or cylinders, contrary to the finding from the Kobayashi beams.

Table 4.13 – ASR/DEF expansion: experimental vs. calculated strains

Specimen	Experimental				Calculated			
	ϵ_{ct} ($\times 10^{-3}$)	ϵ_{cl} ($\times 10^{-3}$)	ϵ_{st} ($\times 10^{-3}$)	ϵ_{sl} ($\times 10^{-3}$)	ϵ_{ct} ($\times 10^{-3}$)	ϵ_{cl} ($\times 10^{-3}$)	ϵ_{st} ($\times 10^{-3}$)	ϵ_{sl} ($\times 10^{-3}$)
R1 DB	1.70	0.60	1.00	0.40	1.40	0.45	1.02	0.45
R2 DB	4.50	0.70	4.50	0.90	4.50	0.65	4.50	0.90
R1 SS	1.90	0.70	1.80	0.50	1.70	0.60	1.75	0.45
R2 SS	6.90	0.20	6.80	0.70	5.00	0.70	6.90	0.80

Table 4.14 – Shear strength of the deep beam shear spans

Specimen	$V_{u, test}$ (kN)	$V_{u, calc.}$ (kN)		Experimental/Calculated	
		Actual ¹	Factored ²	Actual ¹	Factored ²
Pilot DB	2630	1981		1.32	
nR1 DB	2500	2235		1.12	
R1 DB	2309	2754	2176	0.84	1.06
R2 DB	2440	2910	2363	0.84	1.03
Mean				1.03	1.13
COV ³				22.7%	11.5%

Table 4.15 – Shear strength of the sectional shear spans

Specimen	$V_{u, test}$ (kN)	$V_{u, calc.}$ (kN)		Experimental/Calculated	
		Actual ¹	Factored ²	Actual ¹	Factored ²
Pilot SS	1303	1359		0.96	
nR1 SS	1230	1504		0.82	
R1 SS	1496	1767	1486	0.85	1.00
R2 SS	1570	1890	1576	0.83	0.99
Mean				0.87	0.93
COV ³				7.5%	8.9%

¹Actual: concrete properties obtained from cylinder tests

²Factored: concrete properties calculated using the ISE reduction functions

³COV = Coefficient of variation

4.3.4 Monette, 1997

A comprehensive experimental program was carried out by Monette (1997) at the University of Ottawa on the effects of ASR on reinforced concrete beams. The behaviour of ASR-affected specimens was compared with the response of control specimens, cast with non-reactive aggregates. Eight reactive and seven control beams were cast and tested to failure. Cylinders were also cast to monitor the evolution of free expansion, compressive strength and modulus of elasticity. The CSA concrete prism test was used to determine the expansivity of the concrete mix design. The same mix design was used for all the specimens, except for the type of aggregates used: reactive and non-reactive.

The beams had the same cross section, a 90 mm width and 120 mm height, and a length of 900 mm. They were singly reinforced beams with two 8 mm diameter longitudinal bars, and 4.8 mm stirrups placed at 64 mm. Demec targets were used to monitor the expansion on various locations of the beams. One control and two ASR-affected beams were loaded at 28 days to their ultimate flexural capacity. The remainder were tested after 147 days of accelerated curing at 38°C in 1N NaOH solution to enhance the ASR development. During the curing period, the beams were stored under different loading conditions, two ASR-affected and two control beams being used for each loading case: unloaded, statically loaded, and dynamically loaded. For the purpose of this study, only the unloaded and the statically loaded beams will be investigated.

The following main conclusions were drawn from this study:

1. The unloaded reactive beams presented hogging due to differential horizontal ASR-induced strains between the top and bottom fibre.
2. The static load had the greatest effect in reducing the ASR expansion.
3. The non-reactive beams showed little or no strains.
4. The concrete cylinders experienced expansions similar to the ones measured on the top fiber of the unloaded specimens, and to the mid-span vertical expansions of all other specimens.
5. The ASR did not reduce the ultimate flexural strength of the beams.

A FE mesh for the typical simply supported beam RB-2 is shown in Figure 4.16. A total of 4400 rectangular elements, and 174 truss bars were used to represent the beam. The mesh used was 5 mm x 5 mm and all the rectangular elements had the same thickness, 90 mm. The longitudinal reinforcement was modelled as discrete reinforcement with truss bar elements connected directly to the concrete elements. However, the stirrups were modelled as smeared reinforcement included in the concrete elements. Steel bearing plates were modelled at the supports and loading locations. A bearing material with unidirectional stiffness was defined at the interface between the concrete elements and the steel bearing plates.

The default models designated in VecTor2 were used for the analysis. The material properties input for concrete were the compressive strength, and the initial tangent modulus of elasticity, as reported by Monette (1997) and shown in Table 4.16. All other concrete properties were left as default VecTor2 values. The reinforcement stress-strain response assumed a yield strength of 530 MPa, an ultimate strength equal to 640 MPa, a modulus of elasticity of 200,000 MPa, a strain-hardening strain 2.73×10^{-3} , and an ultimate strain of 100×10^{-3} .

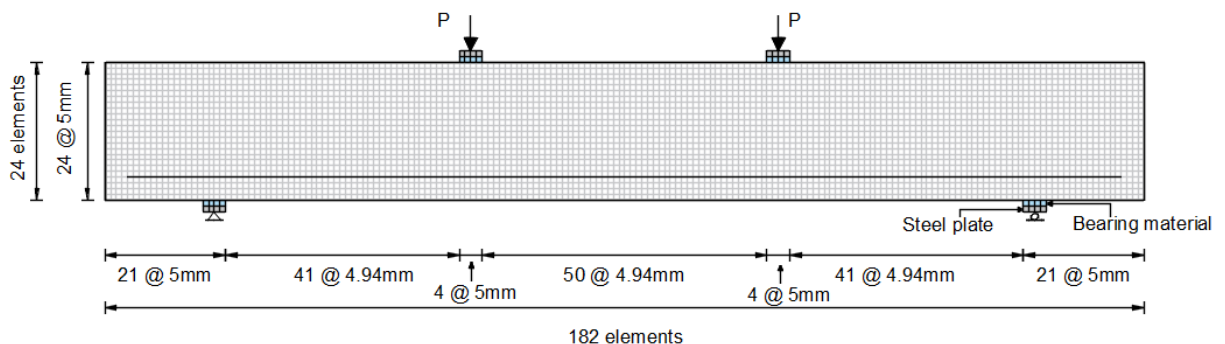


Figure 4.16 – Finite element representation of beam RB-2

Table 4.16 – Concrete properties

Specimen		f'_c (MPa)	E_c (MPa)	Age (days)
Non-reactive	NB-2	24.4	20000	28
	NB-1, NB-7	33.7	26700	147
Reactive	RB-2, RB-5	26.0	20000	28
	RB-1, RB-6	40.0	6450	147

Two types of load cases were used in the analysis. Load Case I represented the displacement-controlled point loads applied similarly to the test set-up. The loads were monotonically increased

with an increment of 0.1 mm at each step. Load Case II represented the self-weight of the beam; it was applied as gravity load, 2400 kg/m³ for all concrete elements, and held constant through the analysis.

A material-level investigation was performed as the stress-strain curves for the cylinders tested were reported. The concrete parameters input were the peak stress, f'_c and the modulus of elasticity, E_c , as reported in Monette (1997). Shown in Figure 4.17 are the stress-strain relationships for the non-reactive concrete at 28 days and 161 days. It can be seen that the default VecTor2 model for concrete in compression traces fairly well the experimental behaviour of the cylinders under uniaxial compression. The results for the reactive concrete are presented in Figure 4.18. The behaviour at 28 days is captured well by the ISE factors implemented in VecTor2, while for the cylinders tested at 147 days the default VecTor2 model for concrete compression stress-strain response calculated a lower initial stiffness, and a higher strain at peak stress, compared to the experimental behaviour. The modulus of elasticity reported for the reactive concrete at 147 days of 6450 MPa is uncommonly low for concrete with a compressive strength of 40.0 MPa. As such, the relationships used for sound concrete to describe the compression response may not be as adequate for ASR-affected concrete.

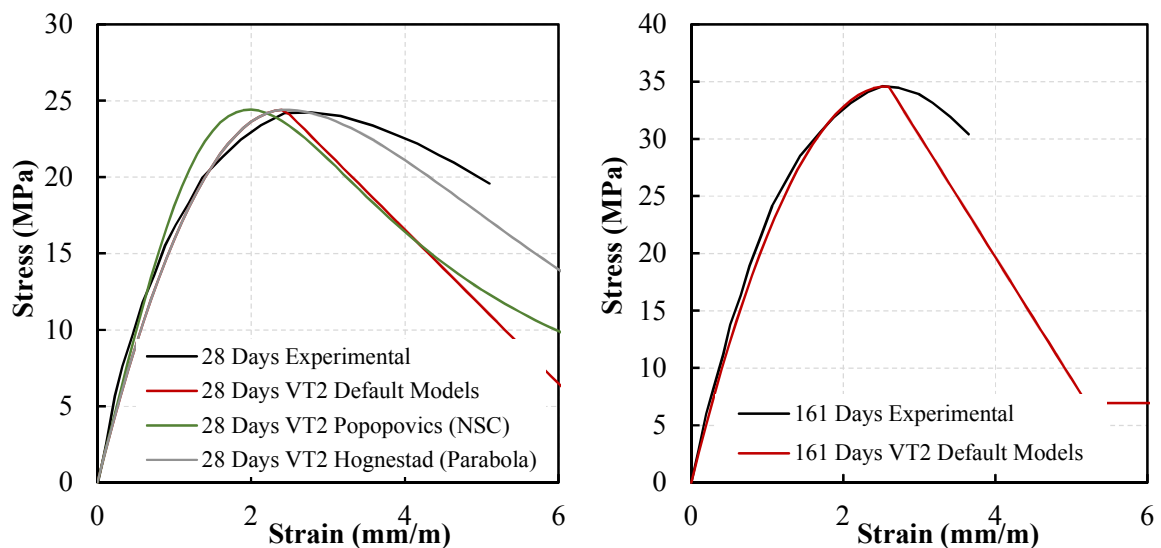


Figure 4.17 – Stress-strain curves for 28 days and 161 days non-reactive concrete

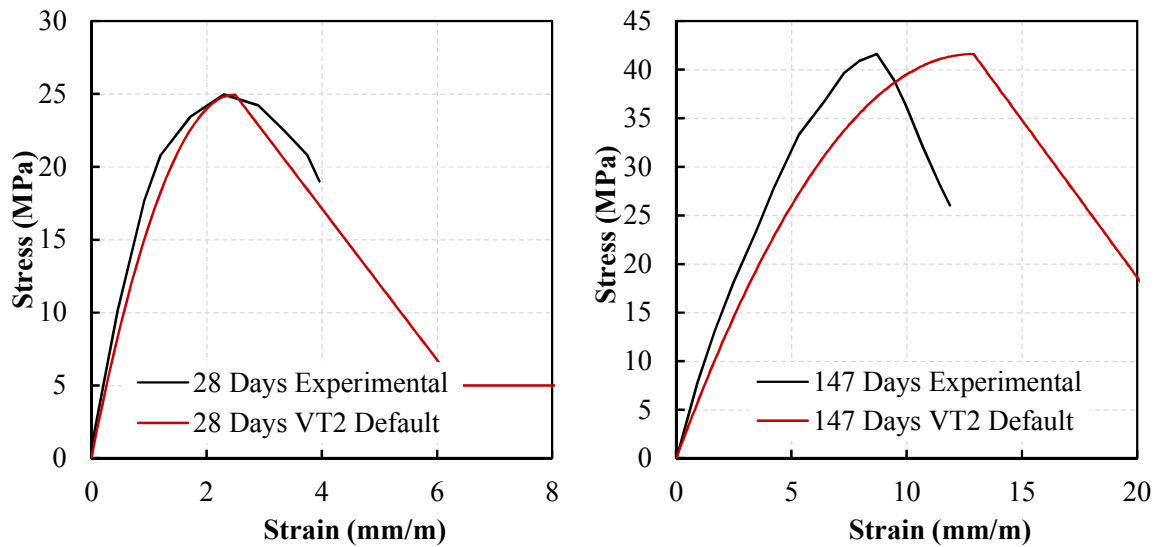


Figure 4.18 – Stress-strain curves for 28 days and 147 days reactive concrete

Figure 4.19 presents the load-deflection relationships for two non-reactive beams, tested at 28 days and at 147 days, stored under unloaded conditions. It is shown that the calculated initial stiffness is in excellent agreement with the experimentally observed one. The peak load, however, is underestimated by VecTor2 by about 10% for each beam.

The behaviour of the reactive beams is presented in Figure 4.20. For the ASR analysis, two expansion models were investigated: Charwood model and Saouma and Perotti model with and without the ISE reduction functions for the concrete mechanical properties. The ASR-induced free expansion was input, as reported by Monette (1997). The calculated response for the ASR beam tested at 28 days traces well the experimental behaviour, with a slightly higher stiffness.

For the specimen tested at 147 days, an investigation was carried out on the influence of expansion models and ISE reduction factors. As shown, for this particular specimen, they have no significant influence on the analytical response. The predicted response for the beam tested at 147 days has a lower stiffness and peak load. This may be attributed to the poor agreement at the material level between the calculated concrete compression stress-strain response and the experimentally observed one.

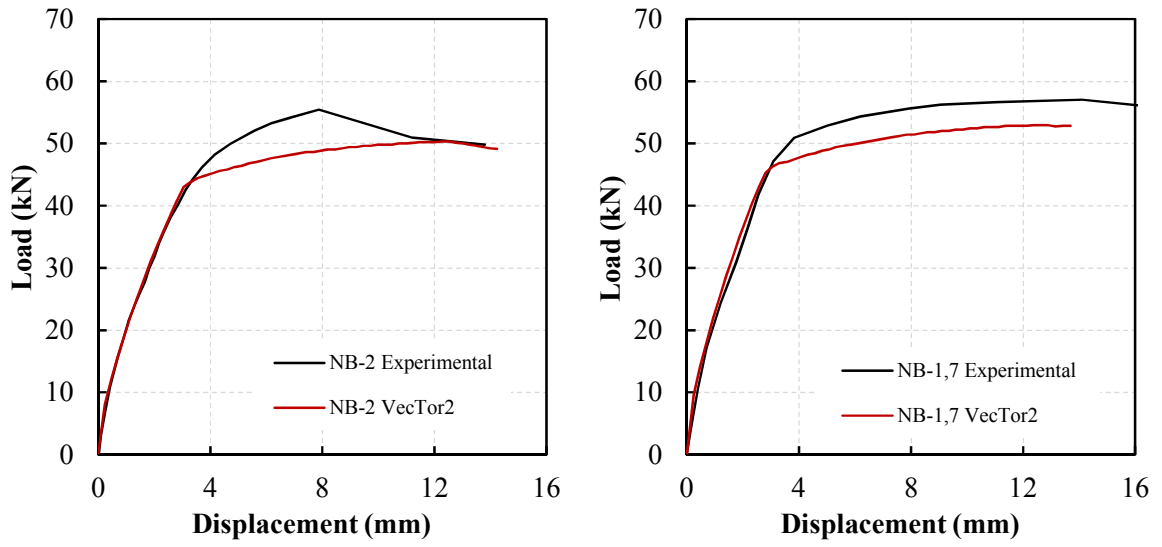


Figure 4.19 – Load-deflection relationships for non-reactive beams NB-2 and NB-1,7

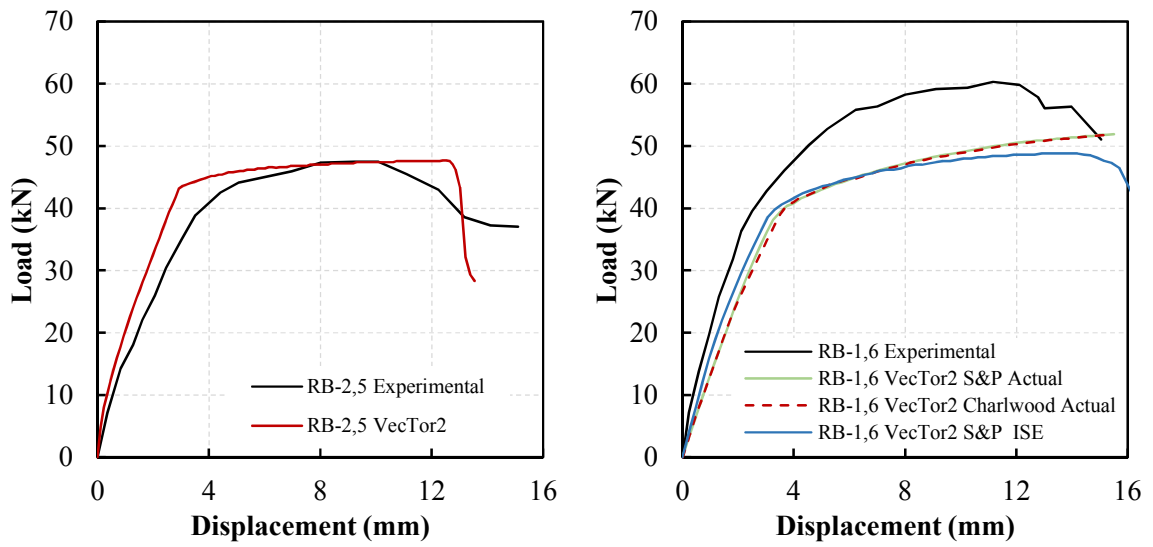


Figure 4.20 – Load-deflection relationships for reactive beams RB-1,6 and RB-2,5

Chapter 5 University of Toronto Specimens

5 University of Toronto Specimens

This chapter presents details of the experimental program carried out at the University of Toronto to investigate the structural effects of ASR on the behaviour of squat shear walls. The modelling techniques employed to analyze and predict the specimens' response are summarized, as well as the comparison between the analytical and experimental results. The tests reported herein were conducted by Farhad Habibi, under the supervision of Dr. Shamim Sheikh, as part of a study funded by the Canadian Nuclear Safety Commission.

5.1 Experimental Program

In order to investigate the structural effects of ASR, a comprehensive experimental program was initiated at the University of Toronto, involving the construction and testing of six squat shear walls, cast with two types of concrete: ASR reactive and sound concrete. All shear walls were similar in terms of reinforcement details, geometric dimensions and configuration, shown in Figure 5.1. The specimens had a barbell-shaped cross section and were built integrally with rigid top and bottom beams. The height of the shear walls, from the top of the bottom slab to the soffit of the top slab was 750 mm. The web was 100 mm thick and 1300 mm wide. The boundary elements had a thickness of 200 mm and a width of 120 mm. The bottom slab of the specimen was post-tensioned to the strong floor and anchored to prevent lateral slippage.

The horizontal reinforcement of the web consisted of 10M reinforcement bars spaced at 140 mm, with a corresponding ratio of 0.80%. The vertical reinforcement consisted of 10M reinforcement placed at 140 mm giving a reinforcement ratio of 0.77%. The boundary elements were longitudinally reinforced with five 10M reinforcement bars, and 6 mm diameter stirrups were spaced at 100 mm, with corresponding reinforcement ratios of 2.10% and 0.67% respectively. The top and bottom beams were designed with high reinforcement ratios to ensure adequate stiffness and prevent failure in these regions.

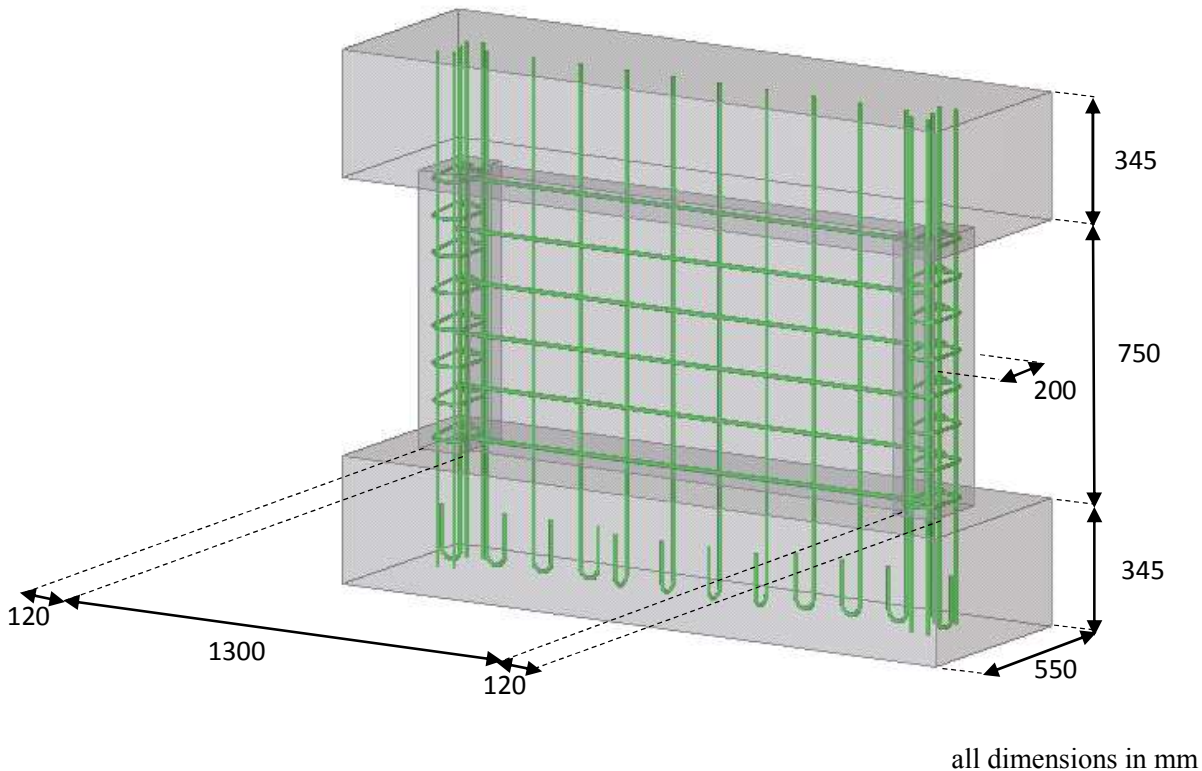


Figure 5.1 – Geometric details and reinforcement layout of shear wall specimens

As part of the first phase of testing, two shear walls were tested to failure, one control specimen at an age of 240 days, and one ASR reactive specimen at an age of 260 days. The test set-up (Figure 5.2) involved a combination of axial and lateral loads. A constant axial load of 800 kN was applied throughout the test by means of one actuator reacting against two spreader beams placed across the top beam. Two actuators, each with a capacity of 1000 kN, were used to apply lateral displacements to the shear walls. The lateral loading protocol was reversed cyclic displacement with variable cyclic increments (Figure 5.3). The loading rate started at 0.005 mm/sec; as the test progressed it was increased to 0.15 mm/sec.

Companion specimens were cast along with the shear walls to monitor the development of concrete mechanical properties and the ASR expansion. The companion specimens included cylinders, modulus of rupture bending prisms, dogbone specimens, and expansion prisms. At the day of testing, the reactive expansion prisms exhibited a free expansion of 1.85×10^{-3} . The concrete properties are shown in Table 5.1, and the reinforcement properties as determined from coupon tests are summarized in Table 5.2. The compressive strength, f'_c was determined from cylinders

with the diameter of 102 mm and with a height of 204 mm, while the tensile strength was determined from dogbone specimens.

Both shear walls failed due to crushing of the concrete in the web of the shear walls upon developing diagonal cracks. As reported by Habibi et al. (2015), the capacity of the control shear wall was 1180 kN, and the capacity of the ASR-affected wall was 1355 kN. The load-deflection responses measured during the tests of both the control specimen and the ASR wall are shown in Figure 5.4 and Figure 5.5 (Habibi et al., 2015). The regular concrete shear wall sustained the maximum load at a lateral displacement of 7.0 mm, and failed at a displacement of 8.2 mm. The ASR wall failed at a displacement of 7.1 mm.

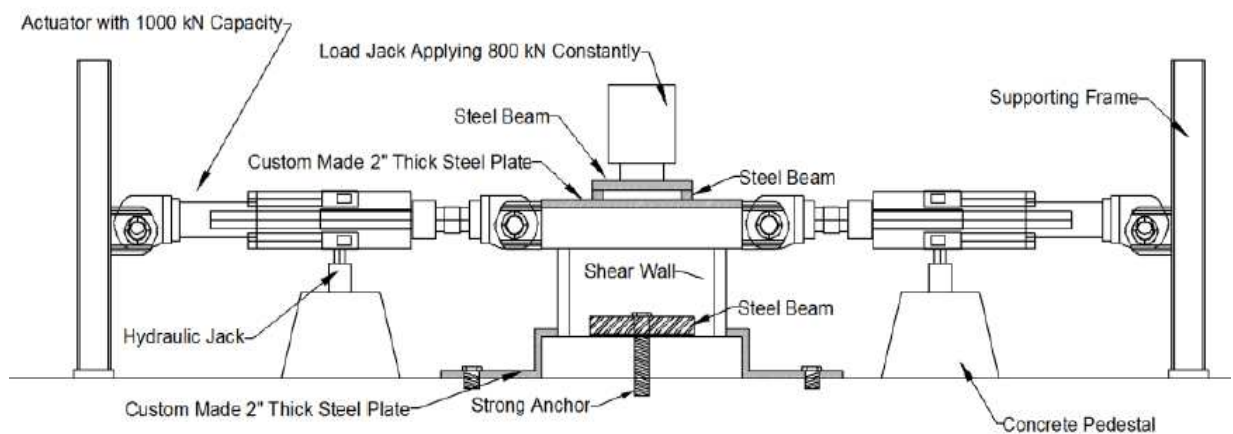


Figure 5.2 – Test set-up (Habibi et al., 2015)

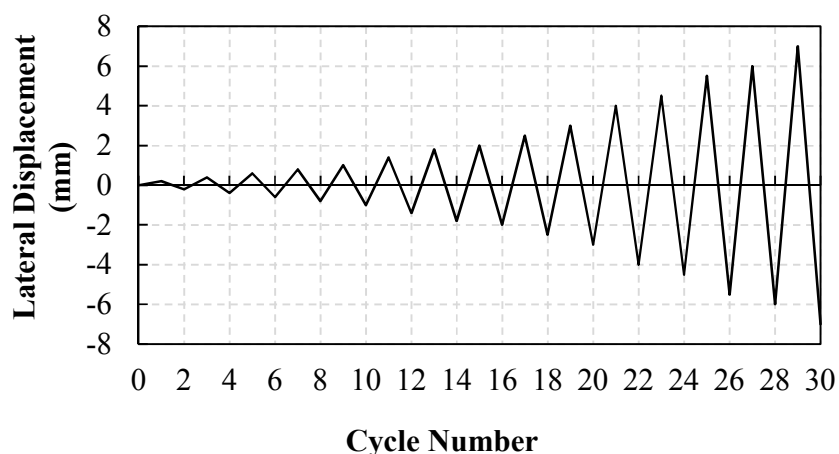


Figure 5.3 – Reversed cyclic loading history

Table 5.1 – Concrete properties (Habibi et al., 2015)

Specimen	f_c (MPa)	E_c (MPa)	f_t (MPa)	Age (days)
Regular A	79.0	47150	4.76	240
ASR A1	63.7	35750	3.24	260

Table 5.2 – Reinforcement properties (Habibi et al., 2015)

Property	A_s (mm ²)	f_y (MPa)	f_u (MPa)	ϵ_{sh} ($\times 10^{-3}$)	ϵ_u ($\times 10^{-3}$)	E_s (MPa)
10M	100	430	638	8	150	182,000
20M	300	465	550	15	200	190,000

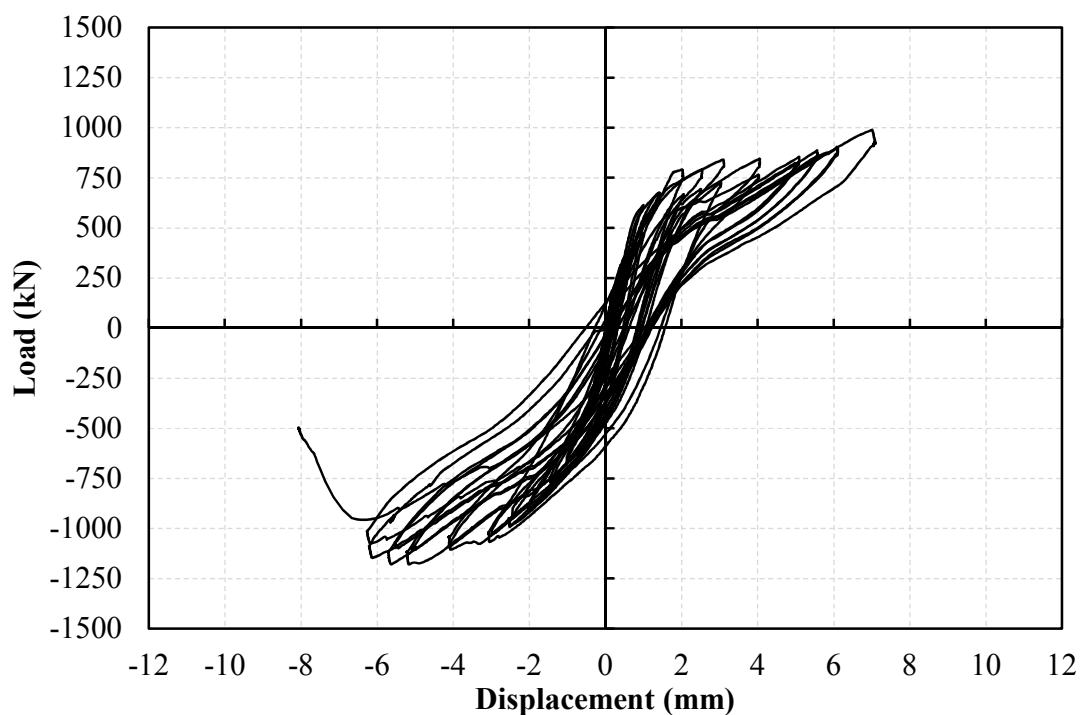


Figure 5.4 – Load-deflection relationship for the control wall specimen Regular A (Habibi et al., 2015)

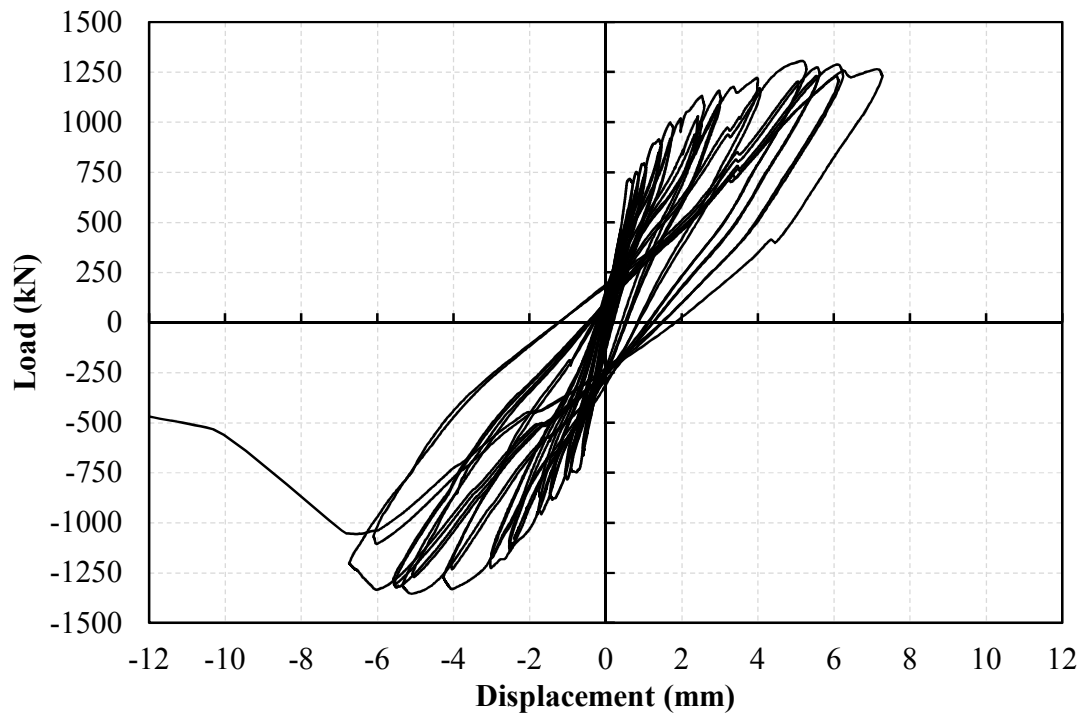


Figure 5.5 – Load-deflection relationship for the ASR-affected wall specimen ASR A1 (Habibi et al., 2015)

5.2 Two-Dimensional Analysis

Finite element analyses were performed with VecTor2 to calculate the behaviour of the shear walls; the typical mesh used is shown in Figure 5.6. A total of 2260 plane stress rectangular elements were used for modelling the shear wall specimens. The mesh was divided into a flange zone, a web zone, and top and bottom beam zones, according to the geometry of the wall. The thickness of the elements was similar to that of the specimen's sections. As such, the elements in the flanges had a thickness of 200 mm, the elements in the web had a thickness of 100 mm, while the elements in the top and bottom beams were 550 mm thick. The reinforcement was included in the concrete elements as smeared reinforcement.

The reinforcement ratios for each member, as considered in the FE analysis, are shown in Table 5.3. The out-of-plane confinement due to the stirrups in the flanges was accounted for by defining the corresponding out-of-plane reinforcement ratio. A reinforcement ratio of 2.0% was defined in each direction: horizontal, vertical, and out-of-plane for both the top and bottom beams.

The support condition was chosen such that it would be representative of the test set-up arrangement and not restrain ASR expansion. Roller supports in the horizontal direction were defined at the bottom surface of the base. At the mid-depth of the bottom beam a roller support was defined with the degree of freedom restrained in the horizontal direction.

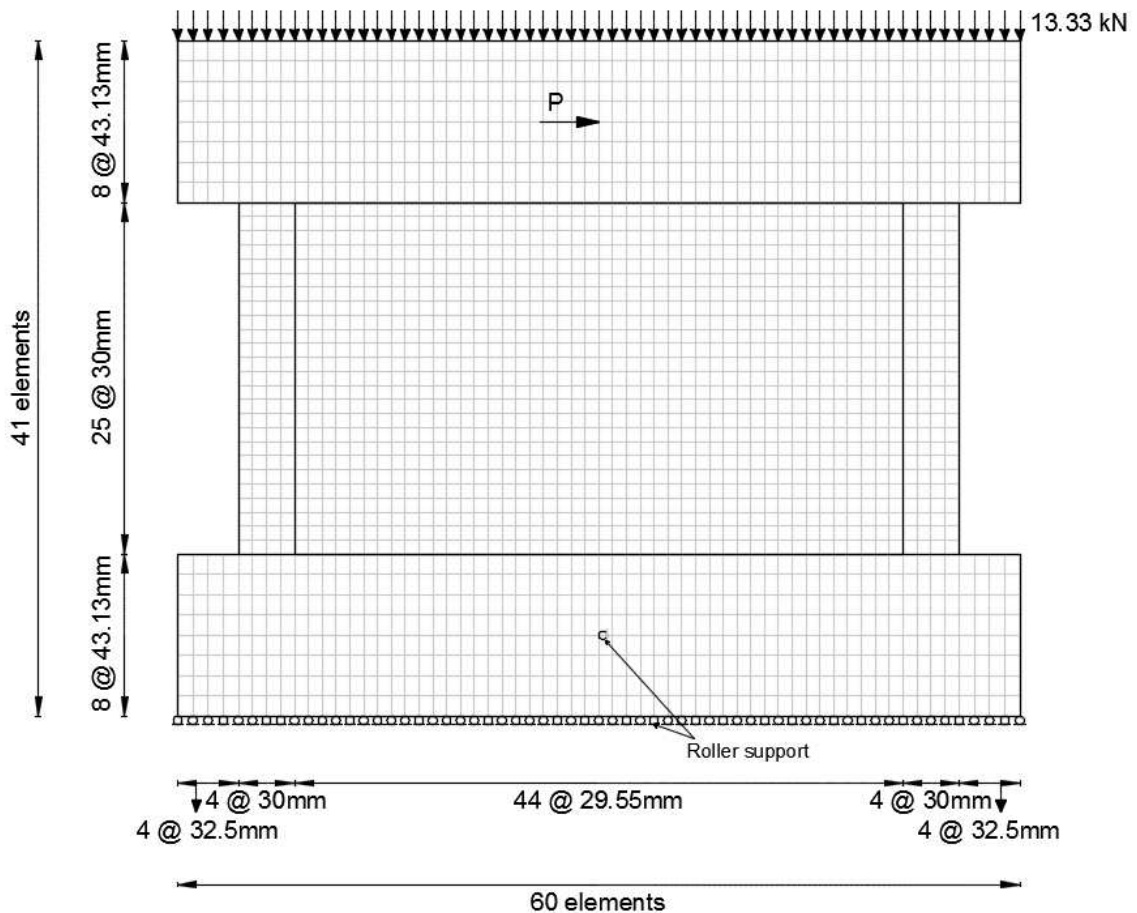


Figure 5.6 – FE model of the shear wall specimens

Table 5.3 – Reinforcement ratios

Specimen	$\rho_{h,web}$ (%)	$\rho_{v,web}$ (%)	$\rho_{h,flange}$ (%)	$\rho_{v,flange}$ (%)	$\rho_{z,flange}$ (%)
Regular A	0.80	0.77	0.67	2.10	0.44
ASR A1	0.80	0.77	0.67	2.10	0.44

Three load cases were defined for the numerical analysis of the shear walls. Load Case I constituted the self-weight of the specimen applied as gravity loads to all the concrete elements, which were assigned a density of 2400 kg/m³. Load Case II represented the lateral load applied at the mid-

depth of the top beam as a nodal displacement. To account for the axial load of 800 kN, nodal forces of 13.33 kN were applied to each node of the upper face of the top beam as Load Case III.

For the ASR-affected shear wall, several analyses were performed in order to investigate the influence of the expansion model. The free expansion of 1.85×10^{-3} , as measured on the expansion prisms, was input for all the ASR analyses. The ASR-induced strains were analysed with an iterative procedure in the first load stage of the analysis. For this initial load stage only, Load Case I, representing the wall self-weight, was activated in order to replicate the experimental loading conditions. Upon the completion of the first load stage, the lateral and axial loads were activated. The ASR strains calculated in the first load stage were carried forward, unchanged, for all subsequent load stages.

Two types of analyses were performed for each shear wall, a monotonic pushover analysis and a reversed cyclic analysis with a loading history similar to the experimental one. The walls were found to be shear-critical; the failure mechanism involved crushing of concrete in the web in vertical planes adjacent to the flanges, and in diagonal planes across the web. Figure 5.7 to Figure 5.8 show the deflection and crack pattern of the shear walls at ultimate load as obtained from the FE analysis. The results agree well with the damage observed during the test, as presented in Figure 5.9 and Figure 5.10.

Figure 5.11 and Figure 5.12 show the comparison between the calculated cyclic and monotonic responses for Regular A and ASR A1 specimens. A slight degradation in strength may be observed in the last cycles for both specimens due to concrete deterioration, as compared to the monotonic pushover. The default behavioural models designated in VecTor2 were used for the analyses and the Charlwood expansion model for ASR expansion.

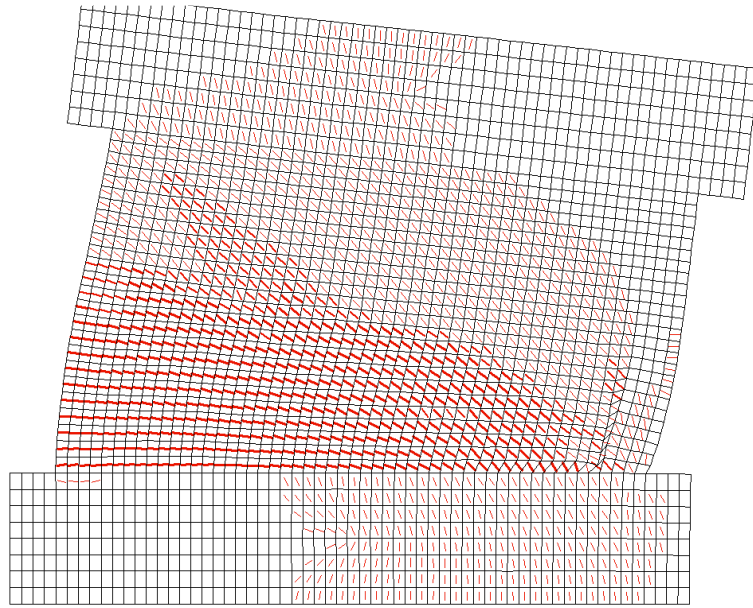


Figure 5.7 – Calculated crack pattern and deflected shape (20x) of Regular A shear wall at ultimate load

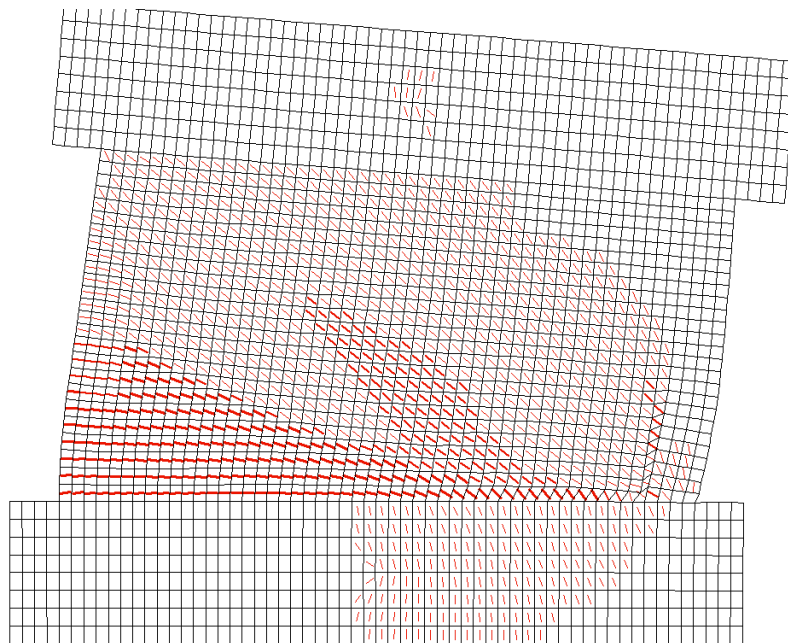


Figure 5.8 – Calculated crack pattern and deflected shape (20x) of ASR A1 shear wall at ultimate load



Figure 5.9 – Regular A shear wall at failure (Habibi et al., 2015)



Figure 5.10 – ASR A1 shear wall at failure (Habibi et al., 2015)

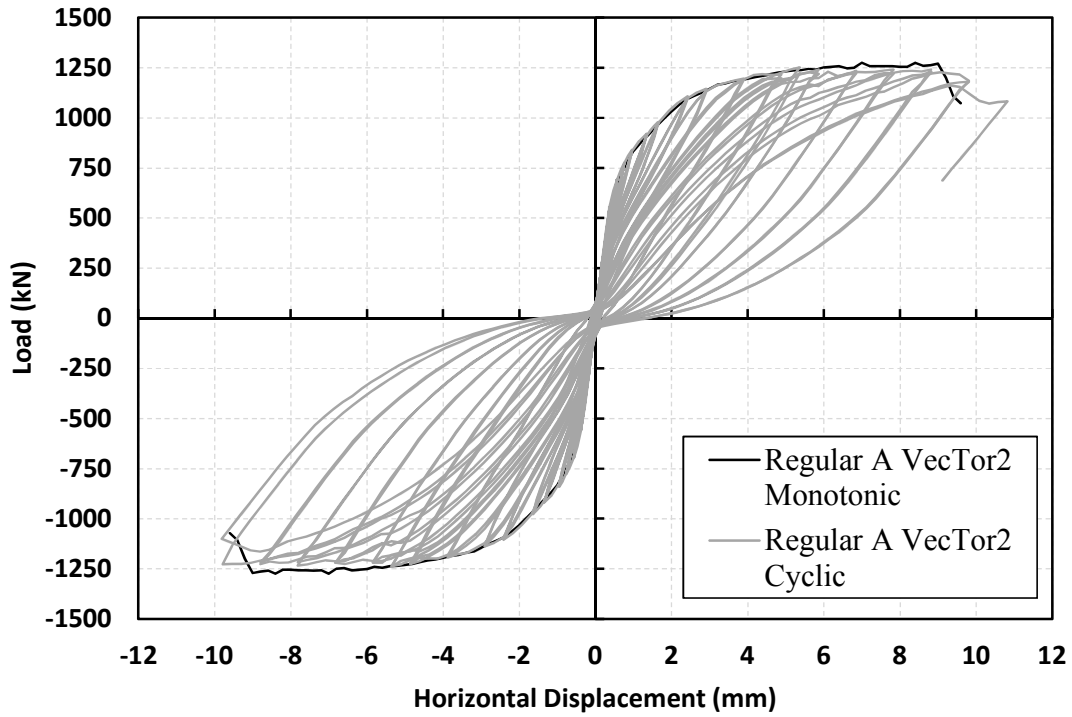


Figure 5.11 – Monotonic vs. cyclic analytical behaviour of Regular A specimen

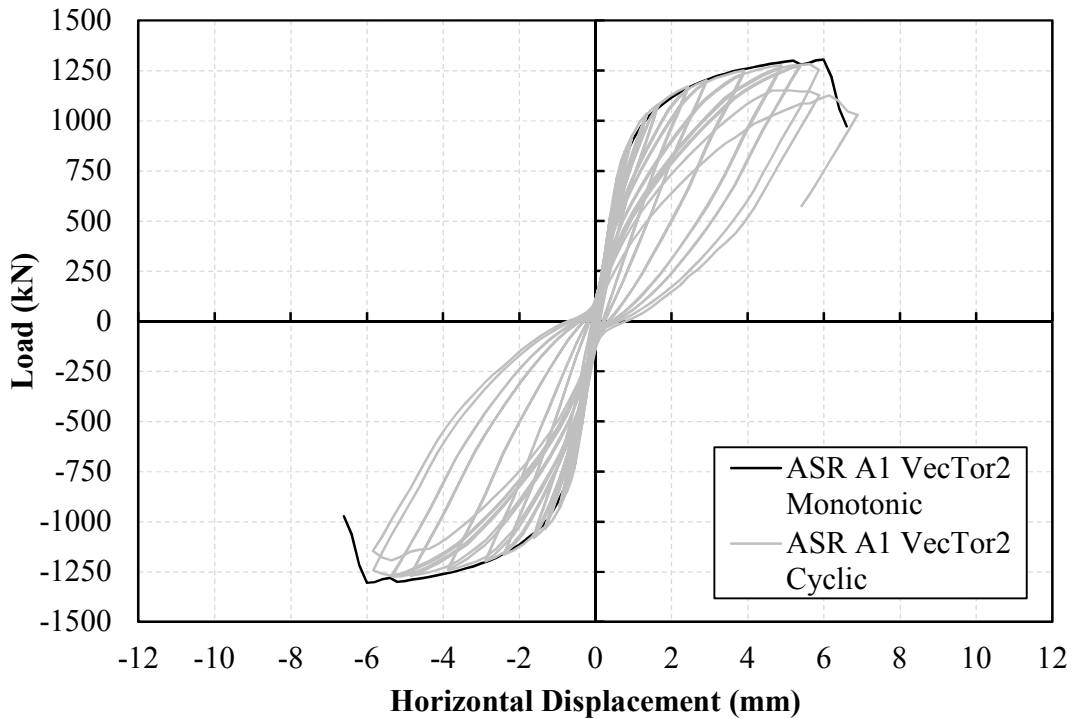


Figure 5.12 – Monotonic vs. cyclic analytical behaviour of ASR A1 specimen (Charlwood model for ASR expansion)

The VecTor2 monotonic load-deflection responses correlated reasonably well with the experimental responses as shown in shown in Figure 5.13 and Figure 5.14. The finite element analysis calculated a peak load for the Regular A shear wall of 1271 kN and an ultimate displacement of 9.0 mm, while for the ASR A1 shear wall the peak load predicted was 1310 kN at a displacement of 5.9 mm. The capacities of the shear walls evaluated during the tests were 1180 kN for the Regular A wall and 1355 kN for the ASR A1 wall. The ASR-affected specimen exhibited an overall increased stiffness. The prestressing effect of the reinforcement, together with the compressive stresses induced in the web of the ASR-affected specimen, are considered to be the mechanisms that caused the increase in ultimate strength and also the decrease in ductility.

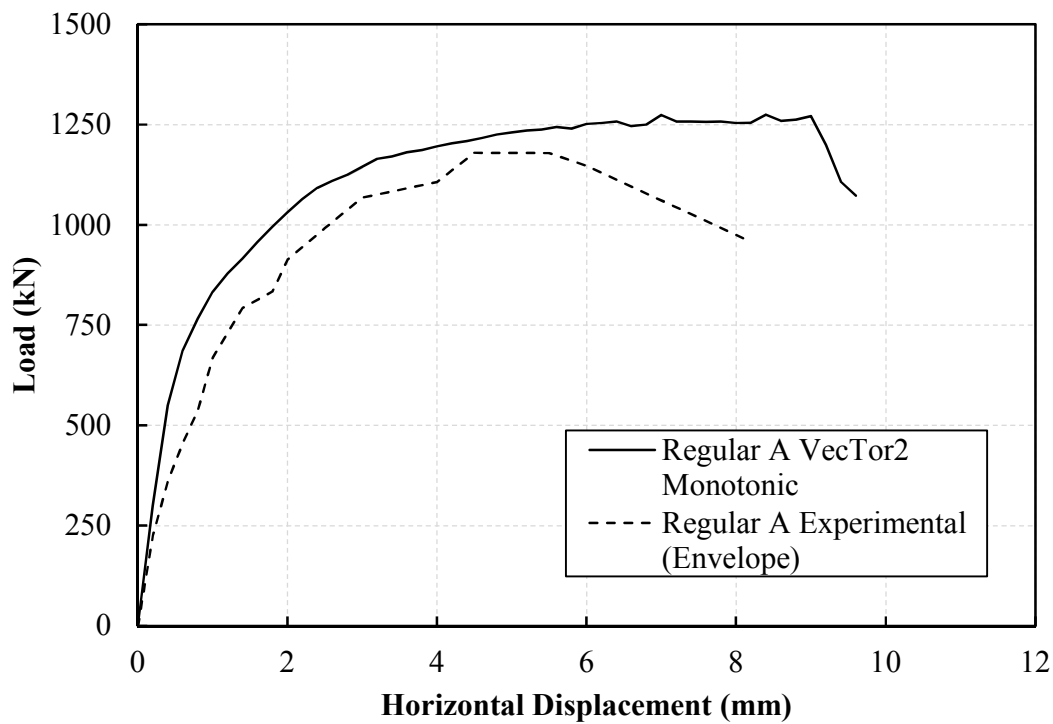


Figure 5.13 – Comparison of experimental and analytical results for lateral load versus displacement relationship of Regular A shear wall specimen

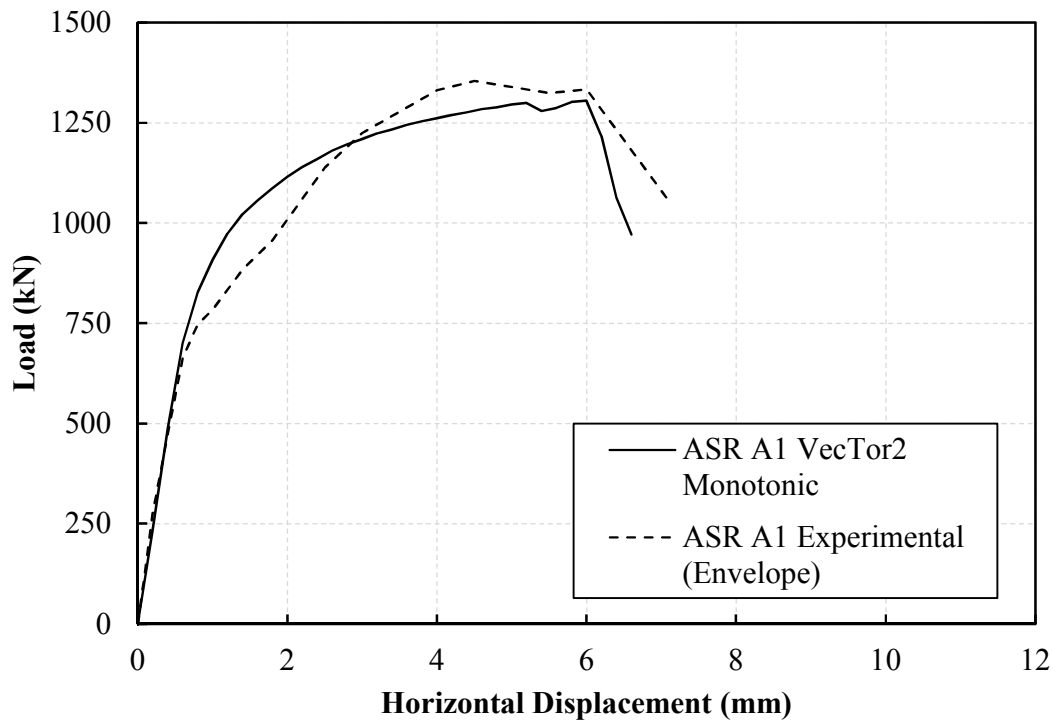


Figure 5.14 – Comparison of experimental and analytical results for lateral load versus displacement relationship of ASR A1 shear wall specimen

5.3 Three-Dimensional Analysis

Three-dimensional models (Figure 5.15) were created to match the two-dimensional models in terms of mesh size, load increment, material properties, analysis parameters, and support conditions. The web was modelled as two elements through the half-thickness, 50 mm long (44 elements) and 29.55 mm wide. The boundary elements were modelled as four elements through the half-thickness, 30 mm wide, and four elements through length, 50 mm long. The wall was discretized into 25 elements along the height. The top and bottom beam discretization followed the ones in the web and flanges.

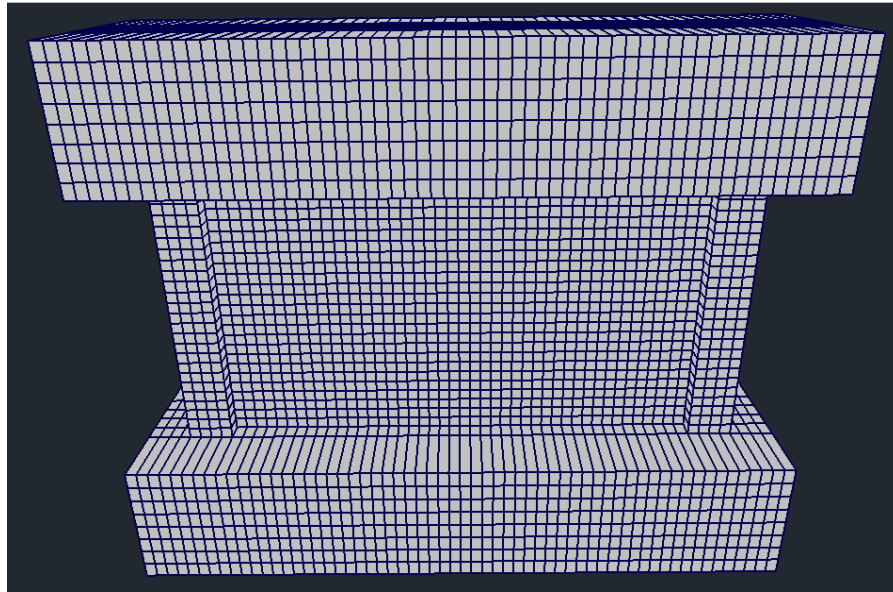


Figure 5.15 – Three-dimensional finite element model

An investigation of the three-dimensional effects was performed by comparing the load-deflection responses between VecTor2 and VecTor3 for both shear wall specimens (Figure 5.16 and Figure 5.17). The results were similar in terms of ultimate capacity, crack pattern, and failure mechanism. As can be observed, there was a difference in the initial stiffness of both Regular A and ASR A1 specimens. The response predicted by VecTor3 had a slightly increased stiffness compared to VecTor2 due to the out-of-place confining effect caused by the top and bottom beams. The web elements in the vicinity of the top and bottom beams were prevented from expanding, resulting in a relatively stiffer behaviour.

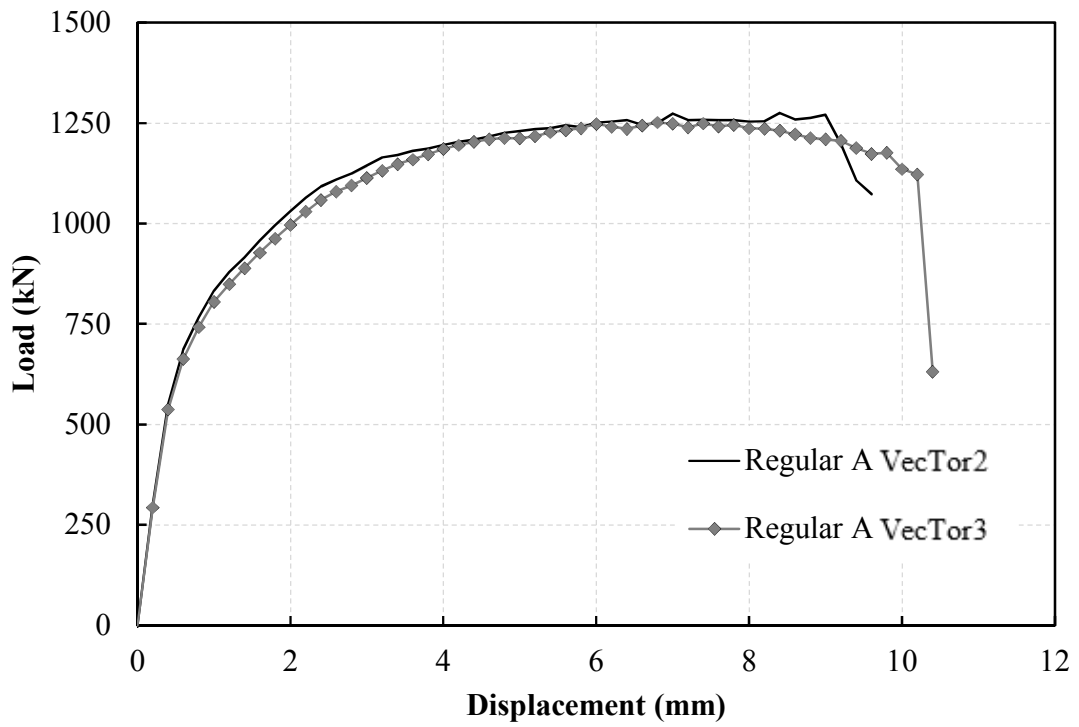


Figure 5.16 – VecTor2 versus VecTor3 responses for Regular A wall

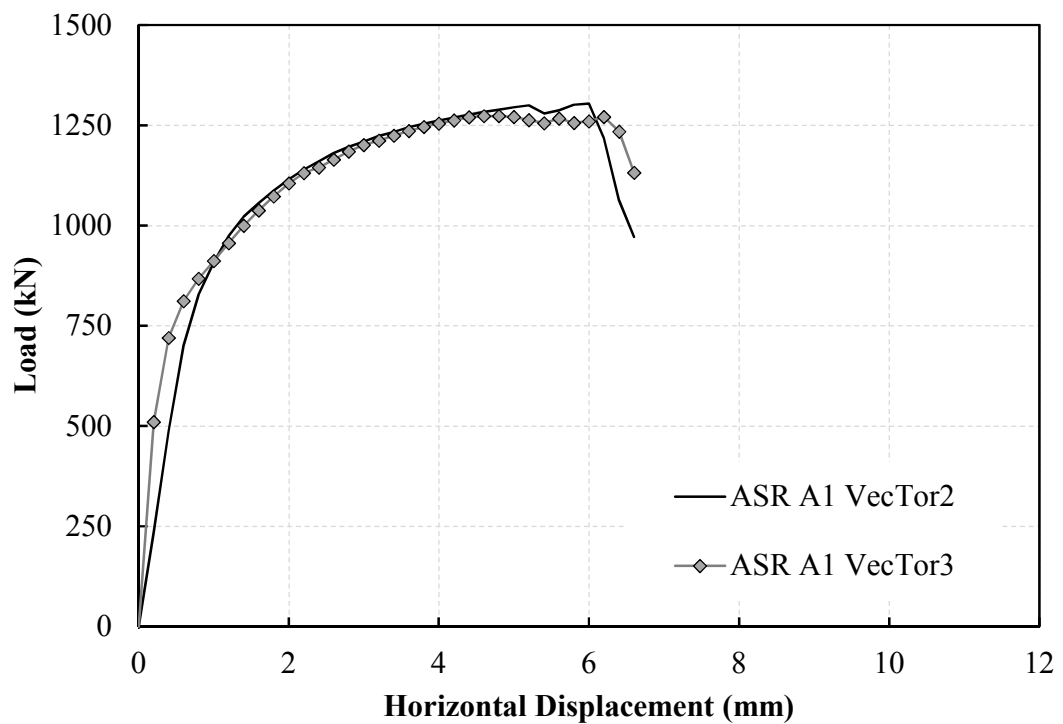


Figure 5.17 – VecTor2 versus VecTor3 responses for ASR A1 wall

Chapter 6 Assessment Recommendations

6 Assessment Recommendations

The purpose of this chapter is to review some of the currently developed assessment recommendations for the ASR-affected structures, and to provide guidance on the modelling techniques which resulted from the findings of the analytical investigations performed in this study.

6.1 Review of Guidelines on ASR-Affected Structures

Alkali-silica reaction is a major deterioration mechanism, affecting numerous concrete structures worldwide; structures in 46 countries are currently known to suffer from ASR, as reported by Doran et al. (2009). Guidelines have been developed in many of the affected countries to both limit the likelihood of ASR occurrence, and to assess and monitor the ASR-affected structures. Specifications to prevent the presence of ASR include the use of non-reactive aggregates, limiting the alkali content in the cement, and sealing the structure from moisture ingress. However, for the purpose of this work, the focus will be placed on the assessment methods of the structures in which ASR has been identified as a cause of deterioration.

Countries as United Kingdom, Canada, United States, France, Netherlands, and Japan have initiated extensive research programs which progressively enhanced the understanding of the ASR effects on concrete structures. Several guidelines were identified as representative for the current work, and some of the significant outcomes will be presented in the following subsections. The 1992 edition of the Institution of Structural Engineers 'Structural effects of alkali-silica reaction - Technical guidance on the appraisal of existing structures' represented a comprehensive basis for the assessment of various types of concrete structures in the United Kingdom. Its principles have been adopted in several other specifications: CSA A844-00 (2000) in Canada, and CUR – Recommendation 102 (2008) in the Netherlands. More recently, international research programs have augmented the ISE (1992) specifications on determining the AAR presence and its severity through the guideline issued by RILEM TC 191-ARP: RILEM AAR 6-1 Guide to diagnosis and appraisal of AAR damage to concrete in structures Part I: Diagnosis (2013). Prognosis, appraisal and management techniques will be incorporated in the upcoming Part II.

6.1.1 ISE, 1992

The ISE (1992) report, one of the most comprehensive technical guidelines on appraisal of ASR-affected structures, considers the effects of ASR on concrete as well as the assessment of specific types of structures. In the following, some of the main topics are reviewed and discussed.

The changes in mechanical properties as a result of ASR expansion proposed by the ISE (1992) were widely adopted in ASR constitutive models, and were implemented in the finite element analysis programs VecTor2 and VecTor3. The lower bounds to the compressive strength, modulus of elasticity, and tensile strength were derived from tests on laboratory specimens and cores extracted from ASR-affected structures. It is emphasised that in a structure, concrete is usually in a biaxial or triaxial stress state; thus, the damage due to ASR may be reduced, as compared to specimens under free stress state condition. As such, the use of the ISE (1992) residual mechanical properties will typically yield conservative results, as shown in Table 6.1.

Table 6.1 – ISE prediction vs. Experimental Results

Specimens	f_c , 28 days (MPa)	f_c , sound concrete, at test (MPa)	f_c , ASR, at test (MPa)	ISE (MPa)	ISE/ Test	Expansion ($\times 10^{-3}$)
U of T Shear Walls	51.0	78.8	63.7	42.0	0.66	1.8
UT Austin Beams	35.1	50.0	31.0	28.4	0.91	2.0
UT Austin Beams	35.1	50.0	28.9	21.0	0.73	7.0
Kobayashi Beam II	34.0	50.0	51.0	30.0	0.58	0.7
Kobayashi Beam III	41.0	50.0	30.0	24.6	0.82	3.0

The influence of reinforcement on the development of ASR expansion is analysed by reporting the restrained expansion with respect to the percentage of reinforcing steel (Figure 6.1), and by comparing the compressive stress induced in concrete with respect to the percentage of reinforcing steel (Figure 6.2) from various experimental programs. The restraint due to reinforcement is reported to delay the start and to reduce the rate of the reaction. Moreover, the collected data show that the compressive stresses induced in concrete due to the prestressing effect of the reinforcement increase with the rate of expansion. As such, the reaction-induced stresses in ASR-affected buildings are likely to be smaller compared to the ones in specimens stored under accelerated conditions.

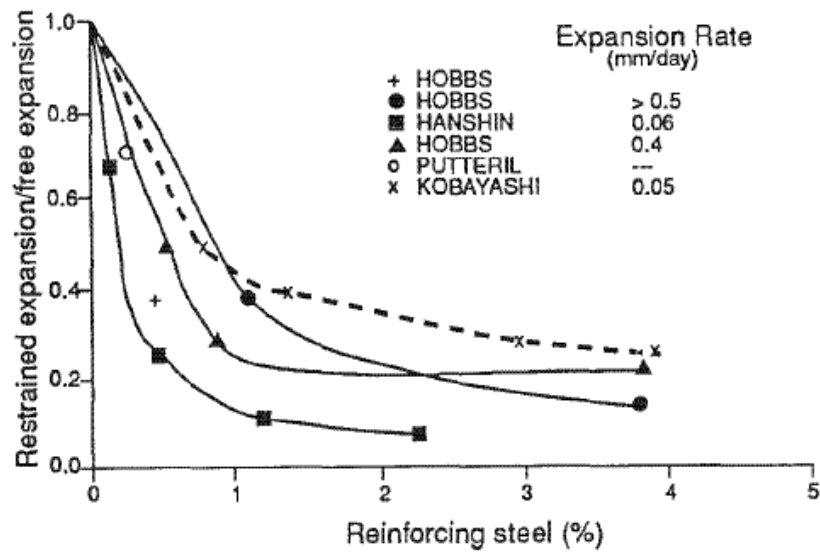


Figure 6.1 – Restrained expansion (ISE, 1992)

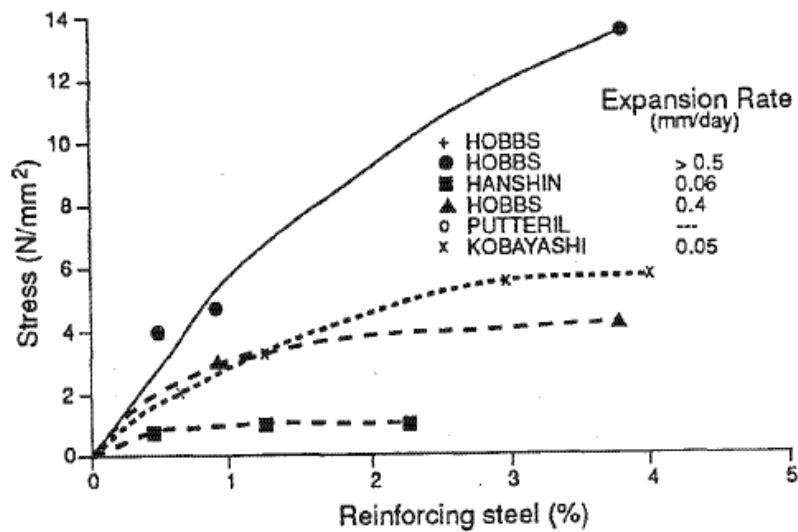


Figure 6.2 – Concrete compressive stress (ISE, 1992)

Apart from the reinforcement, the stress level was also identified as influencing the expansion. It is emphasised that the relationship between the free expansion, restrained expansion, creep, reinforcement ratio, and applied stress is not entirely understood. Nevertheless, with the available data at the time, failure mechanisms and member strength estimations were identified and developed for beams, columns, and slabs.

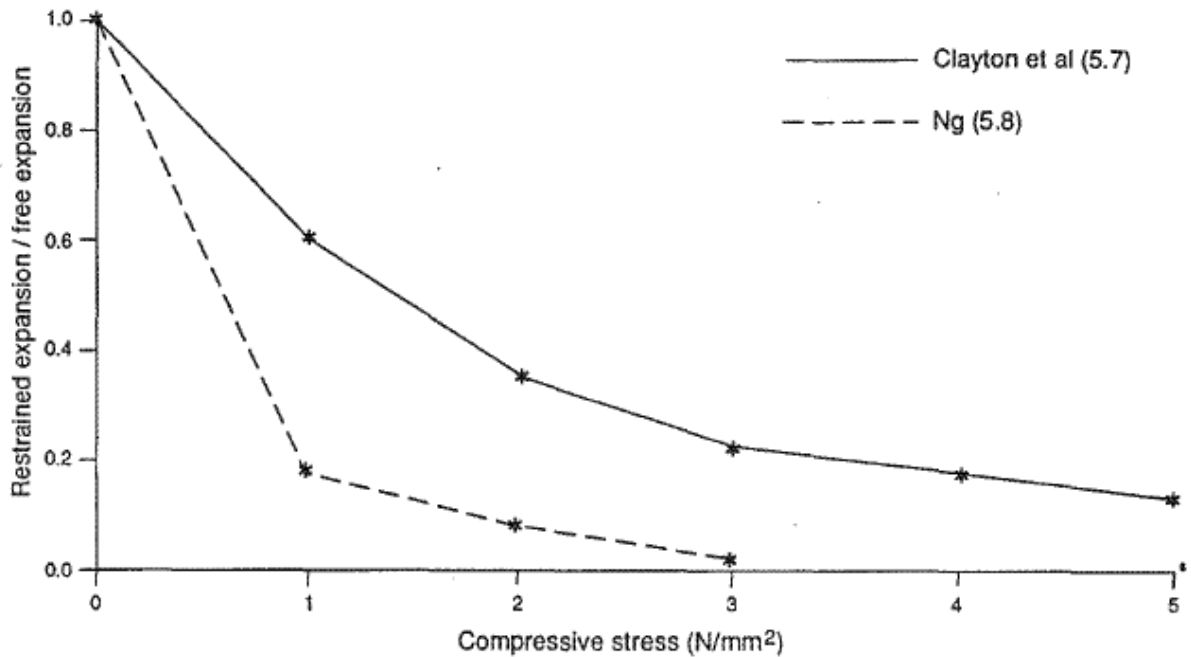


Figure 6.3 – Effect of compressive stress on expansion (ISE, 1992)

Three main aspects were treated regarding the effect of ASR on beam capacity: flexure, shear and fatigue resistance. According to the literature survey performed by ISE (1992), no significant effect on flexural strength is to be considered for free expansions lower than 6.0×10^{-3} , whereas for higher expansion levels a 25% strength reduction has been observed. Thus, the flexural capacity should be assessed using conventional models, with reduced concrete properties. The shear capacity is reported not to be adversely affected by ASR, if a minimum of 0.2% transverse reinforcement is provided. Due to the prestressing effect, up to a 47% increase in capacity has been reported in some tests (Inoue et al., 1989). The shear capacity is recommended to be evaluated taking into account the compressive stress resulting from the prestressing effects, and using reduced mechanical properties. The fatigue life is reported to be unaffected by ASR.

The ISE (1992) recommendations for the assessment of slab strength include, in addition to the failure mechanisms presented for beams, the punching shear failure mode. No significant reduction in punching shear capacity is reported for free expansions lower than 6.0×10^{-3} . Delamination parallel to the reinforcement may occur for higher expansion levels. It was reported by Ng (1991) that the slab may be divided longitudinally in three layers, leading to a 30% reduction in capacity. The punching shear capacity is suggested to be evaluated using conventional methods for prestressed concrete slabs with the mechanical properties of ASR-affected concrete.

Three effects on concrete column strength have been identified. The first one is the reduction in compressive strength, which may be accounted for through the use of an appropriate strength factor in the conventional methods. The second effect of ASR is the delamination which may occur in the plane of the longitudinal reinforcement (i.e. cover spalling). The potential implications of delamination are a loss in buckling restraint for the reinforcement, and a reduction of the cross section, both of which may in turn have a direct effect on the stability of the column. The third effect, unlikely to occur in practical situations, involves the crushing of concrete prior to yielding of the reinforcement due to the ASR-induced compressive stresses.

The ISE (1992) guideline also provides recommendations for the evaluation of bond strength reduction. No significant reduction is considered to occur for expansion levels lower than 4.0×10^{-3} in the case of bars restrained by stirrups, or with a concrete cover that is at least four times the diameter of the bar. For bars that are not restrained by stirrups, or with a concrete cover lower than 1.5 times the diameter, a 50% strength reduction was reported. The reduction is considered to be proportional to the reduction in splitting tensile strength.

The general assessment procedure proposed by ISE (1992) is presented in Figure 6.4. The initial overall evaluation of the structure consists of a study meant to establish whether ASR is the cause of cracking. This investigation is recommended to include the evaluation of the stress level under the existing loading, reinforcement detailing, moisture ingress, concrete mix design, and petrographic examination. Provided that ASR is found to be a contributing factor, a series of checks for structural significance are recommended. These checks involve the evaluation of the severity of expansion, site environment evaluation, reinforcing detailing, consequences of failure, stress level, and residual concrete properties. The severity of the expansion is linked with three classes of reinforcement detailing, provided for slabs, beams and columns. Appropriate action measures are suggested for each combination, accounting for the efficiency of the reinforcement in counteracting the expansion.

It is recommended that two structural appraisals be performed: one based on the current condition of the structure, and the other based on the estimated expansion at some time in the future. The crack width summation is the method proposed to evaluate the level of current expansion, a procedure disputed by other researchers (Deschenes et al., 2009; Saouma and Hariri-Ardebili,

2014). For the prediction of the potential future expansion, the ISE (1992) recommends tests performed on cores extracted from the structure.

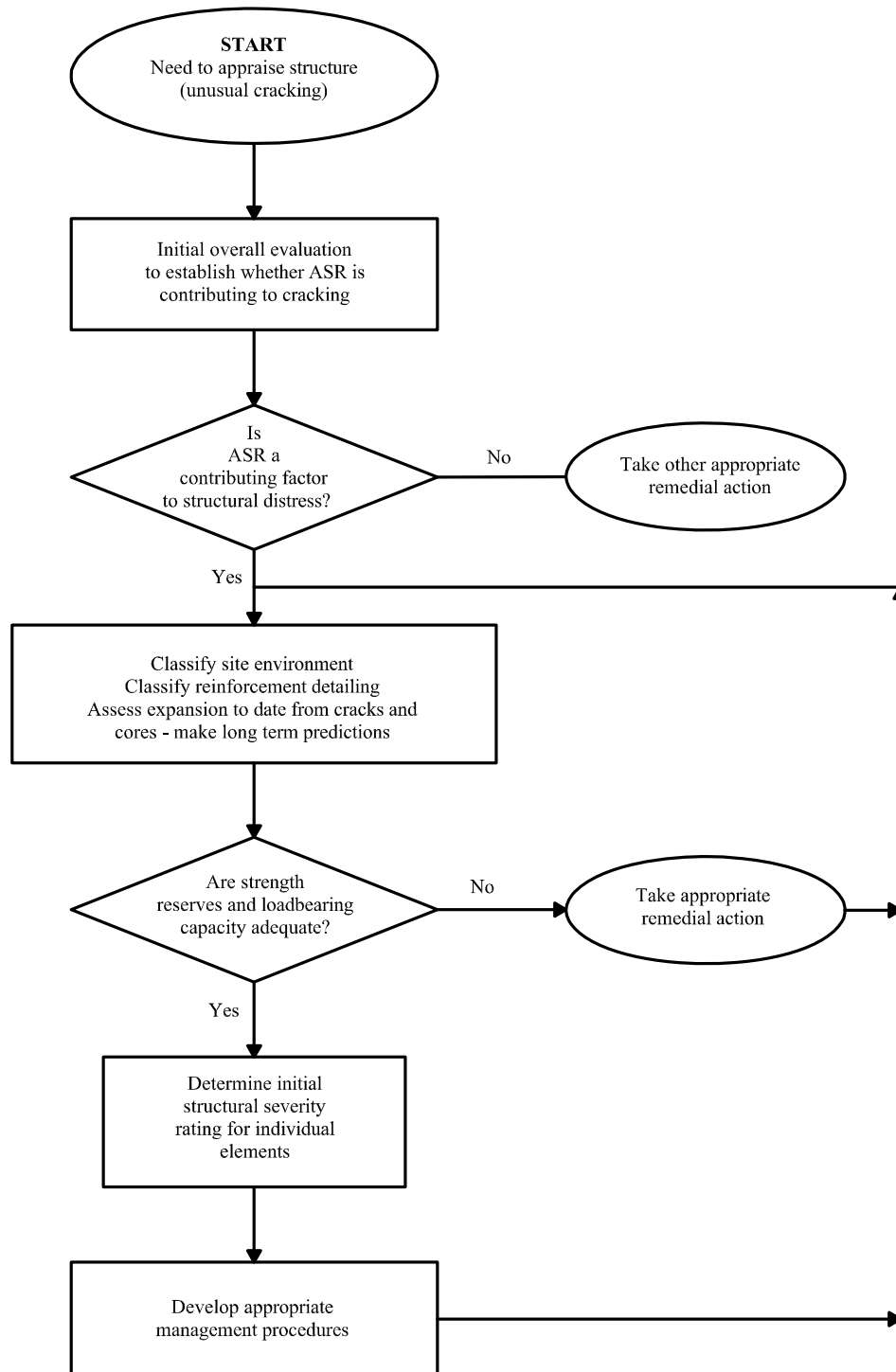


Figure 6.4 – Appraisal leading to diagnosis and action following ASR (ISE, 1992)

Several management procedures of ASR-affected structures are suggested, depending on the type of structure. The following measures have proven to be efficient in several applications: large struts or buttresses to counteract the compressive loads, prestressed anchors, slot cutting, injections with carbon dioxide, and waterproofing. Instrumentation of the ASR-affected structure is recommended by ISE (1992) to monitor the development of cracks, strains, and relative displacement of joints.

The report highlighted the following research needs at the time, some of which have been addressed by more recent experimental studies: influence of restraint on the expansion, stiffness deterioration, bond testing, and development of relationships to quantify ASR effects correlated with the limit state design.

6.1.2 CUR – Recommendation 102, 2008

The identification of ASR as the deterioration mechanism of several bridge decks and lock walls in the Netherlands led to the development of two guidelines focused on the prevention of ASR (CUR – Recommendation 89, 2006), and on the inspection and structural evaluation of ASR-affected structures (CUR – Recommendation 102, 2008). For the purpose of this work, some of the relevant outcomes of the CUR – Recommendation 102 (2008) will be presented. It is to be noted that the structural assessment was developed based on laboratory tests done at the Delft University of Technology, performed on slab strips sawn from ASR-affected decks, presenting extreme internal ASR cracking (Figure 6.5). As such, it is limited to plate-shaped structures with a thickness of at least 400 mm, having bidirectional reinforcement.

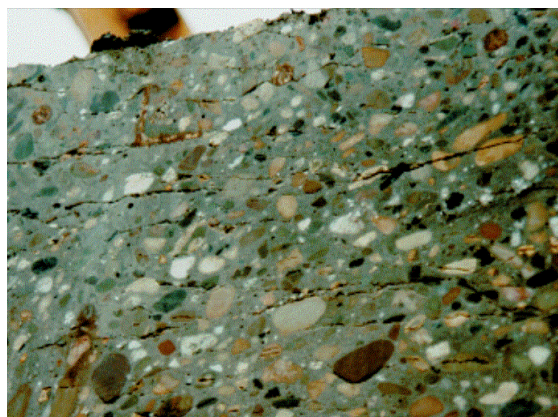


Figure 6.5 – Internal ASR cracking in a vertical section of the bridge deck (Bakker, 2008)

The flow chart for inspection and studies, presented in Figure 6.6, represents a step-by-step approach, generally following the ISE (1992) recommendations and assessment actions. Different types of investigations are to be performed as follows:

1. Class I – Exploratory investigation: to determine whether ASR is the cause of cracking by analysing the crack pattern, identifying the presence of alkali-silica gel, and evaluating the ingress of moisture and de-icing salts.
2. Class II – Technical study: to quantify the damage, and to determine the uniaxial tensile strength perpendicular to the span by testing cores extracted from the structure.
3. Class III – Targeted study: to determine the reinforcement configuration, and the tensile and compressive strength for the structural assessment evaluation.
4. Class IV – Structural study: to determine the safety of the structure.

The CUR – Recommendation 102 (2008) provides guidelines for recording the crack pattern and for determining the cumulative crack width per metre (Figure 6.7), used for the classification within a certain crack width class. Similar to the ISE (1992), the structural risk is deduced based on the reinforcement configuration and consequences for safety (Table 6.2).

For the structural evaluation, several aspects require consideration: cracks and deformations caused by ASR, the residual tensile and compressive strength, and the variation of the tensile strength for the cross section analyzed and in between. The changes in the distribution of internal forces, and in the eccentricity of normal forces, together with the presence of additional loads caused by ASR expansion need to be analyzed. According to CUR – Recommendation 102 (2008) it is only necessary to verify the shear strength; the moment capacity is assumed to be not significantly reduced. As such, the guideline contains provisions for determining the design value of the shear stress, based on the experimental work performed at the Delft University of Technology. The main disadvantage of this calculation method is the fact that it is based on the average tensile strength, obtained from uniaxial tension tests on concrete cores. The reliability of the test is disputable due to the various parameters which may influence the result, other than the concrete tensile strength.

The code also specifies a series of control measures to be taken if the presence of ASR has been identified. The measures depend on the risk classification, tensile strength, and the levels of cracks present. Some of the suggested actions are: sealing against moisture, crack monitoring, limiting

the risk of reinforcement corrosion, applying reinforcement, and slot cutting; these are similar to the ISE (1992) recommendations.

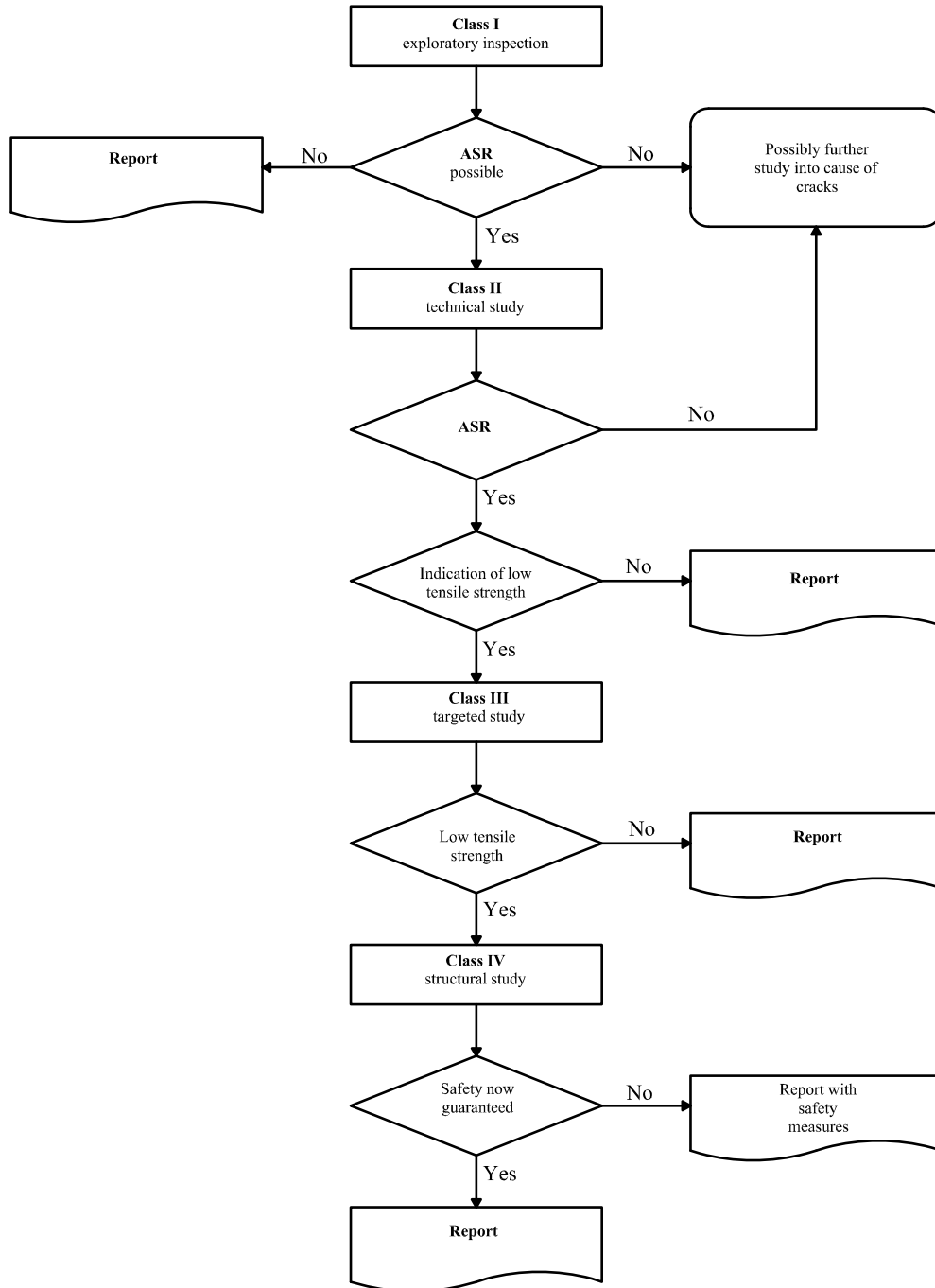


Figure 6.6 – Flow chart for inspection and studies (adapted from CUR – Recommendation 102, 2008)

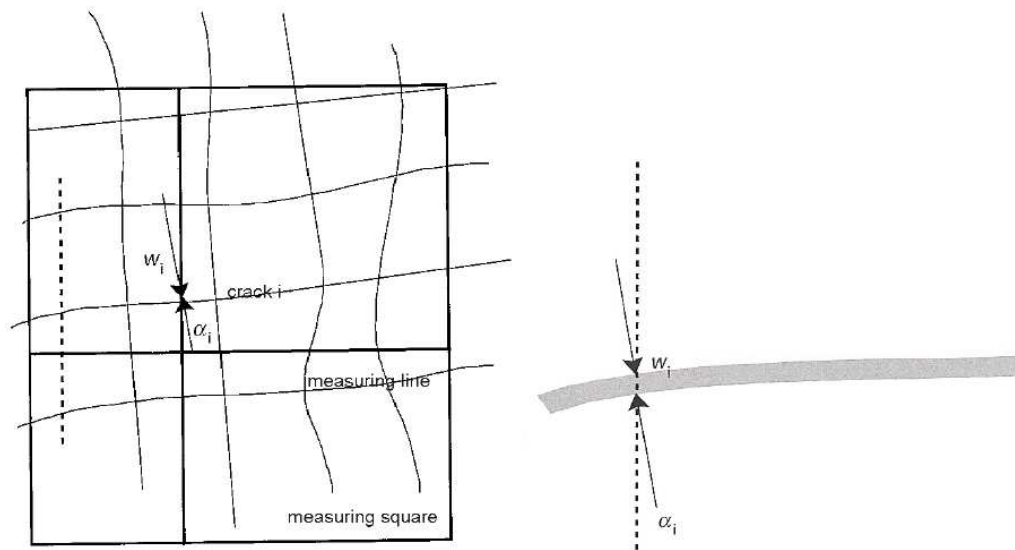


Figure 6.7 – Principle of measuring the relative cumulative crack width (CUR – Recommendation 102, 2008)

Table 6.2 – Structural risk (CUR – Recommendation 102, 2008)

Reinforcement configuration	Consequences for safety and functioning	
	Major	Minor
High quality 3D reinforcement	Structural risk = medium	Structural risk = low
Three-dimensional reinforcement with moderate anchoring	Structural risk = medium	Structural risk = low
Two-dimensional reinforcement with good or moderate anchoring	Structural risk = high	Structural risk = medium

6.1.3 CSA Special Publication A864-00, 2000

The Canadian CSA A864-00 'Guide to the evaluation and management of concrete structures affected by alkali-aggregate reaction' (2000) provides recommendations on the diagnosis and management of concrete structures affected by ASR. The general procedure, presented in Figure 6.8, largely follows the ISE (1992) provisions.

The CSA A864-00 (2000) provides various assessment field techniques for different types of structures: dams, bridges, pavements, median barriers, buildings, and retaining walls. Emphasis is placed on the cracking pattern, differential movements, surface discolouration, presence of gel, and popouts. Core extraction is recommended for investigations on ASR presence, potential for further expansion, and mechanical properties of concrete.

The main difference from the ISE (1992) recommendations is the strength assessment method. According to CSA A864-00 (2000) the anisotropic changes in material properties due to AAR need to be incorporated into the analysis. Therefore, conventional methods are considered to be invalid, and numerical ASR simulations are recommended for the analysis. Several macro-models, some of which have been implemented in VecTor2 and VecTor3, are recommended for the ASR simulation models. The CSA A864-00 highlights the necessity of numerical calibration against field observations: displacements, strain level in the reinforcement and concrete, along with the simulation of the creep behaviour of concrete.

Different aspects which require consideration are formulated depending on the type of concrete structure: plain concrete or reinforced concrete. In the case of mass concrete structures attention should be placed on the formation of major cracks which may cause stability issues, on the potential of sliding of the horizontal joints, triaxial strength of concrete under the field stress condition, and the potential for crushing of concrete at sections with abrupt geometry changes. For the reinforced concrete members, the effects of yielding of the reinforcement and the compressive stresses induced in concrete due to ASR-induced strains have to be taken into account, as well as reduction of bond strength and delamination.

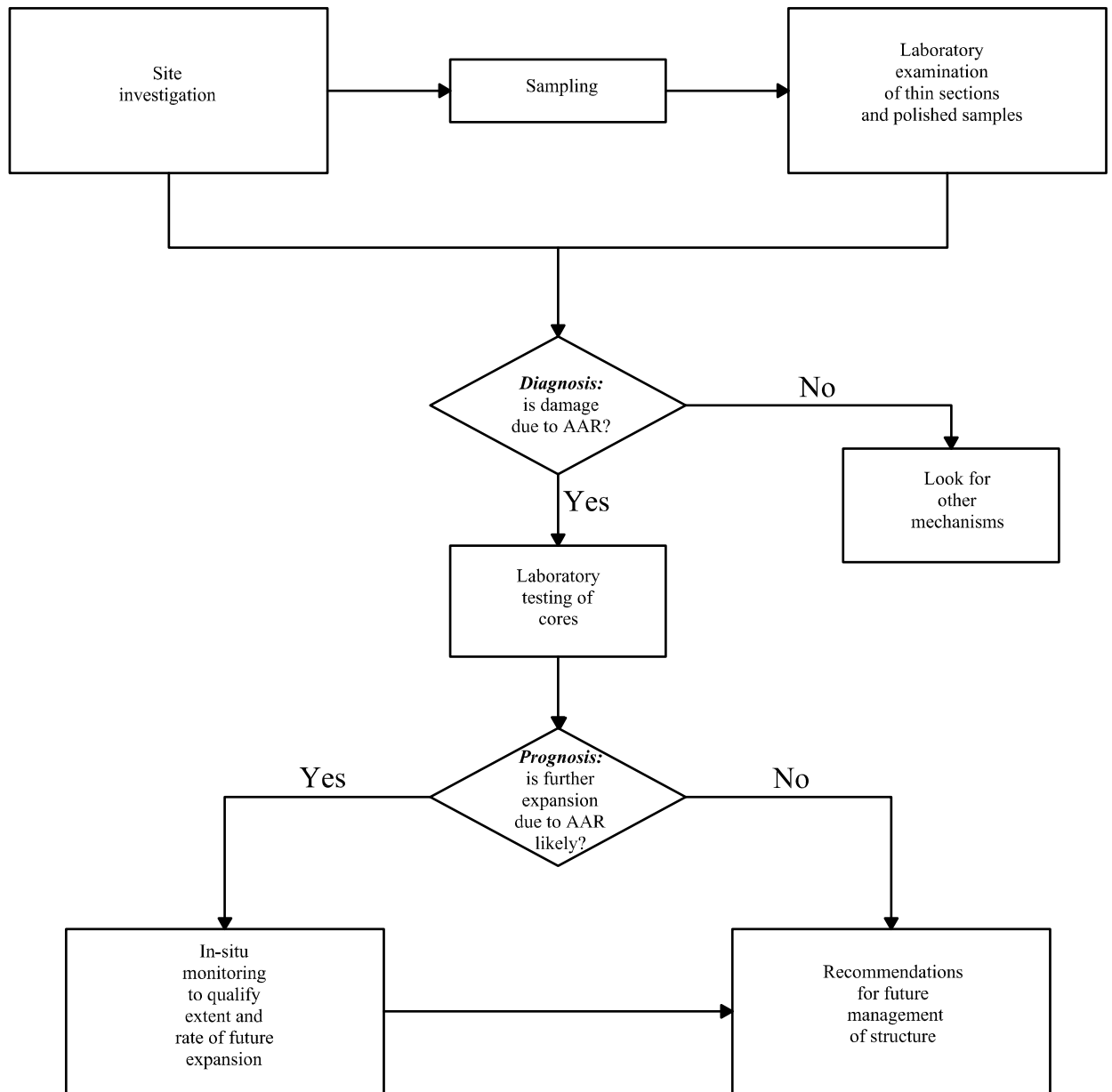


Figure 6.8 – Procedure for the diagnosis of AAR in structures (adapted from CSA A864-00, 2000)

6.2 Modelling Recommendations

The literature review of currently available recommendations on the assessment of ASR-affected structures provides little to no guidance on the modelling techniques that should be employed when severe ASR is identified, although the need for numerical simulations has been established due to the complexity of the effects ASR has on structures. The RILEM Technical Committee ISR – ‘Prognosis of deterioration and loss of serviceability in structures affected by alkali-silica reactions’ is currently developing recommendations for finite element simulations of concrete structures in which the presence of ASR has been identified. The verification studies performed in this thesis, using the programs VecTor2 and VecTor3, have yielded conclusions which may help inform such recommendations.

As described in Chapter 3, two distinct mechanisms have been considered when modelling ASR effects in reinforced concrete structures: the chemically-induced expansion and the accompanying degradation of the mechanical properties (compressive and tensile strengths, and modulus of elasticity). The expansion due to ASR may be evaluated using one of the several state-of-the-art models implemented, while the degradation of mechanical properties may be accounted for through the ISE (1992) reduction functions or by directly specifying the determined values.

For the ASR analysis, an estimation of the current level of free expansion is required. This may either be input by the user, or, provided that sufficient parameters describing the reaction kinetics are known, the free expansion may be estimated by the Saouma and Perotti (2009) or Sellier et al. (2015) models.

Several of the most commonly used ASR macro-models have been implemented in both VecTor2 and VecTor3. Although different in terms of formulation, the comparison between the various expansion models revealed no significant influence on the overall structural behaviour of reinforced concrete beams, prestressed concrete beams, and shear walls. However, the experimental studies which reported both the level of free expansion and the concrete or reinforcement strains permitted a further comparison between the expansion models. The conclusion was that although for certain cases some models may estimate the stress level due to ASR expansion more accurately than other models, the difference has no significant influence on the structural behaviour.

The degradation of the mechanical properties on the other hand, had a significant effect on the predicted response of the ASR-affected concrete elements. The use of ISE (1992) reduction functions always yielded conservative results, nevertheless, in some cases they underestimated the concrete properties significantly.

The anisotropy of the expansion yields a certain anisotropy in the mechanical properties, which is required to be considered by CSA A864-00. To the best knowledge of the author, no FE program has this capability, including VecTor2 and VecTor3. As such, special attention is currently needed for the selection of the material properties. Future research should pursue the development of anisotropic changes in material properties based on the expansion level.

The ASR-induced strains are evaluated in the first load stage of the analysis in an incremental fashion. As they are dependent on long-term stress condition, rather than instantaneous loading, the loads active in the first load stage need to be carefully estimated. After the completion of the first load stage, the strain and stress level induced in the structure, as well as the calculated displacements need to be analysed and compared against the observed behaviour. The estimation of the structures' capacity could then be performed through a monotonic pushover analysis.

The selection of the boundary conditions may have critical influence on the calculated response. The laboratory tests, with support conditions well defined for both the duration of ASR development and for the testing phase, pose no difficulty in reproducing the bearing configuration in a numerical model. However, when concrete members which are part of an actual structure are being modelled, special attention should be placed on the boundary conditions.

Chapter 7 Conclusions

7 Conclusions

7.1 Summary

The goal of this thesis was to develop an analytical tool, based on nonlinear finite element analysis (NLFEA) procedures, to model the response of ASR-affected reinforced concrete structures. In this process the following objectives were addressed:

1. Implementation of numerical models which define the expansion strains and the deterioration in mechanical properties that occur as a result of ASR within the algorithms of the NLFEA VecTor programs.
2. Verification of the models implemented, and of the analytical procedure, by modelling ASR-affected specimens of interest for nuclear structures: reinforced concrete beams, prestressed concrete beams, and shear walls.
3. Examination of assessment recommendations pertaining to the analysis and modelling of ASR-affected structures.

7.2 Conclusions

Based on the results of the analyses performed, a series of conclusions and observations can be made:

1. A total-load, secant-stiffness, macro-modelling approach is a viable NLFEA strategy for modelling ASR effects on reinforced concrete structures.
2. The Disturbed Stress Field Model provides a workable platform on which ASR constitutive models can be implemented.
3. The magnitude and direction of the induced strains depend on internal and external restraints as well as long-term loading conditions which must be appropriately considered for the ASR analysis.

4. Strength and stiffness degradation can be taken into account by either employing reduction factors, as recommended by ISE (1992), or using the measured properties. Neither approach performs consistently better than the other when analyzing ASR-affected specimens.
5. The material-level investigation revealed that the ISE reduction factors tend to underestimate the value of the compressive strength for ASR-affected specimens, while the modulus of elasticity is predicted more accurately.
6. Confinement conditions exert a significant influence on the results. Special care should be taken in modelling confinement related mechanisms, such as Poison's effect and strength and stiffness enhancement, in a realistic fashion.
7. The flexural-critical specimens analyzed did not exhibit a significant reduction of either capacity or ductility due to ASR.
8. Some shear-critical specimens, such as shear walls and reinforced concrete beams provided with transverse reinforcement, showed an increase in strength caused by ASR, while an opposite effect was observed on beams with no stirrups.
9. The VecTor programs currently show reasonably good accuracy in the analysis of ASR-affected specimens which are either shear or flexural critical. For the 17 specimens modelled affected by ASR, the ratio of calculated to measured strength had a mean of 1.10 and a coefficient of variation of 8.0%. For the 13 non-ASR specimens modelled the mean was 1.05 with a coefficient of variation of 11.0%.
10. At the material level, with the exception of the model which does not take into account the influence of stresses on expansion, the models yielded similar results. As well, no significant difference in results was observed between the expansion models at the structural level.
11. To achieve improved accuracy and reliability in the analysis capabilities, additional work is required in better describing the constitutive response of ASR-affected concrete.

7.3 Recommendations

Although the outlined objectives were successfully accomplished, a series of limitations and deficiencies were identified during the analytical assessment. The following recommendations are made for future work, which are thought to represent further analytical improvement on modelling the ASR effects in reinforced concrete structures:

1. Reductions in strength and stiffness may be non-uniform in the principal directions due to the anisotropic expansion. Currently, this aspect is not taken into account in VecTor2/VecTor3, nor in other program currently being used. Future research should be directed towards the development of relationships which capture the anisotropy of the mechanical properties.
2. It is known that the aggregate type has a certain influence on the mechanical properties. This influence has not been properly captured by experimental studies, and it is not incorporated in the VecTor programs.
3. Bond degradation is expected to occur as a result of ASR. This issue is not currently addressed. The development of bond degradation models would be of interest especially for specimens which are susceptible to bond slip.
4. The influence of tensile stresses on the induced expansion is captured only by one of the models implemented, the Curtis model; it was formulated based on field observations and is only suitable for linear elastic analysis programs. Further investigations on this matter are required.
5. The influence of ASR on Poisson's effect is not currently quantified. An appropriate model which captures this influence should be developed and implemented.
6. The increase in strength of some shear-critical specimens may be attributed to the confinement effect caused by either the transverse reinforcement in the case of the beams or the boundary elements in the case of shear walls. However, ductility in shear-critical concrete structures affected by ASR is a potential concern. Thus, it is of interest to study the behavioural response of ASR-affected concrete subjected to shear stresses which were allowed free expansion during the ASR development phase.

References

- ACI Committee 201. (1992). Guide to durable concrete, American Concrete Institute, Report of ACI Committee 201.
- Bakker, J.D. (2008) Control of ASR related risks in the Netherlands, *Proceedings of 13th ICAAR*, M. Broekmans, B Wigum ed., NTNU Trondheim.
- Bazant, Z. P., and Steffens, A. (2000). Mathematical model for kinetics of alkali-silica reaction in concrete. *Cement and Concrete Research*, 30(3), 419-428.
- Bazant, Z. P., Zi, G., and Meyer, C. (2000). Fracture mechanics of ASR in concretes with waste glass particles of different sizes. *Journal of engineering mechanics*, 126(3), 226-232.
- Bentz, E. (2010). *Augustus: Post Processor for VecTor2 (Version 5.6.5)*. Copyright 1996-2010 E. Bentz.
- Bouzabata, H., Multon, S., Sellier, A., & Houari, H. (2012). Swellings due to alkali-silica reaction and delayed ettringite formation: Characterisation of expansion isotropy and effect of moisture conditions. *Cement and Concrete Composites*, 34(3), 349-356.
- Bulteel, D., Garcia-Diaz, E., Vernet, C., and Zanni, H. (2002). Alkali-silica reaction: a method to quantify the reaction degree. *Cement and Concrete Research*, 32(8), 1199-1206.
- Charlwood R. G., Solymar S. V., and Curtis D. D. (1992). A review of alkali aggregate reactions in hydroelectric plants and dams. *Proceedings of the International Conference of Alkali-Aggregate Reactions in Hydroelectric Plants and Dams*, Fredericton, Canada. 1992, 129.
- Chatterji, S., and Christensen, P. (1990). Studies of alkali-silica reaction. Part 7. Modeling of expansion. *Cement and Concrete Research*, 20(2), 285-290.
- Chatterji, S., and Thaulow, N. (2000). Some fundamental aspects of alkali-silica reaction. *Proceedings of the 11th International Conference on Alkali-Aggregate Reaction, Quebec City, Canada, June 21-29*.
- Collins, R. J., & Bareham, P. D. (1987). Alkali-silica reaction: Suppression of expansion using porous aggregate. *Cement and Concrete Research*, 17(1), pp 89-96.
- Comby-Peyrot, I., Bernard, F., Bouchard, P. O., Bay, F., and Garcia-Diaz, E. (2009). Development and validation of a 3D computational tool to describe concrete behaviour at mesoscale. Application to the alkali-silica reaction. *Computational Materials Science*, 46(4), 1163-1177.
- Çopuroğlu, O., and Schlangen, E. (2007). Modelling of effect of ASR on concrete microstructure. *Key Engineering Materials*, 348, 809-812.
- CSA Special Publication A844-00, (2000) "Guide to the evaluation and management of concrete structures affected by alkali-aggregate reaction", *CSA International*.
- CUR-recommendation 102, (2008). Inspection and assessment of concrete structures in which the presence of ASR is suspected or has been established. Gouda.
- CUR-recommendation 89, (2008). Measures to prevent damage to concrete by alkali-silica reaction (ASR), Gouda.

- Dent Glasser, L. S., and Kataoka, N. (1981). The chemistry of alkali-aggregate reaction. *Cement and Concrete Research*, 11(1), 1-9.
- Deschenes, D. J., Bayrak O., and Folliard, K.J. (2009). ASR/DEF – Damaged bent caps: shear tests and field implications, *Technical Report No. 12-8XXIA006*.
- Diamond, S. (1989). ASR – Another look at mechanisms. *Proceedings of the 8th International Conference on Alkali-Aggregate Reaction in Concrete*, 83-94.
- Diamond, S., and Thaulow, N. (1974). A study of expansion due to alkali—silica reaction as conditioned by the grain size of the reactive aggregate. *Cement and Concrete Research*, 4(4), 591-607.
- Doran, D., Douglas, J., and Pratley, R., (2009) Refurbishment and repair in construction, Whittles, Scotland.
- Dunant, C. F., and Scrivener, K. L. (2010). Micro-mechanical modelling of alkali–silica-reaction-induced degradation using the AMIE framework. *Cement and Concrete research*, 40(4), 517-525.
- ElMohandes, F. (2013). *Advanced Three-Dimensional Nonlinear Analysis of Reinforced Concrete Structures Subjected to Fire and Extreme Loads*. PhD Thesis, University of Toronto, Toronto, ON, 407 p.
- Fan, S., and Hanson, J. M. (1998). Effect of alkali silica reaction expansion and cracking on structural behavior of reinforced concrete beams. *ACI Structural Journal*, 95(5).
- Farage, M. C. R., Alves, J. L. D., and Fairbairn, E. M. R. (2004). Macroscopic model of concrete subjected to alkali–aggregate reaction. *Cement and Concrete Research*, 34(3), 495-505.
- Gautam, B., et al. (2015). “Alkali Aggregate Reaction in Nuclear Concrete Structures: Part 2: Concrete Materials Aspects”, *submitted to SMiRT23*, Manchester, U.K.
- Giaccio, G., Zerbino, R., Ponce, J. M., & Batic, O. R. (2008). Mechanical behavior of concretes damaged by alkali-silica reaction. *Cement and Concrete Research*, 38(7), 993-1004.
- Gillott, J. E. (1964). Mechanism and kinetics of expansion in the alkali-carbonate rock reaction. *Canadian Journal of Earth Sciences*, 1(2), 121-145.
- Gillott, J. E., & Swenson, E. G. (1969). Mechanism of the alkali-carbonate rock reaction. *Quarterly Journal of Engineering Geology*, 2(1), 7-23.
- Grattan-Bellew, P. E., Mitchell, L. D., Margeson, J., and Min, D. (2010). Is alkali–carbonate reaction just a variant of alkali–silica reaction ACR= ASR?. *Cement and Concrete Research*, 40(4), 556-562.
- Groves, G. W., and Zhang, X. (1990). A dilatation model for the expansion of silica glass/OPC mortars. *Cement and Concrete Research*, 20(3), 453-460.
- Habibi, F., et al. (2015). “Alkali Aggregate Reaction in Nuclear Concrete Structures: Part 1: Structural Wall Element Aspects”, *SMiRT23*, Manchester, U.K.
- Haha, M. B., Gallucci, E., Guidoum, A., and Scrivener, K. L. (2007). Relation of expansion due to alkali silica reaction to the degree of reaction measured by SEM image analysis. *Cement and Concrete Research*, 37(8), 1206-1214.

- Herrador, M. F., Martínez-Abella, F., and del Hoyo Fernández-Gago, R. (2009). Mechanical behavior model for ASR-affected dam concrete under service load: formulation and verification. *Materials and Structures*, 42(2), 201-212.
- Hobbs, D. W. (1981). Discussion: The alkali-silica reaction - a model for predicting expansion in mortar. *Magazine of Concrete Research*, 33(117), 208-220.
- Hobbs, D. W. (1988). "Alkali-silica reaction in concrete", *Thomas Telford Ltd*, London.
- Hobbs, D. W., and Gutteridge, W. A. (1979). Particle size of aggregate and its influence upon the expansion caused by the alkali-silica reaction. *Magazine of Concrete research*, 31(109), 235-242.
- Huang, M., and Pietruszczak, S. (1996). Numerical analysis of concrete structures subjected to alkali-aggregate reaction. *Mechanics of Cohesive-frictional Materials*, 1(4), 305-319.
- Huang, M., and Pietruszczak, S. (1999). Modeling of thermomechanical effects of alkali-silica reaction. *Journal of engineering mechanics*, 125(4), 476-485.
- Iler, R.K. (1979). *The Chemistry of Silica*. Wiley-Interscience, New York, 886.
- Institution of Structural Engineers (ISE). (1992). *Structural Effects of Alkali-Silica Reaction*. SETO, London.
- Jensen, A. D., Chatterji, S., Christensen, P., and Thaulow, N. (1984). Studies of alkali-silica reaction—part II effect of air-entrainment on expansion. *Cement and Concrete Research*, 14(3), pp 311-314.
- Jin, W. (1998). Alkali-silica reaction in concrete with glass aggregate: a chemo-physico-mechanical approach. (PhD Thesis, Columbia University).
- Jin, W., Meyer, C., and Baxter, S. (2000). Glascrete – concrete with glass aggregate. *ACI Materials Journal*, Mar-Apr 2000, pp 208-213.
- Katayama, T. (2010). The so-called alkali-carbonate reaction (ACR) - Its mineralogical and geochemical details, with special reference to ASR. *Cement and Concrete Research*, 40(4), 643-675.
- Kobayashi, K., Inoue, S., Yamasaki, T., & Nakano, K. I. (1988). Alkali aggregate reaction in prestressed concrete beams. *International Journal of Cement Composites and Lightweight Concrete*, 10(4), 233-240.
- Kuroda, T., Inoue, S., Yoshino, A., and Nishibayashi, S. (2004). Effects of particle size, grading and content of reactive aggregate on ASR expansion of mortars subjected to autoclave method. *Proceedings 12th International Conference on Alkali-Aggregate Reaction in Concrete*. Beijing, China, pp 736-743.
- Larive, C. (1997). Apports combinés de l'expérimentation et de la modélisation à la compréhension de l'alkali-réaction et de ses effets mécaniques (PhD Thesis, Ecole nationale des ponts et chaussées).
- Larive, C. (1997). Apports combinés de l'expérimentation et de la modélisation à la compréhension de l'alkali-réaction et de ses effets mécaniques, PhD Thesis, Ecole nationale des ponts et chaussées.

- Larive, C., Laplaud, A., and Coussy, O. (2000). The role of water in alkali-silica reaction. *11th International Conference on Alkali-Aggregate Reaction*, 61-69.
- Léger, P., Côté, P., and Tinawi, R. (1996). Finite element analysis of concrete swelling due to alkali-aggregate reactions in dams. *Computers & structures*, 60(4), 601-611.
- Locher, F.W., Sprung, F. (1973). Ursache und Wirkungsweise der Alkalireaktion. *Beton*, 23(7&8).
- Moës, N., Cloirec, M., Cartraud, P., and Remacle, J. F. (2003). A computational approach to handle complex microstructure geometries. *Computer methods in applied mechanics and engineering*, 192(28), 3163-3177.
- Monette, L.J.-G. (1997). Effects of the alkali-silica reaction on unloaded, statically loaded and dynamically loaded reinforced concrete beams, PhD Dissertation, University of Ottawa, p. 208.
- Multon, S., (2003). *Evaluation Expérimentale et Théorique des Effets Mécaniques de l'Alcali Réaction sur des Structures Modèles*. PhD thesis, Université de Marne la Vallée, France.
- Multon, S., and Toutlemonde, F. (2006). Effect of applied stresses on alkali-silica reaction-induced expansions. *Cement and Concrete Research*, 36(5), 912-920.
- Multon, S., and Toutlemonde, F. (2010). Effect of moisture conditions and transfers on alkali silica reaction damaged structures. *Cement and Concrete Research*, 40(6), 924-934.
- Multon, S., Seignol, J. F., and Toutlemonde, F. (2005). Structural behavior of concrete beams affected by alkali-silica reaction. *ACI Materials Journal*, 102(2), 67-76.
- Multon, S.; Leclainche, G.; Bourdarot, E.; and Toutlemonde, F., (2004). Alkali-Silica Reaction in Specimens under Multi-Axial Mechanical Stresses. *Proceedings of CONSEC 4 (Concrete Under Severe Conditions)*, Seoul, pp. 2004-2011.
- Orbovic, N. et al. (2015). "Alkali Aggregate Reaction in Nuclear Concrete Structures: Part 1: A Holistic Approach", *SMiRT23*, Manchester, U.K.
- Pan, J. W., Xu, Y. J., and Jin, F. (2012). Chemo-Damage Model for Concrete Anisotropic Expansion Caused by Alkali-Aggregate Reaction. *Applied Mechanics and Materials*, 204, 3230-3235.
- Pietruszczak, S. (1996). On the mechanical behaviour of concrete subjected to alkali-aggregate reaction. *Computers & structures*, 58(6), 1093-1097.
- Pietruszczak, S., Jiang, J., & Mirza, F. A. (1988). An elastoplastic constitutive model for concrete. *International Journal of Solids and Structures*, 24(7), 705-722.
- Popovic A., Panesar D.K., and Elgohary M. (2002). "Repair of the Gentility-1 concrete containment ringbeam structure", *Organization for Economic Co-operative Development-Nuclear Energy Agency (OECD-NEA)*, Workshop on the evaluation of defects, repair criteria and methods of repair for concrete structures on nuclear power plants, Berlin Germany, p.11.
- Puatatsananon, W., and Saouma, V. (2013). Chemo-Mechanical Micromodel for Alkali-Silica Reaction. *ACI Materials Journal*, 110(1), 67.

- RILEM AAR-6.1. (2013) Guide to diagnosis and appraisal of AAR damage to concrete in structures. Part I: Diagnosis, RILEM TC 191-ARP.
- Saouma, V., and Perotti, L. (2006). Constitutive model for alkali-aggregate reactions. *ACI materials journal*, 103(3).
- Schlangen, E., and Garboczi, E. J. (1997). Fracture simulations of concrete using lattice models: computational aspects. *Engineering fracture mechanics*, 57(2), 319-332. 36
- Schlangen, E., and Van Mier, J. G. M. (1992). Experimental and numerical analysis of micromechanisms of fracture of cement-based composites. *Cement and Concrete Composites*, 14(2), 105-118. 37
- Selby, R. G. (1990). Nonlinear Finite Element Analysis of Reinforced Concrete Solids. Master of Applied Science Thesis, University of Toronto, 144 p.
- Sellier, A., Bourdarot, E., Multon, S., Cyr, M., and Grimal, E. (2009). Combination of structural monitoring and laboratory tests for assessment of alkali-aggregate reaction swelling: application to gate structure dam. *ACI materials journal*, 106(3).
- Shayan, A., & Ivanusec, I. (1996). An experimental clarification of the association of delayed ettringite formation with alkali-aggregate reaction. *Cement and Concrete Composites*, 18(3), 161-170.
- Shayan, A., and Xu, A. (2004). Value-added utilisation of waste glass in concrete. *Cement and Concrete Research*, 34(1), 81-89.
- Stanton, T. E. (1942). "California Experience with the Expansion of Concrete through Reaction between Cement and Aggregate," *ACI Journal*, 38, 209-215.
- Stanton, T. E., (1940). "Expansion of Concrete through Reaction between Cement and Aggregate," *Proceedings, American Society of Civil Engineers*, pp. 1781-1811. (Reprinted with discussion and closure in *Transaction, ASCE*, V. 107, pp. 54-126)
- Suwito, A., Jin, W., Xi, Y., and Meyer, C. (2002). A mathematical model for the pessimum size effect of ASR in concrete. *Concrete Science and Engineering*, 4(13), 23-34.
- Svensson, S. E. (1991). Eigenstresses generated by diffusion in a spherical particle embedded in an elastic medium. *International Journal of mechanical sciences*, 33(3), 211-223.
- Swamy, R. N., and Al-Asali, M. M. (1988). Engineering properties of concrete affected by alkali-silica reaction. *ACI Materials Journal*, 85(5), 367-374.
- Swenson, E.G. (1957). A reactive aggregate undetected by ASTM tests. *ASTM Bulletin* No. 226, 48-57.
- Taylor, H. F. W., Famy, C., & Scrivener, K. L. (2001). Delayed ettringite formation. *Cement and Concrete Research*, 31(5), 683-693.
- Tcherner, J., and Aziz, T. S. (2009). "Effects of AAR on Seismic Assessment of Nuclear Power Plants for Life Extensions", *Proceedings SMiRT 20*, Espoo, Finland, p. 1-8.
- Tcherner, J., Aziz, T., Panesar, D. K., Demers, M., and Neale, K. W. (2009). "Performance Surveillance of Gentilly-1 Reactor Building GFRP Repair Using Fiber Optic Sensors and Strain Gauges", *Proceedings SMiRT 20*, Espoo, Finland, p. 9-18.

- Ulm, F. J., Coussy, O., Kefei, L., and Larive, C. (2000). Thermo-chemo-mechanics of ASR expansion in concrete structures. *Journal of Engineering Mechanics*, 126(3), 233-242.
- Urhan, S. (1987 a). Alkali silica and pozzolanic reactions in concrete. Part 1: Interpretation of published results and and hypothesis concerning the mechanism. *Cement and Concrete Research*, 17(1), 141-152.
- Urhan, S. (1987 b). Alkali silica and pozzolanic reactions in concrete. Part 2: Observations on expanded perlite aggregate concretes. *Cement and Concrete Research*, 17(3), 465-477.
- Vecchio, F. (2000). Disturbed Stress Field Model for Reinforced Concrete: Formulation. *ASCE Journal of Structural Engineering*, 126(9), September 2000, pp. 1071-1077.
- Vecchio, F. J. (1992). Finite Element Modelling of Concrete Expansion and Confinement. *ASCE Journal of Structural Engineering*, 118(9), 46-56.
- Vecchio, F., and Collins, M. (1986). The Modified Compression Field Theory for Reinforced Concrete Elements Subjected to Shear. *ACI Journal*, 83(2), March-April 1986, pp. 219-231.